



Universidad Nacional Autónoma de México

Posgrado en Ciencias del Mar y Limnología

**Analysis of ocean bottom pressure and tide gauge data to
reveal a tectonic signal in the Guerrero seismic gap**

T E S I S

que para optar por el grado de

Maestro en Ciencias

(Geología Marina)

Presenta:

Miguel Ángel Torres Sánchez

Tutor principal:

Dr. Vladimir Kostoglodov (UNAM)

Comité tutor :

Dra. Cecilia Elizabeth Enríquez Ortiz (Facultad de Ciencias,
UNAM)

Dr. Enric Pàllas Sanz (CICESE)

Dr. Jorge Alejandro Kurczyn Robledo (Instituto de Ingeniería,
UNAM)

Dr. Luis Zavala Sansón (CICESE)

Asesor externo:

Dr. Ito Yoshihiro (Universidad de Kioto)

Ciudad de México, México, Diciembre 2024



Universidad Nacional
Autónoma de México

Dirección General de Bibliotecas de la UNAM

Biblioteca Central



UNAM – Dirección General de Bibliotecas
Tesis Digitales
Restricciones de uso

DERECHOS RESERVADOS ©
PROHIBIDA SU REPRODUCCIÓN TOTAL O PARCIAL

Todo el material contenido en esta tesis esta protegido por la Ley Federal del Derecho de Autor (LFDA) de los Estados Unidos Mexicanos (México).

El uso de imágenes, fragmentos de videos, y demás material que sea objeto de protección de los derechos de autor, será exclusivamente para fines educativos e informativos y deberá citar la fuente donde la obtuvo mencionando el autor o autores. Cualquier uso distinto como el lucro, reproducción, edición o modificación, será perseguido y sancionado por el respectivo titular de los Derechos de Autor.



Universidad Nacional Autónoma de México
Posgrado en Ciencias del Mar y Limnología

**Analysis of ocean bottom pressure and tide gauge data to
reveal a tectonic signal in the Guerrero seismic gap**

T E S I S

que para optar por el grado de

Maestro en Ciencias
(Geología Marina)

Presenta:
Miguel Ángel Torres Sánchez

Tutor principal:
Dr. Vladimir Kostoglodov (UNAM)

Comité tutor :

Dra. Cecilia Elizabeth Enríquez Ortiz (Facultad de Ciencias,
UNAM)

Dr. Enric Pallas Sanz (CICESE)

Dr. Jorge Alejandro Kurczyn Robledo (Instituto de Ingeniería,
UNAM)

Dr. Luis Zavala Sansón (CICESE)

Asesor externo:
Dr. Ito Yoshihiro (Universidad de Kioto)

Ciudad de México, México, Diciembre 2024

**“It makes no difference to me where I go. I am ready to go
anywhere I am needed.”**

- Margaret Tobin Brown

American human-rights activist, philanthropist and Titanic survivor.

Agradecimientos

Instituciones

Estoy muy agradecido con la Universidad Nacional Autónoma de México (UNAM) y el Posgrado en Ciencias del Mar y Limnología, por la increíble oportunidad de estudiar Geología Marina y los apoyos económicos para el desarrollo de este trabajo de tesis.

Al Consejo Nacional de Humanidades, Ciencias y Tecnologías (CONAHCYT) por la beca otorgada durante la maestría.

Al Instituto de Geofísica, por ofrecerme un lugar durante el desarrollo de este trabajo de investigación. Agradezco al Servicio Mareográfico Nacional (SMN) por proporcionar los datos del nivel del mar.

También extiendo mi agradecimiento a la Secretaría de Marina Armada de México (SEMAR) por permitirme concluir parte de mi investigación y por la oportunidad de aprender más sobre el análisis de tsunamis. Asimismo, agradezco al Centro de Control y Procesamiento de Datos (CECOPROD) por los datos del nivel del mar.

Investigadores y técnicos

Agradezco al Dr. Vladimir Kostoglodov por permitirme integrarme a este proyecto sobre el estudio de sismos lentos, por su valioso asesoramiento, su paciencia al responder mis preguntas, y por sus consejos que han sido clave para alcanzar este objetivo profesional.

A los investigadores de mi comité tutorial: Dra. Cecilia Elizabeth Enríquez Ortiz, Dr. Enric Pàllas Sanz, Dr. Jorge Alejandro Kurczyn Robledo y Dr. Luis Zavala Sansón. Les agradezco mucho su disposición, ayuda y comentarios en cada reunión.

Al Dr. Ito Yoshihiro por aceptar ser mi asesor externo y por su tiempo, sus explicaciones y motivación para que esta investigación fuera posible en México.

Al Dr. Raúl Valenzuela Wong por la corrección y sugerencias del texto de Sismología.

A la Ing. Miriam Arianna Zarza Alvarado por su valioso apoyo en la asistencia técnica para el procesamiento y análisis de datos del nivel del mar y análisis de señales de tsunamis.

Al Fis. Sergio Valente Gutiérrez Quijada por su ayuda en el área instrumental y por la facilitación del material fotográfico de estaciones mareográficas.

Gracias a la Dra. Sara Ivonne Franco Sánchez por proporcionarme los datos de GPS, así como por su gran disposición para resolver mis preguntas sobre Geodesia.

Al Cap. Corb. Iván Vladimir Gutiérrez Palacios por su brindarme el espacio y su tiempo para mi trabajo de tesis.

Al Dr. Alejandro Martín Rodríguez Aguayo por su valiosa disposición en la asistencia técnica en el análisis espectral de datos mareográficos.

Al Ing. Iván Rodríguez Rasilla por brindarme su asesoría técnica en temas relacionados a cómputo, así como su gran ayuda en muchos aspectos durante mi maestría.

A la Dra. Isabel Jalón Rojas por resolver mis dudas sobre el análisis armónico de datos del nivel del mar.

Familiares

A mi mamá, Araceli, por la fortaleza, dedicación y perseverancia que me inculcó. A mi hermana, Elsy Marleth, por brindarme su apoyo incondicional en muchas situaciones desafiantes.

CONTENTS

LIST OF FIGURES	ix
LIST OF TABLES	xi
ABSTRACT	xii
RESUMEN	xiii
1 GENERALITIES	1
1.1 Introduction	1
1.1.1 Organization of the Thesis	2
1.2 Justification	2
1.3 Hypothesis	3
1.4 Objectives	3
1.4.1 Overall objective	3
1.4.2 Specific objectives	3
1.5 Study area and instruments	4
1.5.1 Study area	4
1.5.2 Data and instruments	4
1.6 Tectonic setting of the study region	9
2 BASIC CONCEPTS OF SEISMOLOGY AND SLOW SLIP EVENTS	10
2.1 The theory of plate tectonics: a dynamic Earth	10
2.2 Earthquakes	12
2.2.1 Body waves	13
2.2.2 Surface waves	14
2.2.3 Seismic magnitude	15
2.3 Seismic cycle	18
2.4 Slow slip events	20
2.4.1 Slow slip events in the Guerrero seismic gap	22
3 OCEANOGRAPHIC AND METEOROLOGICAL EFFECTS ON SEA LEVEL	24
3.1 Sea level	24
3.1.1 Tsunamis	24
3.1.2 Atmospheric pressure variations	25
3.1.3 Tides	26
3.1.4 El Niño-Southern Oscillation	29
3.1.5 Storm surges	34
3.2 Sea level measurement	35
3.2.1 Tide gauges	35
3.2.2 Ocean-bottom pressure sensors	36
3.2.3 Satellite altimetry	38
4 DATA ANALYSIS	41
4.1 Signal components	41
4.2 Data reduction	42
4.3 Tidal component correction: harmonic analysis	43
4.4 Nontidal component corrections	44
4.4.1 Data filtering	44
4.4.2 LOWESS smoothing	44
4.4.3 Simple moving average	45
4.5 Ocean-bottom pressure data analysis	46
4.5.1 Correlation analysis with ocean-bottom temperature data	50
4.5.2 Correlation analysis with El Niño 3.4 sea surface temperature data	51

4.5.3	Methods to identify tectonic deformation signals generated by slow slip events	52
4.6	Ocean-bottom tilt data analysis	54
4.7	Sea level data analysis	55
4.7.1	Data reduction	55
4.7.2	Harmonic analysis	56
4.7.3	Low-pass filtering	57
4.7.4	Correlation analysis with atmospheric pressure and temperature data	57
4.7.5	Correlation analysis with El Niño 3.4 sea surface temperature data	58
4.7.6	Reference-site method	59
4.8	Long-term trend in pressure sensor 7	60
4.9	Evaluation of variance reduction and coherence between pairs of nontidal ocean-bottom pressure signals.	62
4.10	Analysis of the coseismic displacement of the 2021 Acapulco earthquake recorded in sea level measurements	63
4.11	Analysis of tsunami signals	65
4.11.1	Main characteristics of tsunami signals	65
4.11.2	Amplitude spectrum: characteristic frequencies	69
4.11.3	Spectral ratios: tsunami source model	69
5	RESULTS AND DISCUSSIONS	71
5.1	Tectonic deformation in seafloor pressure and sea level data	71
5.1.1	Ocean-bottom pressure	71
5.1.2	Coastal sea level	80
5.2	Long-term trend in pressure sensor 7	82
5.3	Coherence between pairs of nontidal ocean-bottom pressure signals	84
5.4	Coseismic signal of the 2021 Acapulco earthquake	86
5.5	Tsunamis	88
5.5.1	Main characteristics of tsunami signals	88
5.5.2	Characteristic frequencies	88
5.5.3	Spectral ratios	91
6	CONCLUSIONS	94
	APPENDIX A SEISMIC SIGNALS	97
	APPENDIX B GPS DISPLACEMENT	98
	APPENDIX C EARTH STRUCTURE	99
	APPENDIX D SEA SURFACE TEMPERATURE ANOMALIES OF 1997 AND 1999	100
	APPENDIX E SAFFIR-SIMPSON SCALE	101
	APPENDIX F PRINCIPAL TIDAL CONSTITUENTS	102
	APPENDIX G TEMPERATURE-CORRECTED BOTTOM PRESSURE RECORDS	104
	APPENDIX H INTENSITY CLASSIFICATION OF EL NIÑO AND LA NIÑA EVENTS	106
	REFERENCES	115
	GLOSSARY	116
	ABBREVIATIONS	119
	NOMENCLATURE	119

LIST OF FIGURES

1.1	Study area	6
1.2	Network of the coastal tide gauge stations and ocean-bottom pressure sensors used in this study	7
1.3	Characteristics of the ocean-bottom pressure observations used in this study	8
2.1	Model of convection cell in the mantle	12
2.2	Distribution of the anelasticity in the Tonga subduction zone	12
2.3	Distribution of the principal tectonic plates around the world	15
2.4	Body and surface seismic waves	16
2.5	Model of a subduction zone	18
2.6	Schematic diagram showing the stages of the seismic cycle	19
2.7	Synthetic horizontal GPS displacement showing three slow slip events with a recurrence interval of 3.5 years and a duration of 6 months	21
2.8	Illustration of a seismogenic zone at a convergent plate boundaries	21
2.9	Geometry of the subduction zone of the Cocos plate beneath the North American plate	22
2.10	Slow slip events recorded in GPS displacement time series	23
3.1	Record of the 1883 tsunami caused by the Krakatoa eruption	25
3.2	Inverted barometer effect on the surface of sea level	26
3.3	Earth-Moon system and tidal forces	27
3.4	Semidiurnal tidal pattern	28
3.5	Tidal patterns	29
3.6	Cycle of spring and neap tides	30
3.7	El Niño-Southern Oscillation cycle	32
3.8	El Niño 1982-1983 effects recorded in sea level time series	33
3.9	Components of a tide gauge station.	37
3.10	Timeline of satellite altimeter missions	39
3.11	Basic principle of altimetric measurements in Oceanography	40
4.1	Most common practices of sea level data reduction	42
4.2	Transfer functions.	44
4.3	Ocean-bottom pressure time series	46
4.4	Ocean-bottom temperature time series	47
4.5	Astronomical tide time series calculated from ocean-bottom pressure data	48
4.6	Detided ocean-bottom pressure data	49
4.7	Low-pass filtered ocean-bottom pressure measurements	49
4.8	Correlation diagrams between 30-day low-pass filtered temperature and pressure signals	50
4.9	Cross-correlation diagrams between sea surface temperature anomalies (El Niño 3.4) and ocean bottom-pressure data	51
4.10	Complex empirical orthogonal functions of the ocean-bottom pressure time series	54
4.11	Sea level observations from the Acapulco and Manzanillo tide gauge stations.	55
4.12	Astronomical tide time series calculated from sea level data collected at the Acapulco and Manzanillo tide gauges.	56
4.13	Detided sea level measurements	56
4.14	30-day low-pass filtered sea level measurements from Acapulco and Manzanillo ports	57
4.15	Sea level time series and atmospheric temperature and pressure observations from Acapulco and Manzanillo	58
4.16	Sea level time series and SST anomaly (El Niño 3.4 region)	59
4.17	Bathymetric profile parallel to the motion vector of the Cocos plate.	60
4.18	Model of the incoming Cocos plate sinking rate at station 7	61

4.19	Coseismic displacement of the 2021 Acapulco earthquake recorded by two tide gauges in Acapulco Bay	64
4.20	Arrival of the 2017 Chiapas tsunami at the Manzanillo tide gauge.	65
4.21	Arrival of the 2018 Oaxaca tsunami at the Acapulco tide gauge	66
4.22	Arrival of the 2021 Acapulco tsunami at the Acapulco tide gauge	66
4.23	Arrival of the 2021 New Zealand tsunami at the Acapulco and Manzanillo tide gauges	67
4.24	Arrival of the 2022 Tonga tsunami at the Acapulco and Manzanillo tide gauges	68
5.1	Residual ocean-bottom pressure time series at site 4 obtained using three methods: reference, CEOF1, and CEOF1+2.	76
5.2	Residual ocean-bottom pressure time series at site 5 obtained using three methods: reference, CEOF1, and CEOF1+2.	77
5.3	Seafloor tilt measurements at site 7	78
5.4	Turbulent mixing in the deep ocean	78
5.5	Normalized power spectra of seafloor pressure data corrected using the reference site, CEOF1, and CEOF1+2.	79
5.6	Residual sea level time series obtained by using the reference-station method.	81
5.7	Seismic profile in the Japan Trench	83
5.8	Pearson correlation coefficient for a sample of 30-day filtered seafloor pressure data	85
5.9	GPS time series of ACYA and ACAP	87
5.10	Amplitude spectra of the tsunamis recorded at the Acapulco tide gauge station	90
5.11	Amplitude spectra of the tsunamis recorded at the Manzanillo tide gauge station	90
5.12	Pre-tsunami and tsunami signal spectra of the Tonga tsunami recorded in the Acapulco and Manzanillo tide gauge stations, as well as their respective spectral ratios.	92
5.13	Mean spectral ratio of the 2022 Tonga tsunami	93
A.1	Seismic signals	97
B.1	GPS displacement of the CAYA station	98
C.1	Internal structure of the Earth	99
D.1	Map of sea surface temperature anomalies related to the El Niño and La Niña phenomena	100
G.2	Temperature-corrected seafloor pressure signals	104
G.3	Temperature-corrected OBP signals after applying the reference-site method	105

LIST OF TABLES

2.1	Largest earthquakes in the Ring of Fire region since 1900	13
2.2	Largest volcanic eruptions in the Ring of Fire region since 1800	14
2.3	Scales of seismic magnitude	17
2.4	Classification of earthquakes	17
4.1	Linear trend and intersection of the ocean-bottom pressure data	47
4.2	Contribution to the linear pressure data trend due to Cocos plate motion.	61
5.1	Tsunami characteristics recorded at the Acapulco and Manzanillo tide gauge stations	89
5.2	Pearson correlation coefficients of tsunami spectral signals.	91
E.1	Saffir-Simpson scale	101
F.1	Principal tidal constituents	102
H.1	Intensity classification of El Niño and La Niña events.	106

ABSTRACT

In the seismic gap of Guerrero, Mexico, an earthquake with a magnitude greater than M_W 8 has not occurred in more than 100 years. The last event of this type occurred in 1911. In addition, since 2003, the occurrence of slow slip events (SSEs) that repeat every four years, with a duration of 6 months, has been documented, increasing the risk of a potential earthquake. It is uncertain whether these phenomena can trigger catastrophic earthquakes in subduction zones. In order to gain insight into the amplitude of SSEs offshore of the seismic gap region, we used ocean-bottom pressure measurements from 2017 to 2022. This research was complemented with sea level measurements from 2018 to 2022, obtained from the ports of Acapulco and Manzanillo to correlate the possible transient deformation signal offshore and on the continental shelf.

The reference site and complex orthogonal empirical function analysis methods were used to remove the oceanographic and meteorological signals to identify tectonic signals associated with slow earthquakes. A possible signal of slow earthquakes was found at an ocean-bottom pressure station. As for the sea level data, no signal of slow events was observed; however, the coseismic and postseismic signals of the 2021 Acapulco earthquake were recorded.

In addition, five tsunamigenic events, including the 2022 Tonga tsunami, were analyzed using coastal sea level observations. Fourier spectrum analysis was performed using tsunamigenic signals to estimate frequencies characteristic of the basin topography. The spectral ratio method was also used to estimate the source of the 2022 Tonga tsunami.

RESUMEN

En la brecha sísmica de Guerrero, México, no ha ocurrido un sismo de magnitud mayor a M_W 8 en más de 100 años. El último evento de este tipo sucedió en 1911. Además, desde 2003 se ha documentado la ocurrencia de eventos de deslizamiento lentos (SSEs) que se repiten cada cuatro años, con una duración de 6 meses, lo que ha incrementado el riesgo de un potencial sismo. No se sabe con certeza si estos fenómenos pueden desencadenar terremotos catastróficos en las zonas de subducción. Con el fin de conocer la amplitud de los SSEs frente a la costa de la región de la brecha sísmica, utilizamos mediciones de presión del fondo oceánico desde 2017 hasta 2022. Esta investigación se complementó con mediciones del nivel del mar desde 2018 hasta 2022, procedentes de los puertos de Acapulco y Manzanillo, con el objetivo de correlacionar la posible señal de deformación transiente tanto en la costa como en la plataforma continental.

Se utilizaron los métodos del sitio de referencia y el de análisis de funciones empíricas ortogonales complejas con el objetivo de remover señales oceanográficas y meteorológicas, para identificar señales tectónicas asociadas con sismos lentos. Se encontró una posible señal de sismo lento en una estación de presión del fondo del océano. En cuanto a los datos del nivel del mar, no se observó ninguna señal de eventos lentos; sin embargo, se registraron las señales cosísmica y postsísmica del sismo de Acapulco de 2021.

Además, se analizaron cinco eventos tsunamigénicos, entre ellos el tsunami de Tonga de 2022, que se registraron en datos del nivel del mar costeros. Se realizó un análisis de espectro de Fourier utilizando señales tsunamigénicas, con el objetivo de estimar las frecuencias características de la topografía de la cuenca. También se utilizó el método de cocientes espectrales para estimar la fuente del tsunami de Tonga de 2022.

GENERALITIES

CHAPTER 1

1.1 Introduction

Since 2000 it has been known that in some subduction, zones where large earthquakes (EQs) nucleate, also occur aseismic events, which are called slow slip events (SSEs). The main differences between SSEs and regular earthquakes are their low frequency, longer duration, and nonradiation of seismic waves. Also, their occurrence may coincide, in space and time, with others types of earthquakes: nonvolcanic tremors (NVTs), low-frequency earthquakes (LFES), very low-frequency earthquakes (VLFES) (Rogers and Dragert, 2003; Hirose and Obara, 2005, see Appendix A). However, it is not yet fully understood, the relationship of the latter three to SSEs.

It is important to mention that some slow slips have occurred previous to great earthquakes. An example of this relation is the 2011 Tohoku earthquake (M_W 9.0), Japan, where it was possible to identify two slow earthquakes by analyzing seafloor pressure measurements (Ito et al., 2013); in northern Chile, prior the 2014 Iquique earthquake (M_W 8.1), a sequence of foreshocks could have been detonated due to an SSE (Kato et al., 2012); in Costa Rica, slow slip events develop in the interseismic stage, although they do not exhibit the typical pattern of occurrences (Kato et al., 2012).

In regards to the duration and ciclicity of SSEs, it is different for every particular area. For instance, in the subduction zone under Vancouver Island, there are aseismic events approximately every 14 months (Bletery and Nocquet, 2020). In contrast, in the Hikurangi subduction Margin, New Zealand, slow earthquakes last from 2 to 4 weeks, with a repetition interval of 18 to 24 months (Wallace et al., 2016). In the Guerrero Pacific coast, Mexico, they occur approximately every four years with a duration of 6 months (Radiguet et al., 2012).

The discovery of slow earthquakes was possible due to the employment of GPS networks for the study of ground deformations. Therefore, it is relevant to extrapolate the knowledge since the pre-GPS era to obtain more information about aseismic events. For instance, by using sea level data from tide gauges, we can also identify vertical deformation signals (e.g., Yamaguti, 1965). In Mexico, sea level has been measured since 1950 (SMN, 2024).

In this investigation, we studied slow slip events occurring in the Guerrero seismic gap (GSG), Mexico, during the period 2018–2022, using ocean-bottom pressure (OBP) sensors. For the first time in Mexican seismology, we can analyze the possible SSE displacements off the Guerrero Pacific coast, since the previous studies were conducted using GPS data in the continental region.

A large earthquake in the Guerrero seismic gap could trigger a tsunami with devastating effects due to the low-lying urban settlements in that region. Historical records indicate that the coasts of Mexico have experienced tsunamis, with waves reaching up to 9-10 meters (Farsangi, 2021). Consequently, we analyzed the tsunami records that affected the ports of Acapulco and Manzanillo from 2017 to 2022.

1.1.1 Organization of the Thesis

The structure of this thesis is as follows:

Chapter 2 provides an overview of basic seismology as well as the origin, mechanisms, and characteristics of slow slip events in the Guerrero seismic gap.

Chapter 4 reviews some oceanographic and meteorological phenomena affecting the sea surface, which contribute to the noise in ocean-bottom pressure and sea level measurements relevant to this research.

Chapter 5 details the analysis of ocean-bottom pressure and sea level data to detect tectonic deformation. This study also included a spectral analysis of the tsunami signals.

Chapter 6 presents the results and conclusions, along with important considerations for future research into the Guerrero seismic gap.

This thesis also includes appendices that provide supplementary information, such as illustrations, data, and additional procedures. Given the interdisciplinary nature of this research, which spans both seismology and oceanography, a glossary is included to facilitate understanding, as well as a list of abbreviations and nomenclature.

1.2 Justification

Given the convergence of the Cocos Plate under the North American Plate and the existence of a seismic gap in Guerrero, Mexico, the relevance of this research lies in evaluating the amplitude of slow slip events off the Guerrero Pacific coast.

The Guerrero seismic gap is anticipated to experience an earthquake with a magnitude $\geq M_W 8$ (Suárez et al., 1990). A similar earthquake has not occurred since 1911. Therefore, a large-magnitude event could affect densely populated areas such as Acapulco, Zihuatanejo,

and Mexico City. For this last city, the potential risk would increase for three reasons: (1) The distance between Mexico City and Costa Grande is ~ 300 Km, while the distance between Mexico City and the 1985 earthquake epicenter is ~ 400 Km. (2) The soil material of the Mexico City basin is composed mainly of lacustrine clay deposits; therefore, it causes the passage of seismic waves to suffer local amplification. Many buildings (not subject to the building code) would be severely damaged. (3) The population of Mexico City is more than 9 million, and it is the most important political and financial center in Mexico. A seismic event of this magnitude ($\geq M_W 8$) would collapse its economic system.

Estimating the SSE amplitudes and the tsunamigenic risk would allow us to better understand possible large earthquakes triggered by slow slip events. Furthermore, the basis for updating the construction codes of cities located in seismic risk areas would be expanded, and prevention culture would be improved by preparing risk maps.

1.3 Hypothesis

The joint analysis obtained with ocean bottom pressure and sea level measurements is capable of detecting, if the SSEs propagate to the continental margin, aseismic event signals off the Pacific coast of Guerrero, Mexico.

1.4 Objectives

1.4.1 Overall objective

Discern the vertical displacement of the continental margin off the Costa Grande region of Guerrero at a resolution of centimeters.

1.4.2 Specific objectives

- Study ocean-bottom pressure, ocean-bottom tilt, and sea level records to identify the changes of transient crustal deformation and coseismic displacement caused by the September 8, 2021 Acapulco earthquake ($M_W 7.1$).
- Find appropriate filtering techniques to remove oceanographic and meteorological effects from the ocean-bottom pressure and sea level time series.
- Analyze tsunami signals recorded from 2017 to 2022 in the Manzanillo and Acapulco tide gauges to identify maximum tsunami amplitudes and maximum peak-to-trough height.

- Perform Fourier spectral analysis of the tsunami records to identify frequencies associated with basin resonating characteristics.
- Calculate the spectral ratio of the 2022 Tonga tsunami signal to determine its source spectrum and examine its frequencies.
- Explain the sensor drift observed in the measurements from one of the ocean bottom pressure sensors.

1.5 Study area and instruments

1.5.1 Study area

The study area comprises the 120 km long northwest Guerrero seismic gap (Figure 1.1), where the Cocos plate subducts beneath the North American plate. The collision between these two tectonic plates has generated earthquakes of great magnitude, e.g. the 1985 Michoacán earthquake (Figure 1.1). Since 1911, no $M_W \geq 8.0$ subduction thrust earthquakes have been recorded in the seismic gap¹ identified by Singh et al. (1981). According to Nishenko and Singh (1987), large subduction earthquakes occur approximately every 30-50 years along the Pacific coast of Mexico. Therefore, the absence of an earthquake with a magnitude $M_W \geq 8.0$ since 1911 represents almost 113 years so far.

Concerning the dimensions of the extended seismic gap (rupture areas of 1911, 1957, and 1962 earthquakes), and based on the convergence rate (DeMets et al., 2010), plates' coupling coefficients, etc., the seismic gap can be divided into (Figure 1.2):

- Northwest Guerrero seismic gap (120 km long): lower coupling and therefore low elastic strain rate accumulation.
- Southeast Guerrero seismic gap (95 km long): higher coupling and deformation rate.

In this research, the study area is the Northwest Guerrero seismic gap (Figure 1.2), so we will refer to it as the Guerrero seismic gap (GSG).

1.5.2 Data and instruments

To determine the extent of these phenomena beyond the coastline, we used temporary stations installed on the seafloor off the Guerrero seismic gap, which recorded ocean-bottom pressure

¹The seismic gap hypothesis states that after a large earthquake, the seismic risk is low and increases with time.

and tilt from 2017 to 2022 (Figure 1.2). These instruments were installed within the SATREPS (Science and Technology Research Partnership for Sustainable Development) project, a collaboration between Mexico and Japan. Only OBP sensors 4, 5, and 7 were recovered² during the Puma oceanographic campaign in April 2022.

Seafloor pressure observations are the result of the hydrostatic load of the water column, along with other external factors such as tsunamis, temperature variations, and wind effects (Figure 1.3). When searching for the tectonic component in the pressure time series, it is crucial to consider the influence of external factors, which introduce noise into the data. Our goal is to separate tectonic signals from the environmental interference. Such tectonic signals are expected to reflect the uplift or subsidence of the continental margin (Figure 1.3), caused by stress accumulation and gradual release during slow slip events.

We obtained sea level data from tide gauge stations in Acapulco and Manzanillo for the years 2018-2022 (Figure 1.2). The Servicio Mareográfico Nacional³ and the Secretaría de Marina Armada de México⁴ provided the data. Using north-south GPS horizontal⁵ displacement data at the CAYA station (Figure 1.2), we can correlate the slow-earthquake periods.

²We also received 11 months of bottom pressure observations from sensor 6, but the sensor failed because it had a 1-second sampling rate, which significantly reduced its battery life.

³The national agency is in charge of monitoring the sea level in Mexico.

⁴Mexican Navy

⁵Any GPS station records surface displacements in three components: two horizontal (West-East or North-South) and one vertical. However, the horizontal components, are less susceptible to seasonal noise (see Appendix B for more details).

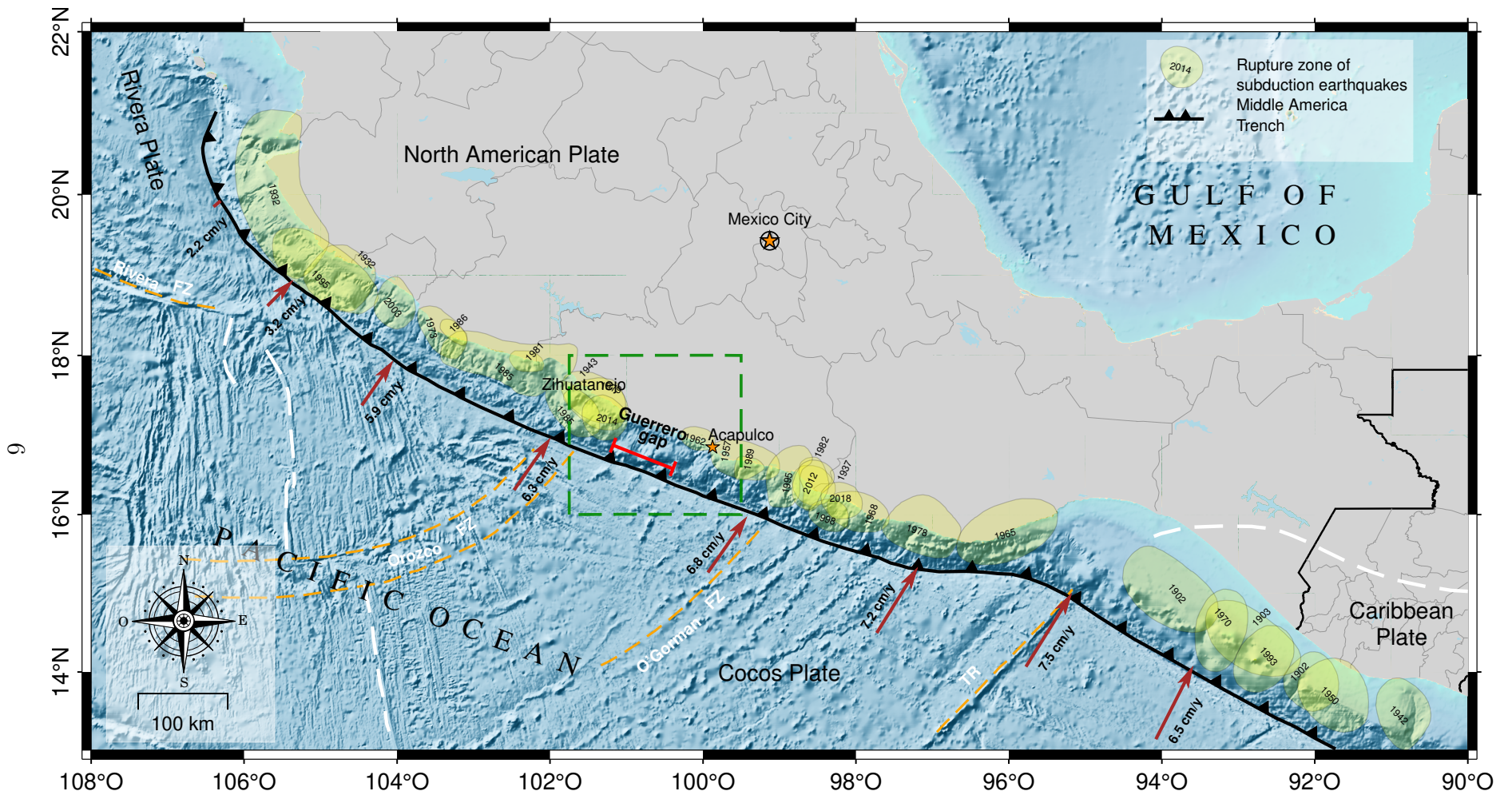


Figure 1.1. Location of the study area is indicated by the dashed green line. FZ: Fracture zone; TR: Tehuantepec ridge. Red rows show the direction and magnitude of the relative motions between the North American, Cocos, and Rivera plates. Dashed white lines indicate fracture zones. Yellow shaded areas outline large earthquakes since 1900. Adapted from Kostoglodov and Pacheco (1999), cited in Cruz-Atienza et al. (2018).

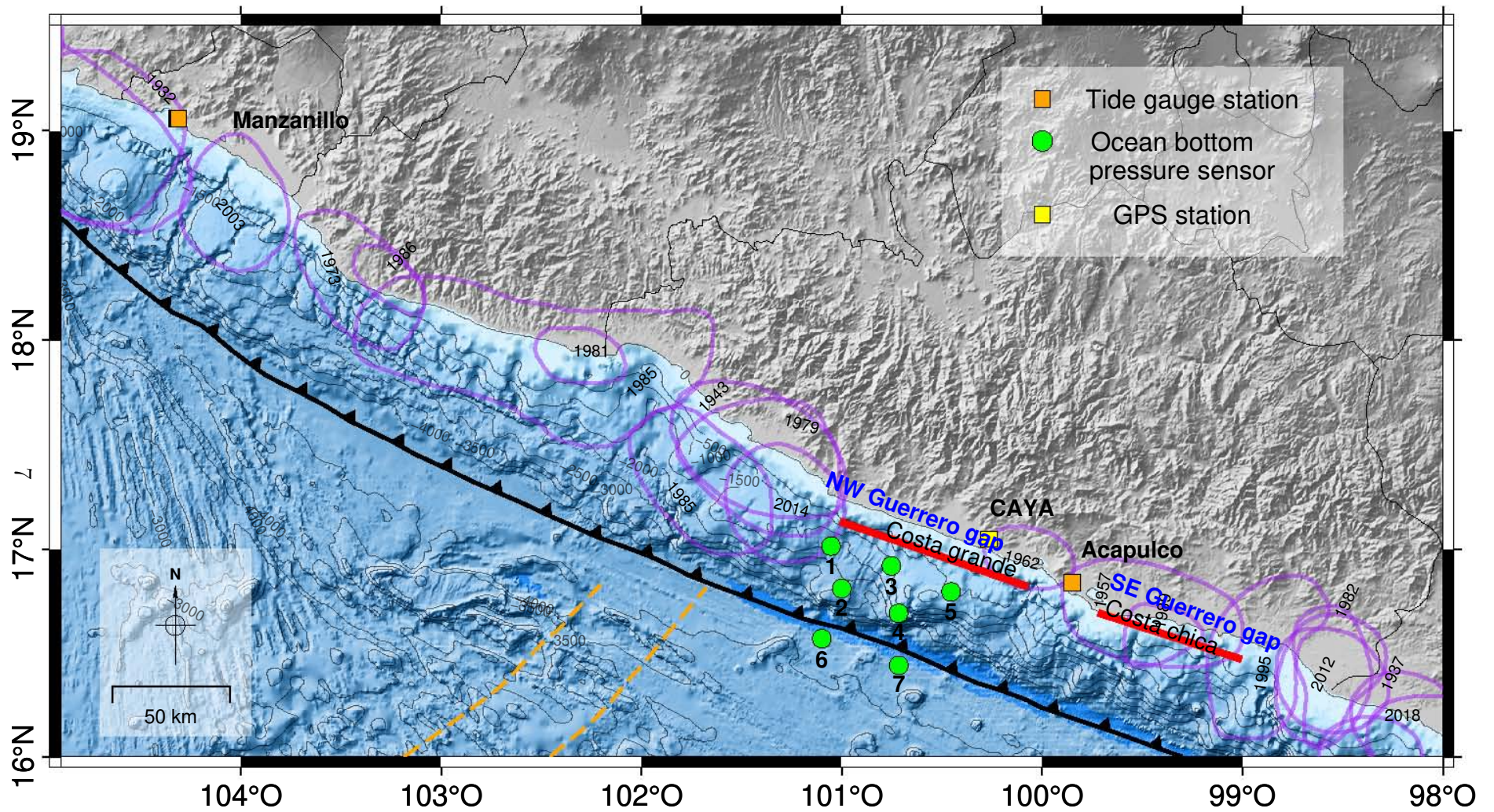
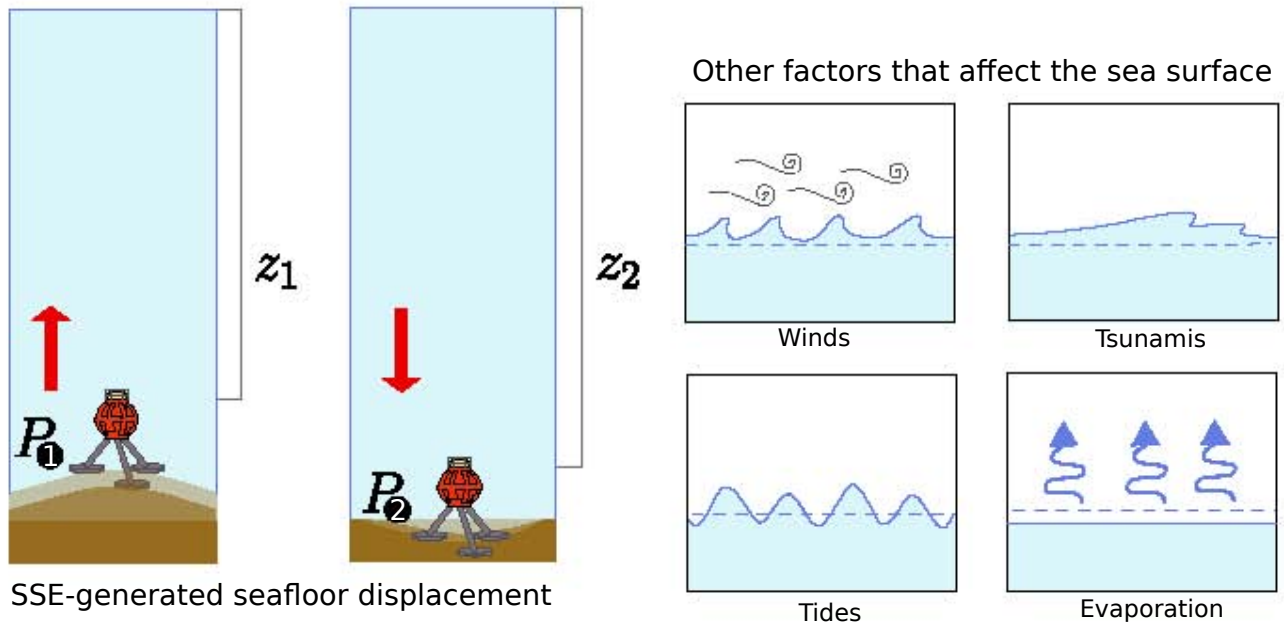
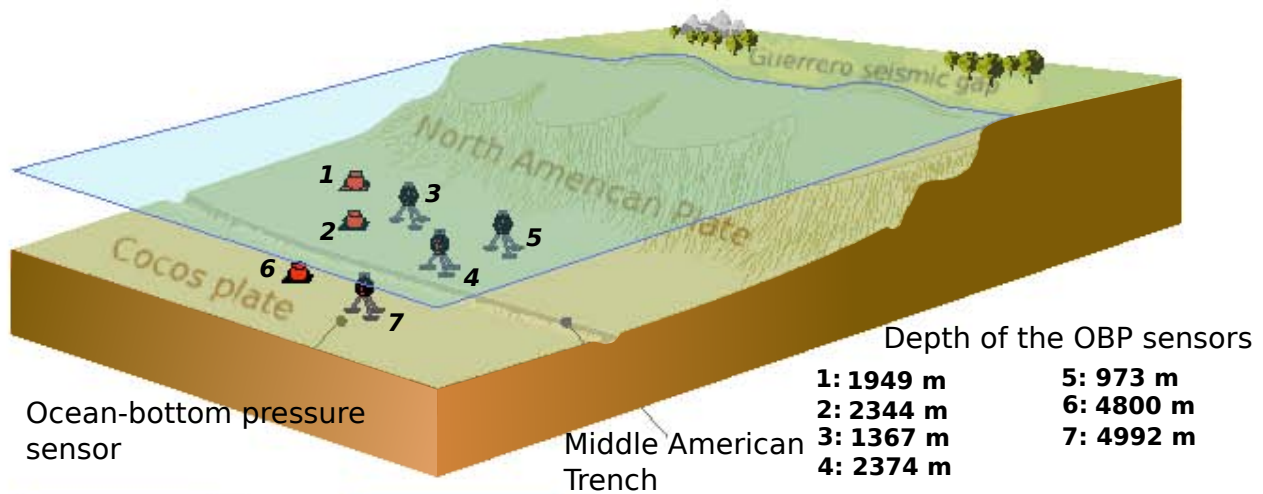


Figure 1.2. Map of the tide gauge stations and ocean-bottom pressure sensors (SATREPS project) used for this study. The OBP measurements are from November 2017 to March 2022, and only sensors 4, 5, and 7 were recovered. The distance between the Acapulco and Manzanillo stations is 530 km. Purple contours outline large earthquakes since 1900. Bathymetric contours are in meters. Source: Cruz-Atienza et al. (2018) and Plata-Martínez et al. (2021).



$$P_1 < P_2$$

P : Pressure at the seafloor
 z : Height of the water column

Figure 1.3. Characteristics of the ocean-bottom pressure observations used in this study, and an illustration of “noise” factors.

1.6 Tectonic setting of the study region

The Cocos plate subducts northeastward beneath the North American plate along the Mesoamerican Trench (Figure 1.1). The subduction angles range from approximately 12° to 15° , with the subduction rate increasing from 4.8 to 7.5 cm/yr in the southeastern direction (Pardo and Suárez, 1995; DeMets et al., 2010). The Cocos and Rivera plates are considered to have formed a single lithospheric unit, the Farallon plate, approximately 11 Ma ago. The splitting of the Farallon plate led to the origin of the Nazca and Cocos plates, which occurred in the early Miocene due to a 3,000 km-long fracture (Lonsdale, 2005). Subsequently, the Cocos plate fragmented 10 Ma ago, resulting in the formation of the Rivera microplate (DeMets and Traylen, 2000).

The lithospheric boundaries of the Cocos plate are as follows: to the north, the North American and Rivera plates; to the northeast, the Caribbean and Panama plates; to the east and south, the Nazca plate; and to the west, the Pacific Plate. The Cocos plate encompasses the Orozco and O’Gorman fracture zones and the Tehuntepec ridge (Figure 1.1). The Guerrero seismic gap, the subject of our research, is situated between the Orozco and O’Gorman fracture zones (Figure 1.1).

BASIC CONCEPTS OF SEISMOLOGY AND SLOW SLIP EVENTS

CHAPTER 2

2.1 The theory of plate tectonics: a dynamic Earth

The observations that preceded the consolidation of the plate tectonics theory came from geologist Eduard Suess's scientific contributions. He proposed that mountains formed due to crust contracting over time. According to his hypothesis, the Alps orogeny was caused by the lateral collision of discrete blocks (Neubauer, 2014). Although Suess stated that the continents remained fixed¹, his book *Faces of the Earth* (1885) explained that the continents first came together to form a continental unit called "Gondwanaland". This was a paleo-continent made up of the southern continental regions: Africa, South America, India, and Madagascar. He supported the idea that the distribution of the plant fossil *Glossopteris* was consistent across the previous regions.

Another hypothesis, which denied the idea of a fixed earth, came from the study of Alfred Wegener in his book *The Origins of Oceans and Continents* (1915). He introduced, for the first time, the term continental drift, supported by evidences such as (Wegener, 1915): (1) geological blocks of the same type were found in both South America and Africa; (2) paleoclimatic: Large glaciers once covered regions in the Southern Hemisphere, merging into a single ice block. Evidence of glacial striations has been found on rocks from continents that now have vastly different climates; (3) fossils: *Mesosaurus* fossils were found in Brazil and South Africa (similar to Suess' evidence). All these points supported the idea that the continents were united in a land mass called "Pangea".

The theory of continental drift has been attributed to Alfred Wegener (Hallam, 1975), although Frank Taylor had already referred to it in 1908 (published in 1910). Taylor explained to the American Geological Society that "sheets of Earth's crust" caused the formation of the Tertiary mountains (Totten, 1981). Furthermore, he concluded that continents came from polar blocks that migrated to the Equator in response to tidal forces.

¹The formation of mountains and oceans, as well as the similarities between continental rims and margins were explained before Suess brought them to light. Some researchers believed that the Earth was stationary, while others believed that it was in motion.

The hypothesis of Alfred Wegener and Frank Taylor could not explain the mechanism of continental drift. Therefore, Holmes (1931) proposed the hypothesis of convection cells in the mantle: analogous to a volume of boiling water, the hottest (less hot) and less dense (denser) part rises (sinks), driving the displacement of the fluid. According to Holmes, the energy that drives the convection process comes from radioactive decay in the Earth's interior² (Jaupart and Mareschal, 2010).

Geologist Alexander L. Du Toit suggested to divide the continent Pangea, proposed by Wegener, into two parts: Laurasia³, in the equatorial region, and Gondwana, to the South. This configuration restored the Gondwana glaciers to coincide in age with the coal-forming plants of the Northern regions. The Equator at that time would have favored swampy environments that were favorable for coal formation.

By 1960, the continental drift theory was becoming more accepted by the geological community. For example, research by Ewing and Ewing (1959) using a marine seismic survey in the Mid-Atlantic Ridge revealed that the speed of the seismic waves increased as they traveled away from the ridge axis. It was found that magnetic reversal patterns were recorded in the lavas of the mid-ocean ridges.

Finally, in 1962, Harry Hess unified the previous ideas and established the seafloor spreading theory: In mid-ocean ridges, magma rises due to convection currents (Hess, 1962). On the other hand, the older and denser seafloor sinks⁴ in subduction zones, thus completing a cycle (see Figure 2.1).

However, there were still divisions regarding whether the Earth was fixed or mobile. In the geological context at that time, Tuzo Wilson established the geological mechanism of the formation of the Hawaiian Islands: hot spots coming from the mantle (see Appendix C). In his work, he mentioned that the age of the islands increases as they move away from the Island of Hawaii and that the islands have a linear pattern and lose support as they become inactive volcanoes exposed to erosion (Wilson, 1963). He deduced that the Pacific plate moves to the northwest, dragging the volcanic islands.

Those observations were related to specific points of discoveries in Seismology. Among them, the results of the quality factor (Q), stand out. These were obtained from the paths of seismic waves in the transition between continental and oceanic crust (e.g., Anderson et al., 1965; Utsu, 1966). So, it was possible to infer that oceanic crust subducted under continental crust (Figure 2.2).

²William Thomson proposed that the Earth's internal energy emanated from its accumulation during formation. Later, the crustal rocks were found to have natural radioactivity.

³It was formed by North America, Europe, and Asia, except the Indian peninsula.

⁴It is a geological process known as subduction.

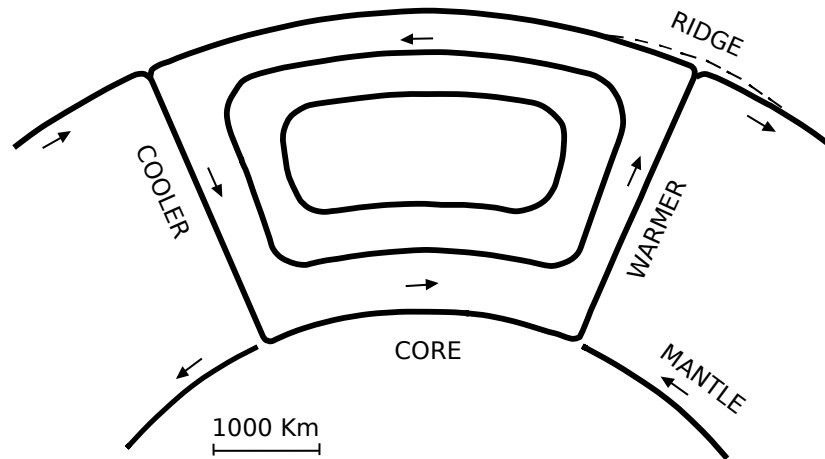


Figure 2.1. Model of convection cell in the mantle. Hess (1962) took up Holmes' idea of convection to support the mechanism of volcanic activity in mid-ocean ridges. Adapted from Hess (1962).

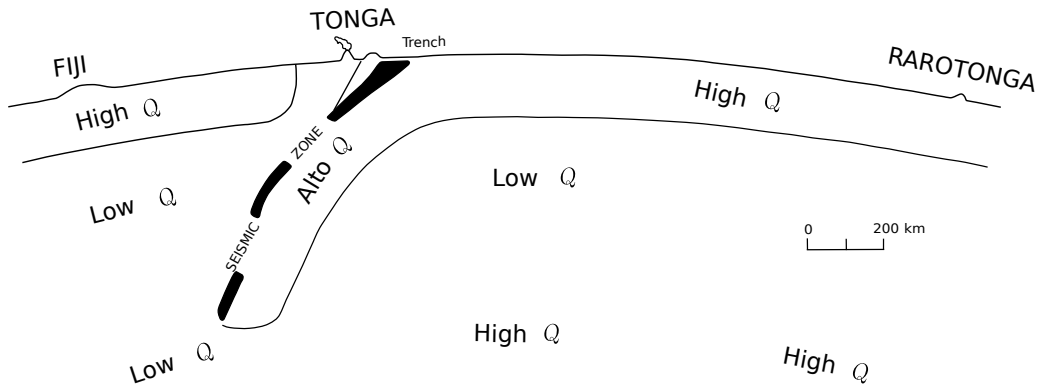


Figure 2.2. Model proposed by Oliver and Isacks (1967) of the Pacific plate subducting beneath the Australian plate along the Tonga trench.

As expected, most large earthquakes (Table 2.1) and violent volcanic eruptions (Table 2.2) occur along convergent plate boundaries. Particularly, there is a region delimited by the edges of the Pacific plate where geological activity is most intense, and is called the Pacific Ring of Fire (Figure 2.3). The most disastrous earthquakes recorded in modern times have occurred in this region (Isacks et al., 1968).

2.2 Earthquakes

Earthquakes are caused by the sudden slip of two blocks of Earth's crust⁵ that come together at a geological fault once the breaking point of the rocks or the static friction of pre-existing faults is exceeded. The slip area caused by a seismic event is called a seismic rupture area. The starting point of the earthquake rupture is called the hypocenter, while its vertical projection

⁵Earthquakes also occur in the subducted slabs sinking into the mantle, although they are rare.

Table 2.1. Largest earthquakes in the Ring of Fire region since 1900.

Location	Date (mm/dd/yr)	Magnitude	Latitude	Longitude
Off the Coast of Ecuador	01/31/1906	8.8	1.00	-81.50
Chile-Argentina Border	11/11/1922	8.5	-28.55	-70.50
Kamchatka	02/03/1923	8.5	54.0	161.00
Banda Sea, Indonesia	01/02/1938	8.5	-5.05	131.62
Kamchatka	04/11/1952	9.0	52.76	160.06
Andreanof Islands, Alaska	03/09/1957	8.6	51.56	-175.39
Chile	05/22/1960	9.5	-38.29	-73.05
Kuril Islands	12/13/1963	8.5	44.90	149.60
Great Alaska Earthquake	03/28/1964	9.2	61.02	-147.65
Rat Islands, Alaska	02/04/1965	8.7	51.21	178.50
Off the West Coast of Northern Sumatra	12/26/2004	9.1	3.30	95.78
Northern Sumatra, Indonesia	03/28/2005	8.6	2.08	97.01
Southern Sumatra, Indonesia	09/12/2007	8.5	-4.43	101.37
Offshore Maule, Chile	02/27/2010	8.8	-35.84	-72.71
Near the East Coast of Honshu, Japan	11/03/2011	9.0	38.32	142.36
Off the west coast of northern Sumatra	04/11/2012	8.6	2.31	93.06

Adapted from Saksono et al. (2018).

on the Earth's surface is the epicenter (Figure 2.5). Some of the elastic energy is released in a dislocation and partially transform into heat as a product of the friction between the rock masses, and the rest of the energy is released as seismic waves. In order to generate a seismic wave, either a natural source (e.g., an earthquake) or an artificial source (e.g., an explosion) is needed. An elastic medium, such as the Earth's interior, is also needed for waves to propagate. Seismic waves are classified as body waves and surface waves (Fowler et al., 1990).

2.2.1 Body waves

They are waves that travel from an Earth's interior point through its layers and contain high frequencies. Simeon-Denis Poisson proposed their existence in 1828 (Ben-Menahem and Singh, 2012). There are two types of body waves:

- **Longitudinal waves:** Also called P waves (primary), they travel the fastest and, in consequence, are the first to be recorded on a seismograph (Kulhánek, 2012). The material which they travel suffers compression (increase in the density of matter in an instant of time) and rarefaction (decrease in the density of matter in an instant of time) (Fowler et al., 1990), that is, the direction of its displacement is parallel to the propagation of seismic energy (Figure 2.4). P waves can travel through liquids and solids.

Table 2.2. Largest volcanic eruptions in the Ring of Fire region since 1800.

Location	Date (yr)	VEI ¹	Latitude	Longitude
Tambora, Indonesia	1815	7	-8.25	111
Krakatau, Indonesia	1883	6	-6.102	105.423
Novarupta, Alaska	1912	6	58.27	-155.15
Mount St. Helens, Washington	1980	5	46.2	-122.18
El Chichón, México	1982	5	17.36	-93.22
Mount Pinatubo, Philippines	1991	6	15.13	120.35
Hunga Tonga-Hunga Ha'apai, Tonga	2022	5	-20.53	-175.390

Source: USGS (2023) and Zobin and Jiménez (2008).

¹ VEI: Volcanic explosivity index.

- **Transverse waves:** These seismic waves are known as S waves (secondary), and their displacement is perpendicular to the direction of wave propagation. They move matter particles up and down, and can be observed on a seismogram after the arrival of the P wave (Figure 2.4). Due to their inability to travel through liquids, it has been inferred that the outer core is liquid (Brush, 1980).

In an elastic, homogeneous, and isotropic medium, the P velocity of the wave is given by the following expression (Fowler et al., 1990):

$$v_p = \sqrt{\frac{\lambda + 2\mu}{\rho}} \quad (2.1)$$

where λ and μ (shear modulus) are the Lamé parameters and ρ is the medium density. Regarding the velocity of the S wave, it is denoted by:

$$v_s = \sqrt{\frac{\mu}{\rho}} \quad (2.2)$$

2.2.2 Surface waves

The constructive interference of the body waves from shallow earthquakes generates the surface waves (Bath, 2013). These types of waves travel parallel to the free surface or along discontinuities of the Earth's interior. Since their amplitudes are more significant⁶ than the body waves, they generate more structural damage. There are two types of surface waves:

- **Rayleigh waves:** In a homogeneous space, the retrograde vertical elliptical motion of the particles (counterclockwise) produces Rayleigh waves (LR). Their origin is due to

⁶As the depth increases, the surface wave amplitudes decrease.

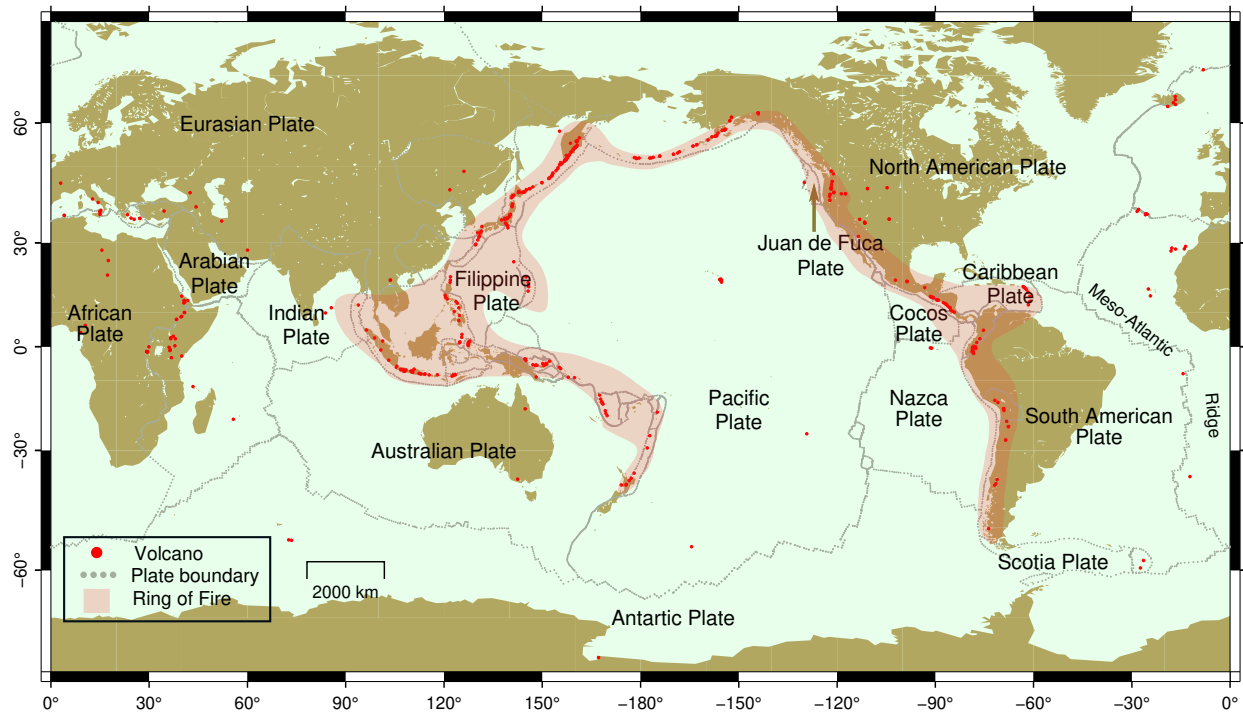


Figure 2.3. Distribution of the principal tectonic plates around the world. Source: Kious and Tilling (1996) and OSU (2021).

the constructive interference between the P and S_v waves (Kulhánek, 2012) (Figure 2.4). Lord Rayleigh demonstrated their existence in 1885.

- **Love waves:** Lord Rayleigh demonstrated their existence in 1885. The reflection of the S_h waves (horizontally polarized S waves) in the low-velocity layer originates the Love waves (LQ). At the same time, the particle movement is perpendicular and parallel to the surface of the direction of propagation (Lay and Wallace, 1995) (Figure 2.4). The LQ wave was discovered in 1911 by mathematician Augustus E. H. Love.

2.2.3 Seismic magnitude

The seismic magnitude is one of the principal parameters that is calculated after an earthquake occurs. This parameter characterizes the energy of seismic waves produced by a particular earthquake. So then, the seismic scale is a measurement relative to the size of an earthquake. It was introduced by Richter (1935) as a local magnitude (M_L) to quantify the magnitude of seismic events in Southern California (Equation 2.3).

$$M_L = \log(A) - \log(A_0(\Delta)) \quad (2.3)$$

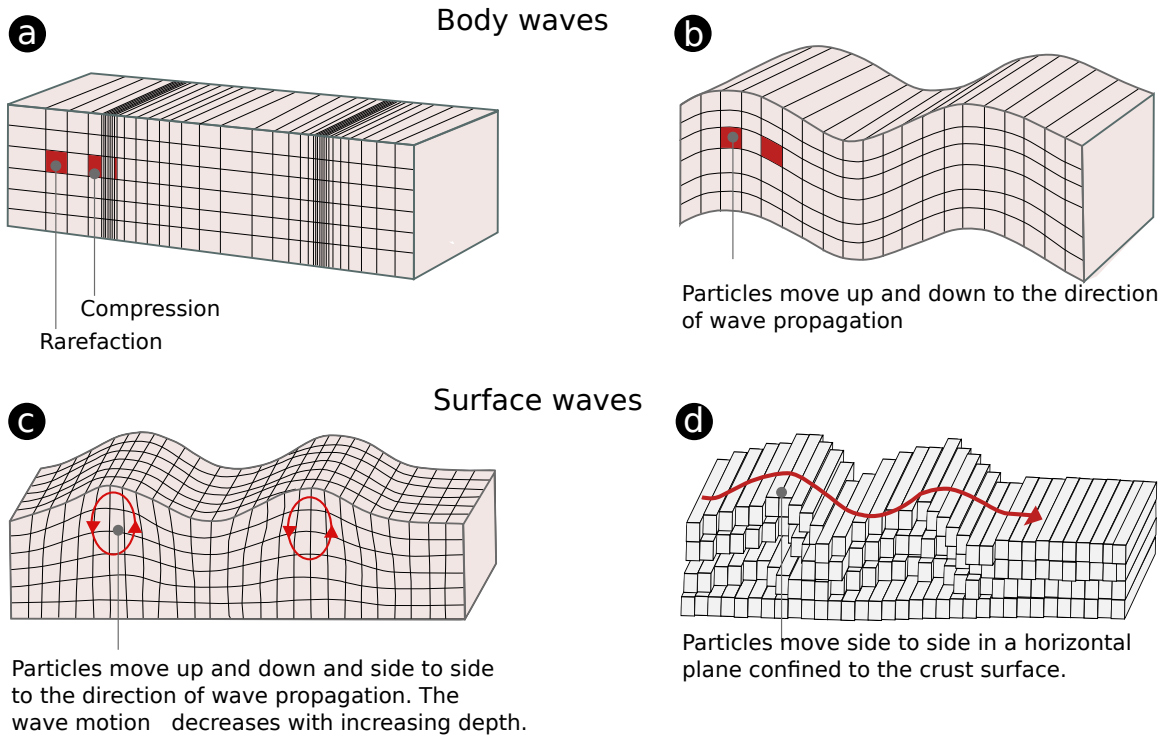


Figure 2.4. Classification of the seismic waves: body waves (a) P and (b) S ; and surface waves (c) Rayleigh and (d) Love. Adapted from Grotzinger et al. (2010).

where A is the maximum amplitude (in millimeters) recorded on a seismogram, while $\log(A_0(\Delta))$ represents the logarithm of the amplitude at the distance Δ^7 at which the earthquake was recorded (Richter, 1935).

The M_L magnitude was defined for shallow earthquakes recorded by the Wood Anderson seismograph and measured exclusively for seismic activity in the California region (Boore, 1989). So, this magnitude scale would not be adequate to report an earthquake that occurred in another part of the world. As a result, different scales have been created considering the seismotectonics of a region, the radiated energy by an earthquake, and the type of seismic phase, among others (Table 2.3).

While a large earthquake occurs, it can saturate the seismogram, i.e., the amplitudes of seismic waves exceed the seismometer's bandwidth, so measuring them is difficult or impossible. For magnitudes $M > 7.0$, the M_s magnitude value is saturated and does not correspond to the real energy of the earthquake. To avoid the above problem, Hanks and Kanamori (1979) proposed the moment magnitude scale M_W , defined as:

⁷Values tabulated by Richter (1935).

Table 2.3. Scales of seismic magnitude.

Magnitude	Expression	Description
Coda magnitude	$M_c = a \log(t_c) + c$	a y c are constants for different areas; t_c is the coda time measured from P wave arrival time to the seismic signal attenuation.
Body wave magnitude	$M_B = \log(A/T) + Q(\Delta, h)$	A/T is the maximum amplitude of the P wave measured on the vertical component and then divided by the period T . $Q(\Delta, h)$ is an attenuation function that depends on the epicentral distance Δ and hypocentral distance h .
Surface wave magnitude	$M_s = \log(A/T) + 1.66 \log(\Delta) + 3.3$	A is the maximum amplitude (μm) of the surface waves, Δ is distance in degrees.
Energy magnitude	$M_e = (2/31) \log(E_s) - 2.9$	E_s is the radiated energy by the earthquake.

Source: Havskov and Ottemoller (2010).

$$M_W = \frac{2}{3} \log_{10}(M_0) - 10.7 \quad (2.4)$$

where M_0 is the seismic moment (Newton-meters) and is a function of

$$M_0 = \mu A_f D \quad (2.5)$$

here A_f is the fault area, and D is the average displacement of the fault. Calculating the magnitude of an earthquake give us an idea about the size of the earthquake, considering different parameters recorded on seismograms. Table 2.4 shows the general classification of earthquakes according to their magnitude, M_W .

Table 2.4. Classification of earthquakes.

Size classification	Magnitude
Great	$M_W > 8$
Large	$M_W = 6-8$
Medium	$M_W = 4-6$
Small	$M_W = 2-4$
Micro	$M_W < 2$

Adapted from Havskov and Ottemoller (2010).

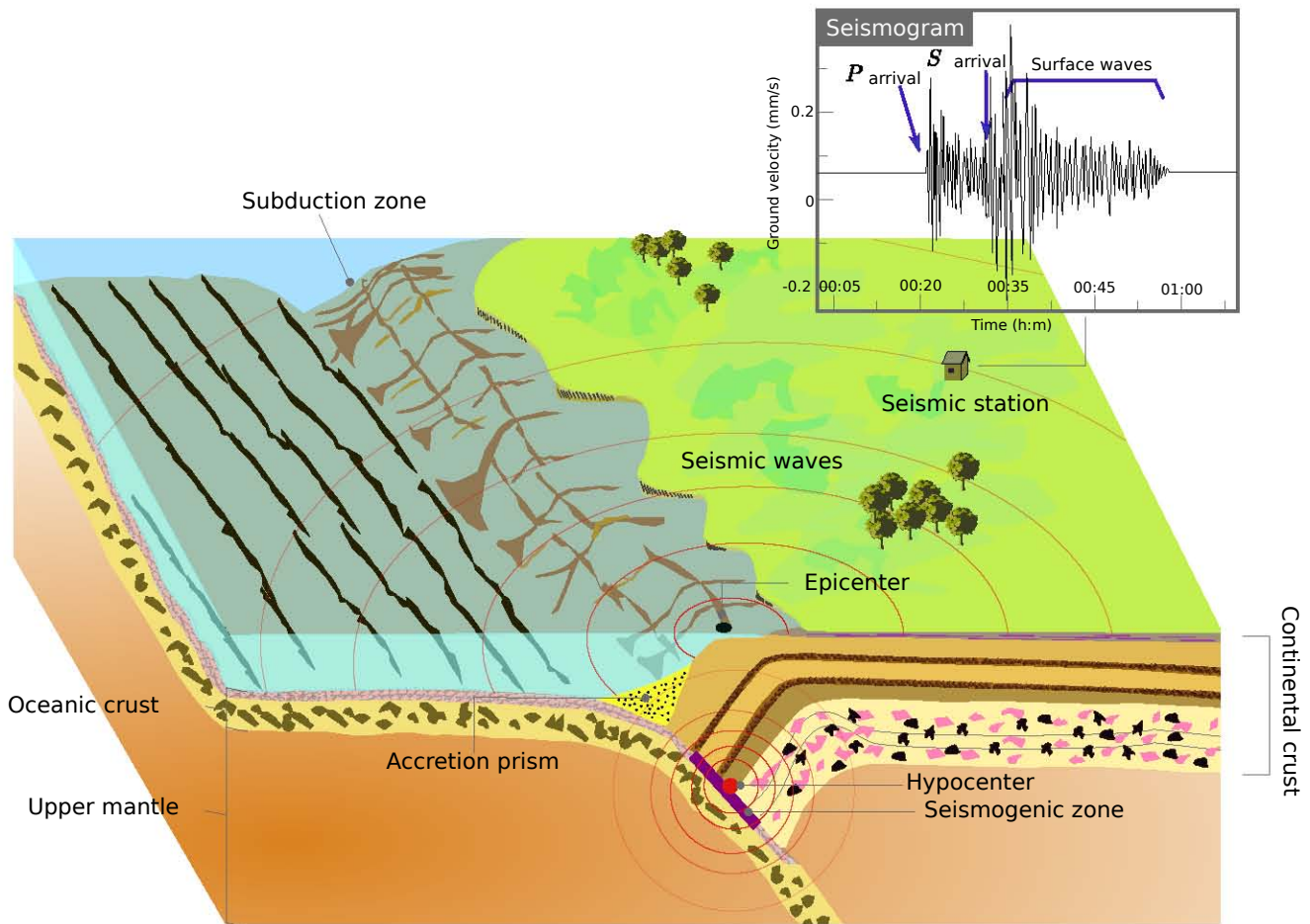


Figure 2.5. Model of a subduction zone. Great earthquakes occur in these regions. The sudden release of accumulated tension between two blocks produces seismic waves, which can be recorded by a seismograph.

2.3 Seismic cycle

Gilbert's (1884) observations of geologic faults in the Great Basin region (United States) were the first approach to the concept of a seismic cycle (SC). The escarpments that protruded from orogenic structures were due to relative sliding between two tectonic blocks. He recognized that the displacement of the continental blocks occurred slowly, and when the friction blocking the contact between the two plates was overcome, an earthquake was triggered.

In 1906, the San Francisco earthquake occurred, one of the most catastrophic events in the United States, forcing the government to create a commission to investigate the origin of such an earthquake. Then, Reid (1911) condensed the hypotheses that had been proposed since Gilbert's ideas, such as the "theory of elastic rebound". In this theory, the Earth's crust is elastic. The displacement on a fault occurs slowly, accumulating stress until, at a given moment, the friction between both sides is overcome, allowing deformation to continue and triggering an earthquake. Once the release of elastic energy is completed, relaxation occurs and

subsequently returns to the initial position, restarting another seismic cycle (Scholz, 2019).

The process of elastic deformation of the crust that occurs between each earthquake was summarized by Mescherikov (1968) in the following stages:

- Slow deformation (secular)
- Preseismic movement (indicate an imminent strong earthquake)
- Earthquake occurrence: the moment when elastic energy is released

The above processes did not take into account other phenomena that have been observed before and after a mainshock, which may be seismic inactivity (Wyss and Habermann, 1988), foreshocks (Jones and Molnar, 1979), and aftershocks (Das and Henry, 2003). Considering the above aspects, the seismic cycle model is based on the following stages (Figure 2.6): interseismic, preseismic, coseismic, and postseismic.

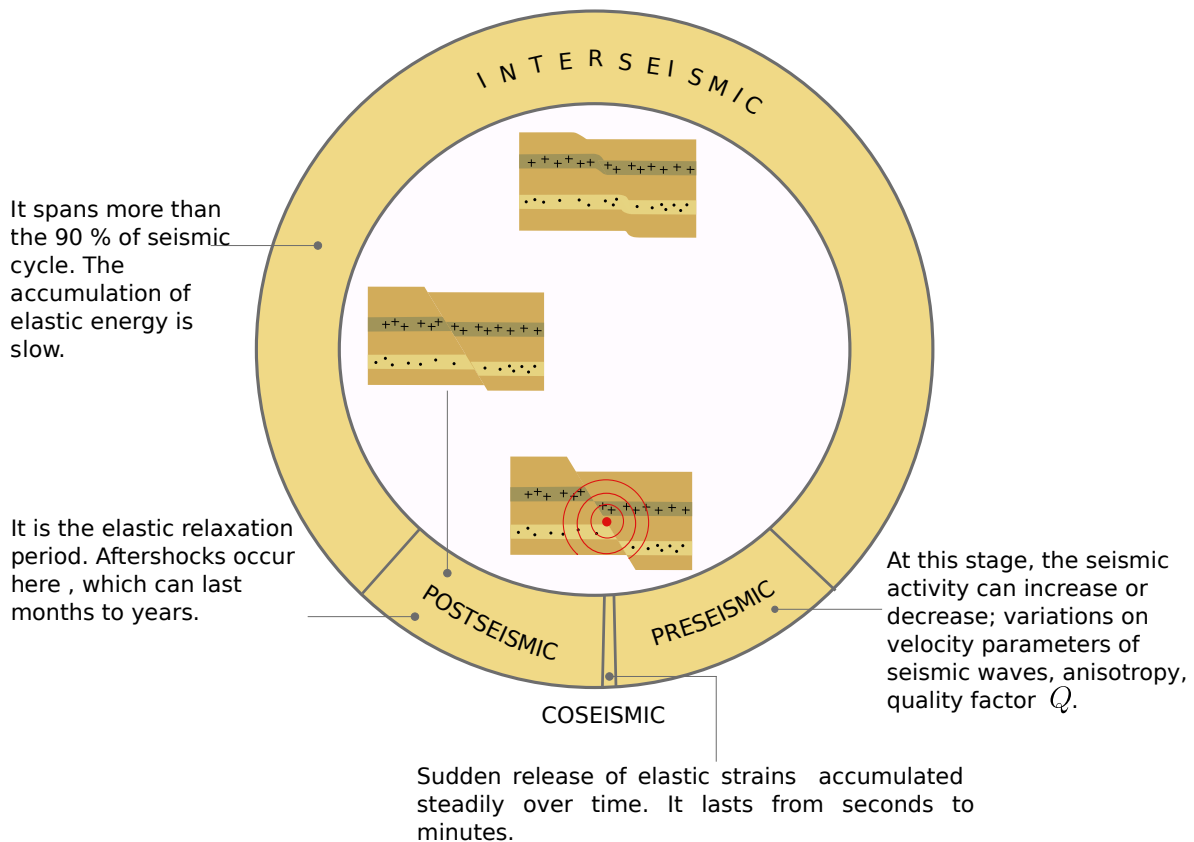


Figure 2.6. Schematic diagram showing the stages of the seismic cycle.

The usefulness of the SC for estimating large earthquakes is that these events are thought to occur at quasi-periodic intervals, which are called as “recurrence times”. According to the seismic gap hypothesis (Fedotov, 1965), the largest magnitude event that has occurred in a

particular area can be considered a characteristic earthquake⁸. The main conditions for the characteristic earthquake are: (1) rupture the entire area of a segment without crossing the boundaries⁹, (2) the rupture leads to a return to a state of base stress, and (3) the process occurs while ignoring the effects of other earthquakes.

Thus, the seismic cycle has helped to understand, in very general terms, the possible occurrence of the next earthquake. However, it should be kept in mind that this periodicity occurs in an ideal context. Therefore, many factors would affect the seismic cycle model. Brace and Byerlee (1966) proposed that these factors are asperities, fault gouge, and pore fluid pressure, which affect pore fluid friction conditions.

2.4 Slow slip events

The energy release mechanism of slow slip events in subduction zones is similar to that of regular earthquakes: During the interseismic period, the oceanic plate is subducting beneath the continental plate, causing the latter to move in the same direction due to collisional shortening, but during the energy release phase, the direction of continental plate displacement is reversed (see Figure 2.7). However, the failure mechanism that triggers a slow slip event is not the same as that of a conventional earthquake and is not yet fully understood.

The discovery of slow earthquakes was attributed to the work of Hirose et al. (1999), who found this type of slow deformation in the Bungo Channel by analyzing GPS measurements. He called this deformation pattern a slow reverse event, in which the stress accumulated in the subduction zones was supposed to be released, just as in a conventional earthquake, but over a more extended period.

Slow earthquakes were previously known for their low frequency and long duration. Hirose et al. (1999) concluded that these unusual events were related to the earthquakes described by Beroza and Jordan (1990). Dragert et al. (2001) studied slow slip events occurring every 13 to 16 months in the Cascadia subduction zone. Dragert et al. (2004) later analyzed more extended GPS time series and found a correlation between episodic nonvolcanic tremor and slip events (ETS).

On the other hand, while most of the slow slip events have been identified in subduction zones, there are two exceptions, for example: (1) on the San Andreas Fault (continental fault zone), Linde et al. (1996) reported slow deformation with borehole measurements; (2) in Hawaii

⁸The other two prediction models are the time-predicted earthquake and the predicted slip earthquake (see Shimazaki and Nakata, 1980).

⁹The segments adjacent to the central segment jumped during the Landers earthquake (1992). Since then, the interaction between segment boundaries has been considered (WGCEP, 1995).

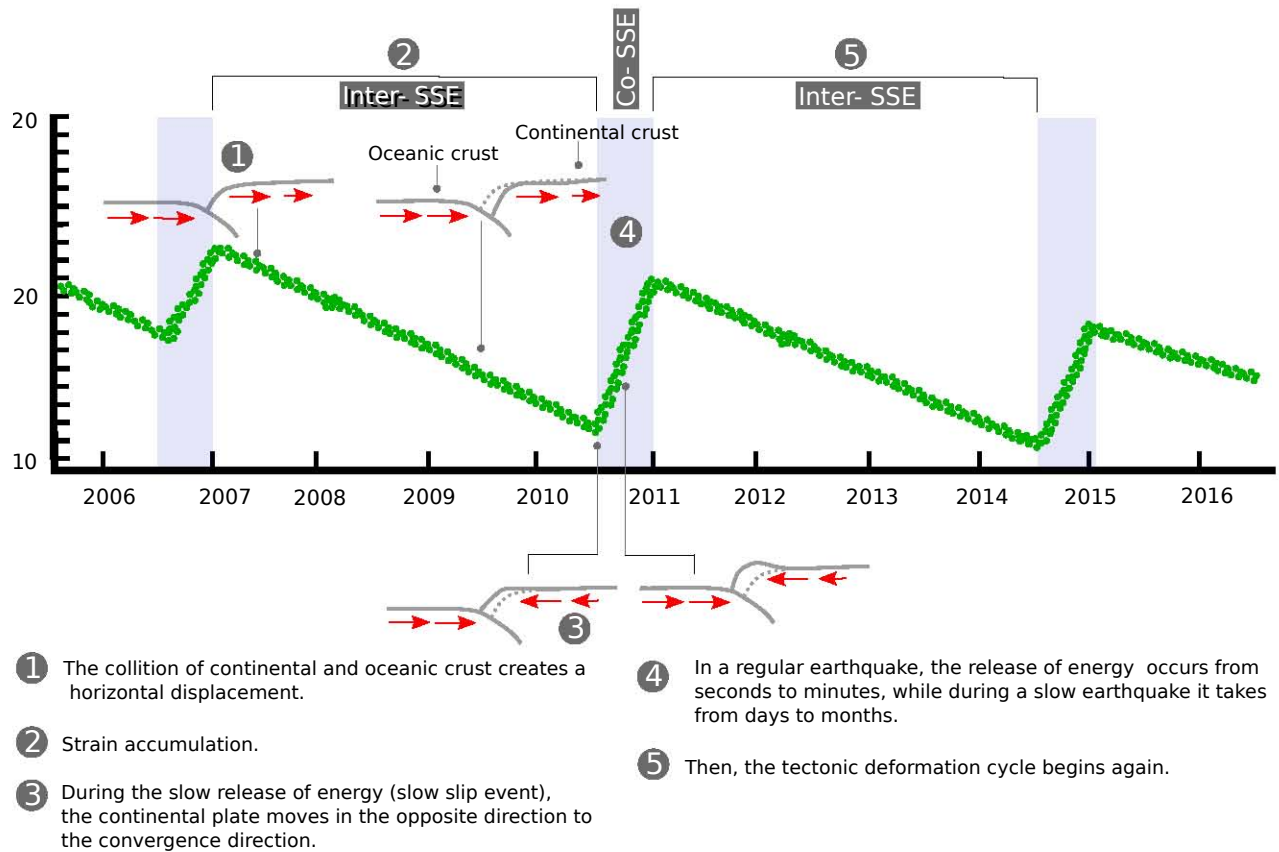


Figure 2.7. Synthetic horizontal GPS displacement showing three slow slip events with a recurrence interval of 3.5 years and a duration of 6 months. The stages of a slow earthquake are very similar to those of a regular earthquake, but the release of stress takes days to months.

(volcanic structure), Cervelli et al. (2002) identified an aseismic event with a duration of 36 hours and a magnitude of M_W 5.7. In contrast, slow earthquakes in subduction zones mainly occur deeper than the lower part of the seismogenic zone (Figure 2.8). They can also take place in the upper part (LaBonte et al., 2009) of the seismic zone or within it (Sagiya, 2004), although the latter is rare.

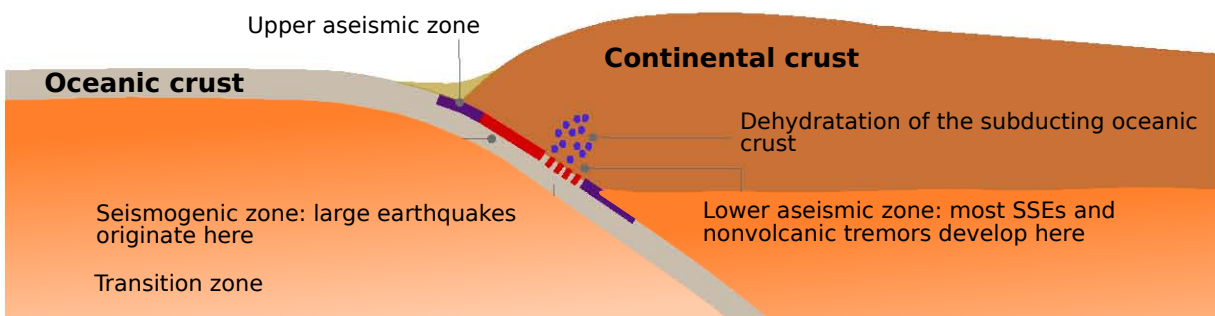


Figure 2.8. Illustration of a seismogenic zone at a convergent plate boundary. Source: Hyndman et al. (1997) and Schwartz and Rokosky (2007).

2.4.1 Slow slip events in the Guerrero seismic gap

The factors that cause SSEs in Guerrero and other subduction zones are thought to be fluid migration through porous media (Figure 2.9) caused by dehydrating minerals (Fujii and Kumazawa, 2010).

The slow earthquakes that occur in the Guerrero seismic gap are characterized by a recurrence period of 3.5 to 4 years and an average duration of 6 months (Figure 2.10), cataloged within the longest in the world (Radiguet et al., 2012). They can release tectonic stresses equivalent to an M_W 7.5 earthquake¹⁰ (Frank and Brodsky, 2019). Although this recurrence period (estimated for 1997 to 2017) has changed due to seismotectonic effects of the 2017 M_W 8.2 Tehuantepec earthquake (Figure 2.10), since then, the recurrence interval between slow slip events has ranged from 0.25 to 0.5 years (Cruz-Atienza et al., 2021).

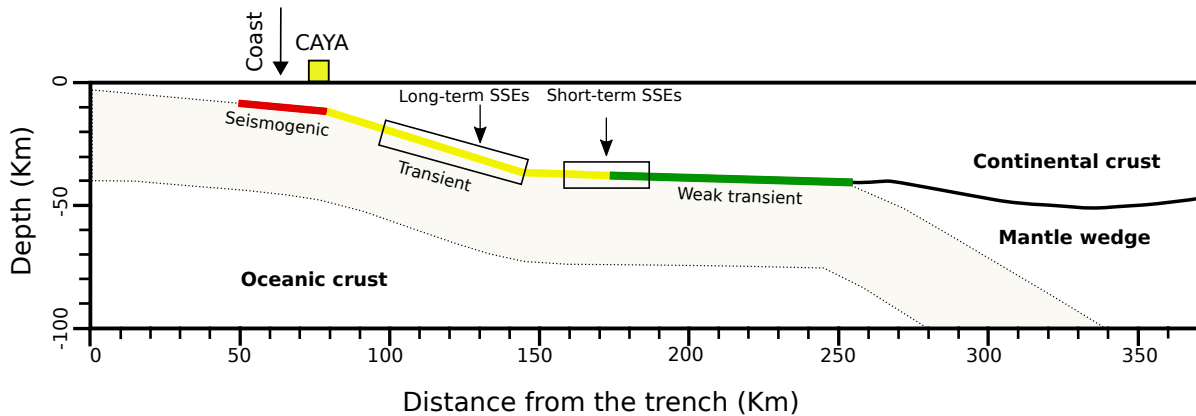


Figure 2.9. Geometry of the subduction zone of the Cocos plate under the North American plate. The location of slow slip events is consistent with an ultra-slow layer (Kim et al., 2010). Adapted from Kostoglodov et al. (2010).

¹⁰The moment magnitude of a slow earthquake can be estimated by inverting GPS data to calculate the rupture area and its average slip.

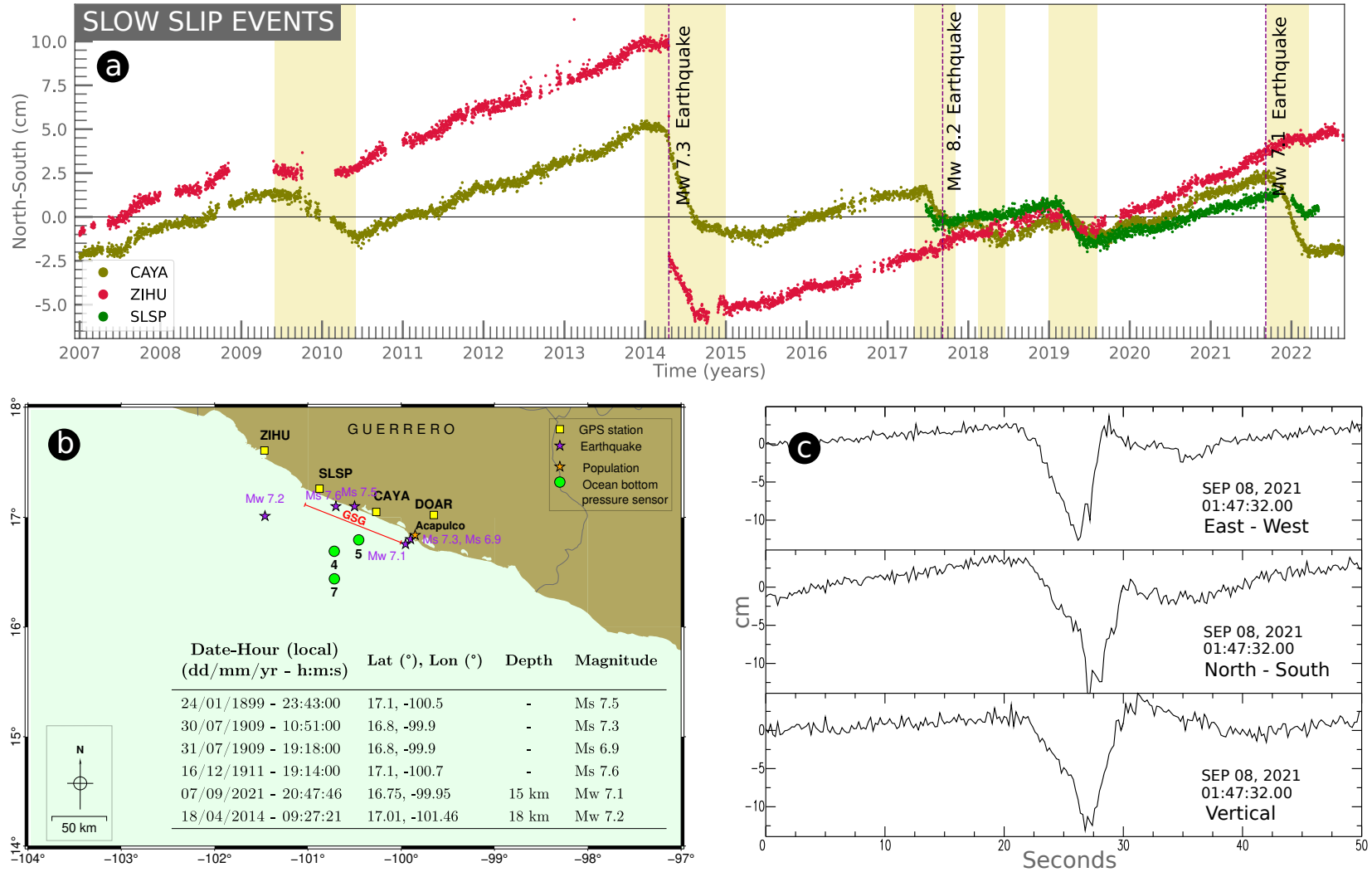


Figure 2.10. Slow slip events recorded in the North-South GPS component. (a) The 2018 slow event was only recorded at the CAYA and SLSP GPS stations. (b) Map of the location of the GPS stations operated by the Departamento de Sismología and Servicio Sismológico Nacional. The largest earthquakes (see Table in b) in the Guerrero seismic gap, the epicenter of the 2014 Papapanoa earthquake, the 2021 Acapulco earthquake, and other epicenters (SSN, 2023) are shown in map (b). (c) GPS displacement measurements every second at the DOAR station (see map for reference) show the dynamic signal of the 2021 M_W 7.1 Acapulco earthquake.

OCEANOGRAPHIC AND METEOROLOGICAL EFFECTS ON SEA LEVEL

CHAPTER 3

3.1 Sea level

The mean sea level (MSL) is obtained by averaging a sea level time series of at least a month or a year (PSMSL, 2023). Although these observation periods help obtain an approximate mean sea level value, a time series of approximately 19 years of data is preferably used for geodetic prospecting purposes. Moreover, sea level measurements are relative to a reference point known as the tidal datum (zero level). The sea level depends on gravitational forces exerted by the Moon (most significant contributor) and the Sun (minor contributor). Other factors, such as meteorological and oceanographic effects, can also cause perturbations in sea level heights.

3.1.1 Tsunamis

The word tsunami comes from the Japanese language, *tsu*, port, *nami*, wave, which means harbor waves. The name was derived from the observation of large waves that crashed into Japanese ports. Tsunamis can be caused by submarine earthquakes or seismic events nucleated at subduction zones, which move a portion of water, generating waves that can reach the coast. Notable examples are: the M_W 9.2 Alaska earthquake (March 27, 1964), when the tsunami waves reached Kodiak Island 30 minutes later (Grantz et al., 1964); the M_W 9.6 Chile earthquake (May 22, 1960), the strongest event recorded by modern instruments, broke a fault area of $1,000 \text{ km} \times 150 \text{ km}$, causing a tsunami that crossed the Pacific until arriving in 15 hours at the port of Hilo, Hawaii. In the tsunami, the waves rose to 10 meters (Eaton et al., 1961), and in Japan, they reached up to 4 meters (Atwater et al., 2001).

Volcanic eruptions may also cause tsunamis due to strong explosions or landslides from volcanic structures. For example, the 1883 volcanic eruption of Krakatoa (Ritter Island), one of the deadliest volcanic eruptions in history, started with intense seismic activity and emitted

four eruptions. With subsequent tsunami generation (Pelinovsky et al., 2005). The tsunami signal was recorded in tide gauges in India, Indonesia, and Pakistan (Figure 3.1).

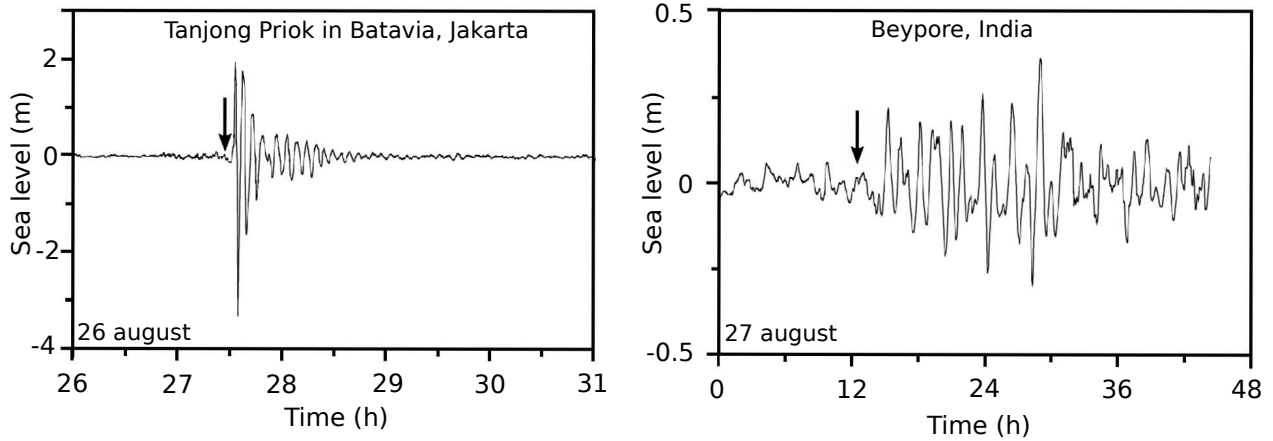


Figure 3.1. Record of the tsunami waves (black arrow shows the initial moment of the tsunami) from the 1883 Krakatoa eruption in tide gauge records from Beypore (India), and Batavia (Jakarta). The sea level time series were detided. Adapted from Pelinovsky et al. (2005).

3.1.2 Atmospheric pressure variations

The fluctuations of the free surface of the sea caused by variations in atmospheric pressure can be explained explained by the inverted barometer effect¹ (IB). The mechanism consists of a system of high pressure that causes a decrease in the sea level height, while low pressure is reflected in an increase in sea level (Figure 3.2). Then, IB can be described by the following equation (Vaníček, 1978):

$$\eta = \frac{(P_0 - P_{obs})}{\rho_{sw} g} \quad (3.1)$$

where

η = Sea level change

P_0 = Mean atmospheric pressure

P_{obs} = Atmospheric pressure at the sea level

ρ_{sw} = Seawater density

Assuming that the atmospheric pressure remains constant and that the density change is negligible concerning the compressibility of water, it is possible to use Equation 3.1 to calculate

¹The inverted barometer effect was first identified by Gisler in 1747, who observed the impact of atmospheric pressure fluctuations on sea level changes. Subsequently, it was studied by Ross (1854).

the pressure variation over time (Pugh, 1996). Redefining Equation 3.1 with the values of $g = 9.81 \frac{m}{s^2}$, and $\rho_{sw}=1027 \frac{Kg}{m^3}$:

$$\eta = 0.9936 (P_0 - P_{obs}) \quad (3.2)$$

A change in the height of the seawater column (η) is in centimeters, while $P_0 - P_{obs}$ in millibars.

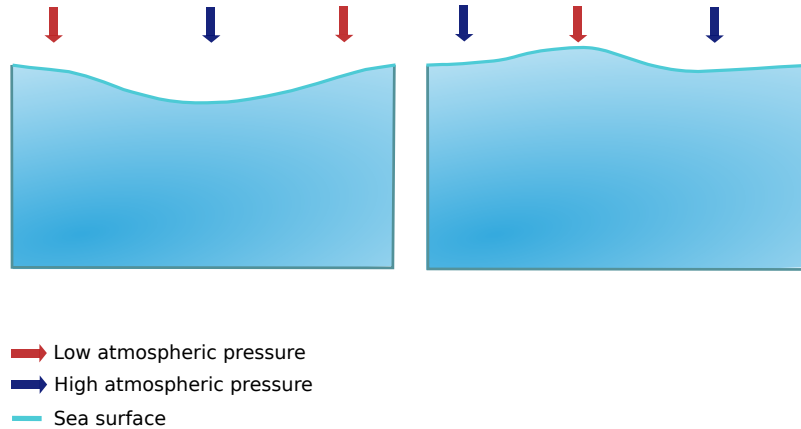


Figure 3.2. Illustration of the inverted barometer effect on the surface of sea level.

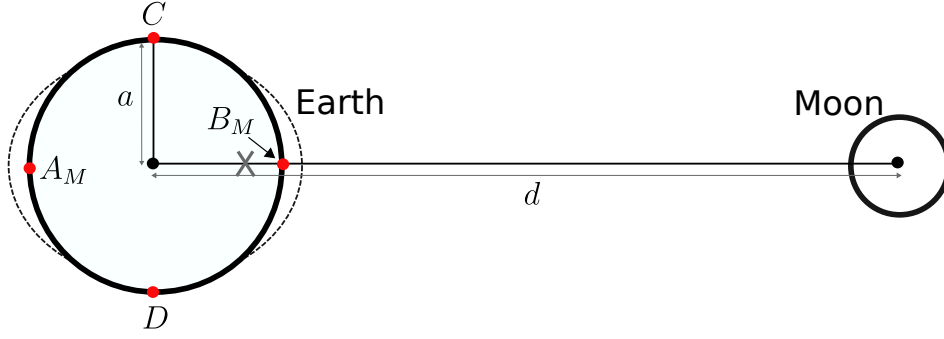
3.1.3 Tides

Tides are sea level fluctuations (fall and rise) caused by changes in the Earth’s gravitational field, which are mainly influenced by the Sun and the Moon. Hence, they are also called gravitational or astronomical tides. One of the main characteristics distinguishing the astronomical tide from the meteorological tide is its periodicity. The instrument that measures sea level is called a tide gauge (see Figure 3.9), and its record is called a marigram.

The equation for the generating forces of tides is derived from Newton’s law of gravitation; as its name indicates, it is the gravitational attraction of celestial bodies on the ocean surface, mainly the Moon and Sun. Notably, although the Sun is larger than the Moon, its gravitational contribution is less because the Earth-Sun distance is much greater than the Earth-Moon distance. The force F that the Moon (Sun) exerts on the Earth can be represented according to Newton’s law of gravitation as:

$$F = G \frac{m_E m_M}{d^2} \quad (3.3)$$

m_E and m_M are the masses of the Earth and Moon, respectively; G is the universal gravitation constant; d is the distance between the centers of mass of the two bodies. The tide-generating force on the sub-lunar point B (Figure 3.3) is defined as the difference between the gravitational



- Arbitrary point
- Center of mass
- × Center of mass (gravitational) of the Earth-Moon system.
- A_M B_M Antipodal and sub-lunar point, respectively
- Tidal bulge

Figure 3.3. The influence of the Moon's gravitational force on the sea surface. Adapted from Pugh and Woodworth (2014).

force exerted by the Moon to the Earth's center and the force on a surface point of itself. Following Pugh and Woodworth (2014):

$$\begin{aligned}
 FM_B &= G \frac{m_E m_M}{(d-a)^2} - G \frac{m_E m_M}{d^2} \\
 &= G \frac{m_E m_M}{d^2} \left[\frac{d^2 - (d-a)^2}{(d-a)^2} \right] \\
 &= G \frac{m_E m_M}{d^2} \left[\frac{1}{(1-\frac{a}{d})^2} - 1 \right] \tag{3.4}
 \end{aligned}$$

the ratio of the Earth's radius a and the Earth-Moon distance d is approximately $\frac{1}{60}$, so it follows that:

$$\left[\frac{a}{d} \right]^2 \ll 1 \tag{3.5}$$

By approximating $[1/(1-\alpha)^2] \approx (1+2\alpha)$ it is concluded that:

$$FM_B = \frac{2 G m_E m_M a}{d^3} \tag{3.6}$$

similarly, we have for the antipodal point A :

$$FM_A = -\frac{2 G m_E m_M a}{d^3} \tag{3.7}$$

The previous model considers that the Earth is covered by water (continents do not exist), the friction between the layers of water is negligible, and the position of the Moon is aligned

with the terrestrial Equator (there is no declination). Consequently, the lunar gravitational force is instantaneous on the ocean surface, producing two tidal bulges: one toward the Moon (sub-lunar point) and one on the opposite side (antipodal point). At points A_M and B_M in Figure 3.3, the tide increases (high tide), while at points C and D , the tide has a fall (low tide). Because the Earth rotates every 24 hours, we would have semidiurnal tidal patterns (Figure 3.4). The previous descriptions refer to the equilibrium tide.

On Earth, under the conditions described above (the Moon orbiting in alignment with the terrestrial equator), there would be two low tides of equal amplitude and two high tides of equal amplitude (in one lunar day). However, given the actual conditions—i.e., the Moon’s orbit varying from north to south of the terrestrial equator in 27.21 days, and the distribution of the continents distorting the flow of water—the heights are unequal. If there is one low tide and one high tide during the day, the tidal pattern is diurnal. However, if the record shows a pronounced inequality between the low and high tides, the tidal regime is mixed (Figure 3.5).

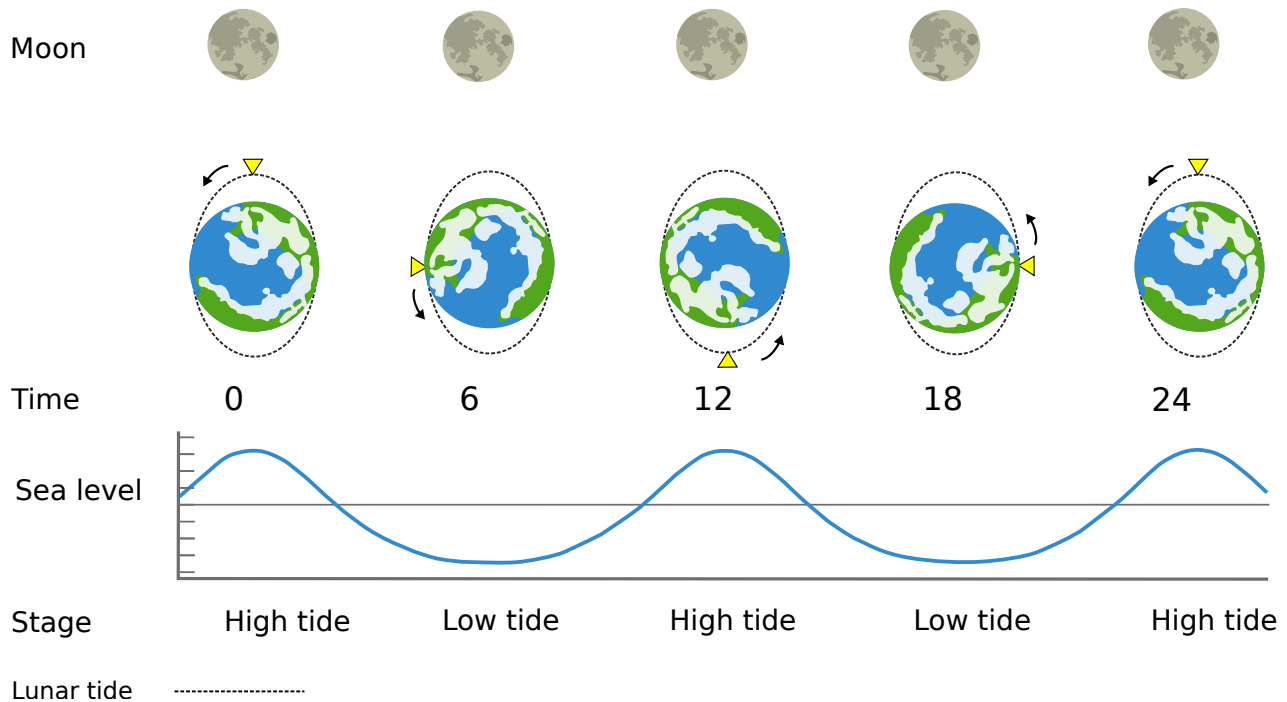


Figure 3.4. Semidiurnal tidal pattern. On a solar day (triangle yellow), the same site experiences two low tides and two high tides. Adapted from Sumich and Morrissey (2004).

The cycle of spring and neap tides: planetary alignment

The translation movement of the Moon around the Earth generates 4 Moon phases (Figure 3.6): new Moon, first quarter, full Moon, and third quarter. The alignment of the principal tide-generating bodies is clearly reflected in a one-month tide chart (Figure 3.4). The superposition

of the Sun and Moon causes spring tides (Figure 3.6). While in quadrature alignment (i.e., 90°), the gravitational forces are reduced when they cancel out, thus producing lower than average tides, known as neap tides.

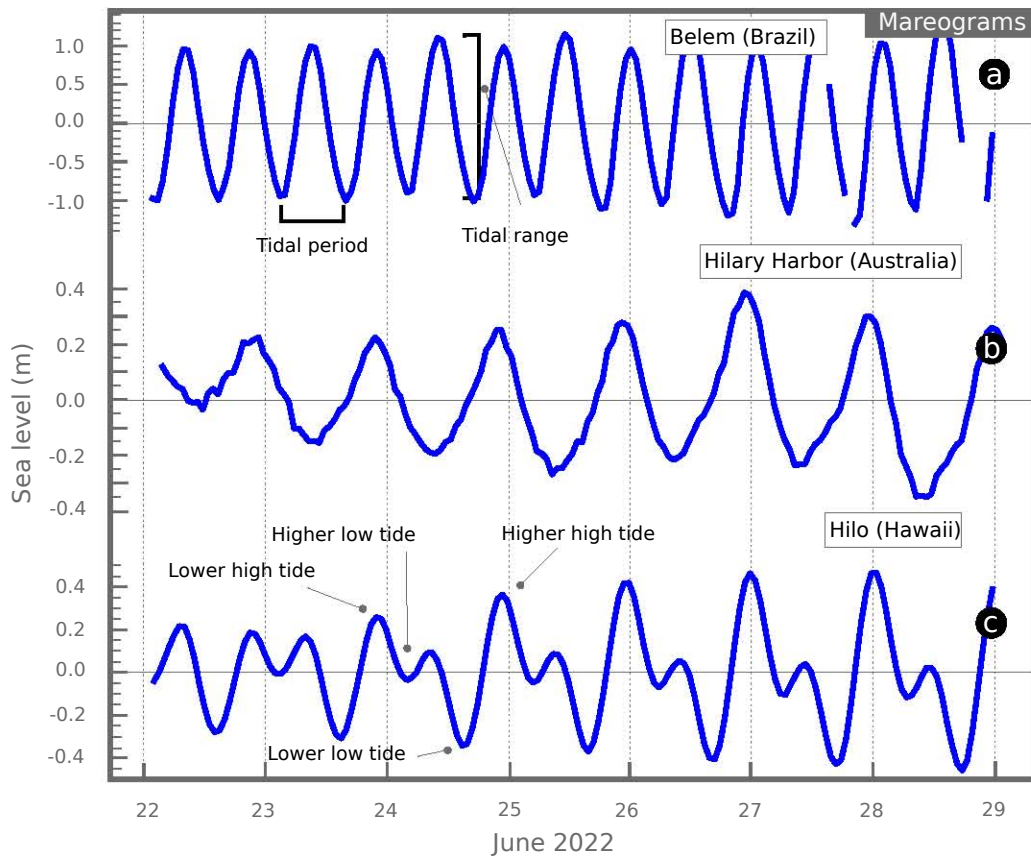


Figure 3.5. Tidal patterns. (a) Semidiurnal tides; (b) Diurnal tides; (c) Mixed tides. Source: PSMSL (2023).

3.1.4 El Niño-Southern Oscillation

El Niño-Southern Oscillation (ENSO) is an oceanographic and meteorological phenomenon that develops in the tropical band of the Pacific Ocean. The term Southern Oscillation² refers to the atmospheric origin of the ENSO, that is, fluctuations in atmospheric pressure that induce changes in the central Pacific (OMM, 2014). The effects of ENSO are the increase in temperature in the Eastern and Central Pacific and the decrease in temperature in the Western Pacific (Figure 3.7). Consequently, trade winds are weakened by changes in pressure. The rainfall pattern is modified: The rainy season in Indonesia decreases drastically, with the consequent transfer of rainfall to the Eastern and Central Pacific.

²Sir Gilbert Walker discovered the Southern Oscillation (SO). Walker (1924) and Bjerknes (1969) concluded that this weather pattern kept close to the occurrence of El Niño.

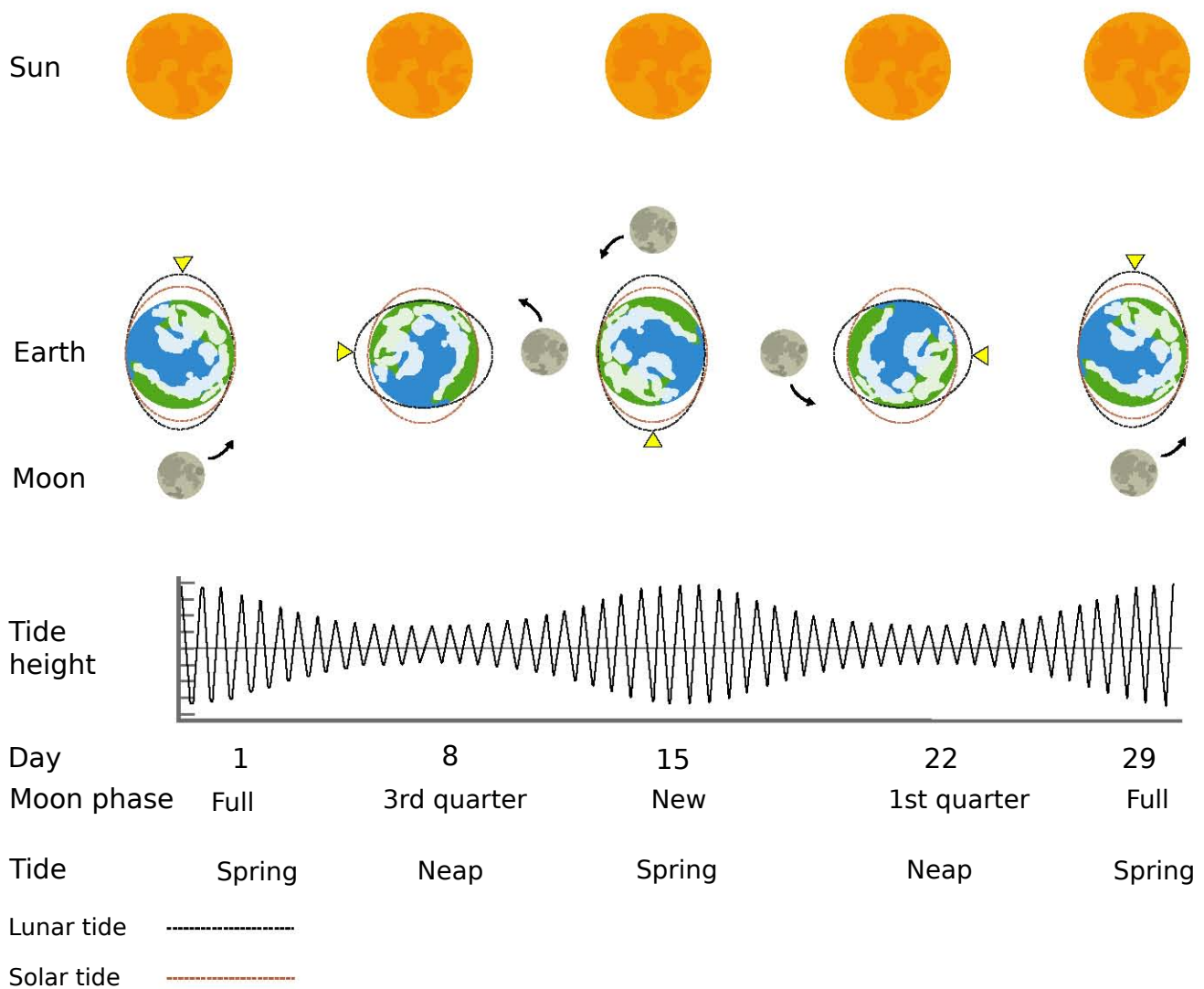


Figure 3.6. The alignment between the Sun, Earth, and Moon produces an additional weekly tidal variation. Adapted from Sumich and Morrissey (2004).

Under normal conditions, trade winds move from the high-pressure region³ (HPR) to the low-pressure region (LPR). This movement generates the Walker cells (Figure 3.7), which carry cold air from the HPR to the LPR. Once the air reaches the low-pressure region, it ascends and moves toward the Eastern Pacific, thereby completing the cycle. If the temperature decreases in the East Pacific (EP), that is, the region becomes colder than usual, the system causes heavy rains in the West Pacific (WP) and severe droughts in the EP. The above phenomenon is known as La Niña (see Appendix D). ENSO period is quasi-periodic, from 3 to 7 years (Wang et al., 2017) and can last for 18 months. To measure it, the Southern Oscillation Index (SOI) is calculated, which is the difference in the pressure anomaly between Tahiti (French Polynesia)

³Delimited by the region between the coast of South America and 140°W, spanning approximately from 3°N to 15°S. (Cane, 1983).

and Darwin (Australia). If the fluctuations in a SOI time series are negative, then this is a warning phase or El Niño; on the other hand, positive values indicate a cold phase or La Niña. Values close to zero indicate stability (NOAA, 2023).

Trade winds can rise sea level by up to a meter in the Western Pacific. When their velocity is reduced, the equatorial upwelling on the southern coast of America decreases. Some studies have shown that the effect of ENSO on sea level is very evident; for example, Cane (1983) analyzed the sea level time series of tide gauges located in Rabaul, Fanning, Santa Cruz, and Callao for the period 1982-1983, in which occurred one of the most strong ENSOs, and clearly shows the negative and positive fluctuations of sea level height (Figure 3.8). Moreover, Enfield and Allen (1980) analyzed changes in meridional sea level, temperature, and wind stress at 19 sites (from Yakutat, Alaska, to Valparaiso, Chile); sea level measurements from the Galapagos Islands, Talara, and Callao showed the most significant correlations with the ENSO signals from 1950 to 1974.

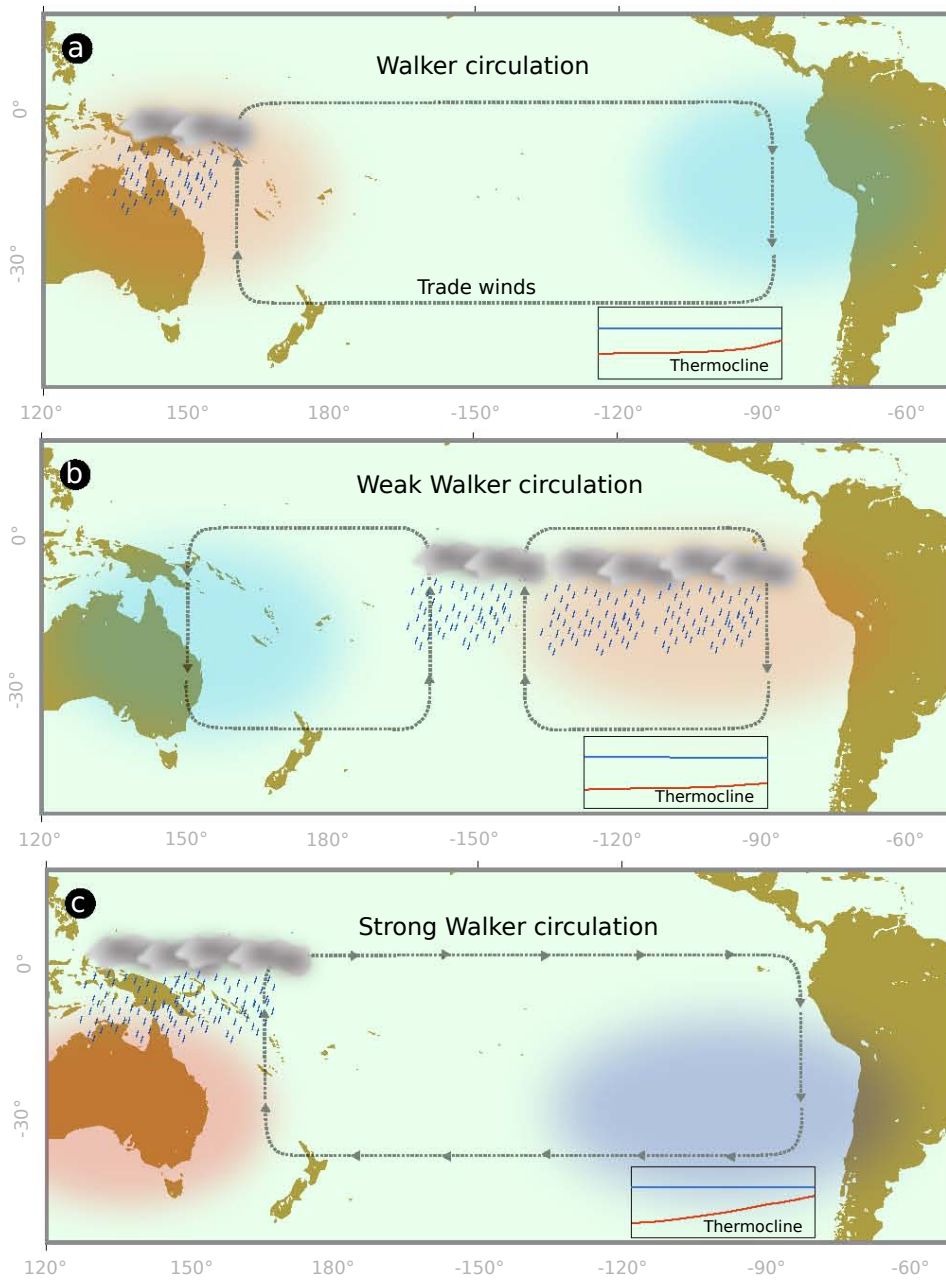


Figure 3.7. Illustration of the East and West Pacific temperature distributions. (a) Walker circulation under neutral conditions. During El Niño, the conditions in (a) are reversed. (c) The La Niña phase develops when the Eastern Pacific is colder, and the Western Pacific is warmer. Gray arrows indicate vertical air circulation.

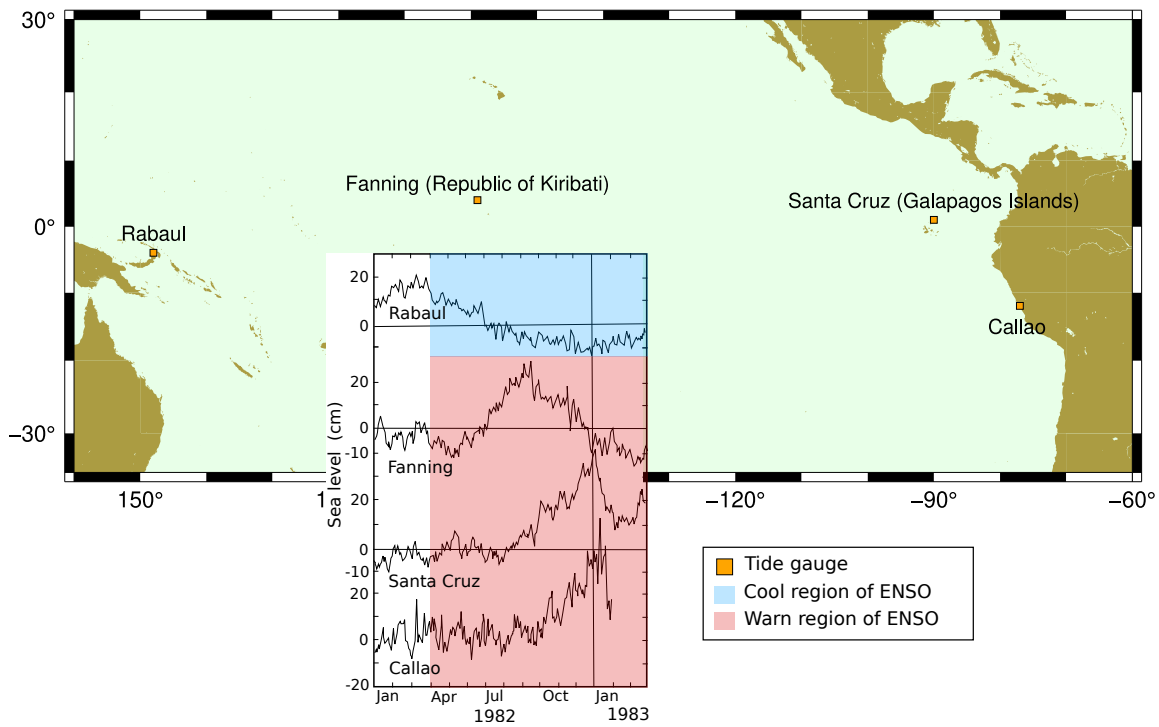


Figure 3.8. El Niño-Southern Oscillation of 1982-1983 was recorded in tide gauge measurements. Note the rise in sea level at the Rabaul tide gauge (warm region); in contrast, a decrease is apparent at the Flanning, Santa Cruz, and Callao tide gauges (cold region). Modified from Cane (1983).

3.1.5 Storm surges

The elevation or depression of the sea surface, lasting for hours or days, can also be caused by the tangential stress of strong winds associated with a storm (Heaps, 1983). In extreme meteorological conditions, wind piles up water above mean sea level (MSL); conversely, MSL decreases if the wind direction is toward the sea (Lisitzin, 1974).

Among the factors that tend to increase or decrease the intensity of storm surges on coasts, we have (1) the dimension of the coast (width and length) as well as its slope (abrupt and shallow); (2) the coincidence with high astronomical tide, causing the level to rise above average conditions. The above phenomenon is called storm tide; (3) If the coastal geomorphology is open or concave. In normal weather conditions, the influence of the wind will always or almost always disturb the surface of sea level (e.g., formation of waves). Therefore, phenomena such as cyclones constitute the leading cause of the elevated sea level on coast. According to the latitude at which they develop, they can be classified as follows:

- Tropical cyclones: They occur between the tropics of Capricorn and Cancer and are characterized by very low-pressure systems (below 950 mb) with strong winds (Paul and Rashid, 2017). They last 2 to 5 days (Von Storch and Woth, 2008).
- Extra-tropical cyclones (frontal cyclones or temperate cyclones): They develop between the strips delimited by latitudes 30° - 60° (S and N), and they cause storm surges lasting from several hours to half a day, which can affect coastlines of 200 km in length (Von Storch and Woth, 2008).

Regarding the direction of rotation, the cyclonic flow is counterclockwise in the Northern Hemisphere, whereas it is clockwise in the Southern Hemisphere. In addition, the atmospheric evolution of cyclones is usually hurricanes (see Appendix E).

3.2 Sea level measurement

3.2.1 Tide gauges

The measurement of sea level began with maritime activity linked to the trade of emerging civilizations; since the surface level fluctuated periodically, knowledge of this helped the embarkation of ships and the construction of ports. One of the instruments invented was a vertical rule attached to port buildings, and hence, the water level was marked on it. In ancient Egypt, its use helped warn of the flooding of the Nile River; these measurements were recorded on stone tables (Matthäus, 1970). The disadvantage of these instruments is that data collection has to be conducted by a person at every time interval, and the measurements may be affected by the currents and their precision.

Stilling-well gauges

Because of the need for sea level measurements throughout the year and the difficulty of taking readings, the first tide gauge was built in 1831 by engineer Henry R. Palmer and installed in the Thames estuary (Matthäus, 1972). The mechanism was based on a float tied by a chain to various gears, which were connected to a pencil that recorded the vertical movements of the float. This tide gauge had a clock system. The tube that protected the sensor (float) acted as a filter that prevented high frequencies, such as seiches and currents.

The errors associated with the float system may be due to the change in density of the water inside and outside the tube, which occurs if the tide gauge is located in estuaries, since this type of water body is very sensitive to weather conditions (Savenije, 2005). Another factor is the accumulation of sediment inside the tube, reflecting in a flat low tide, because the float goes down until it touches the sediment clump (Hannah, 2011).

By 1980, sea-level recording mechanisms had transitioned from analog to digital. Consequently, the sea level records on paper were digitized for later incorporation into historical records and re-processing (Emery and Aubrey, 1991).

Acoustic gauges

The measurement principle of acoustic tide gauges is the emission of acoustic waves, are instantly reflected from the sea surface. The signal is protected with a tube that joins the tide gauge with the surface. However, with such support, it is not possible to remove high frequencies, as occurs with stilling-well gauge, so the readings obtained are averaged to obtain a filtered values (IOC, 2006).

Radar gauges

Radar tide gauges are classified according to how they transmit electromagnetic signals (Woodworth et al., 2016): frequency-modulated continuous-wave radar (FMCWR) and pulse radar (PR). In the FMCWR, as its name implies, the emission is a continuous electromagnetic wave when colliding with the sea surface; if it is stationary, the return signal will be of the same frequency. The opposite occurs when the object is mobile (Devine, 2000). The highest return frequency is interpreted as a near-surface (high tide), and a low frequency as a far-surface (low tide). For pulse radar tide gauges, short wave packets lasting milliseconds or nanoseconds are emitted, and when bouncing off the sea surface, return in a determined time (Figure 3.9). The travel time is multiplied by the speed of light and divided by two (similar method to altimetry, see section 3.2.3), obtaining the distance from sea level (Devine, 2000).

Reference point: tide gauge benchmark

Sea level heights obtained using the tide gauges mentioned above are relative (Figure 3.9). In other words, they are related to a tide gauge benchmark (zero level). These points can be represented by metal plates or similar objects on rocky soil (Woodworth et al., 2017). The set of references is part of a more extensive geodesic network. They are usually calibrated regularly if they are located on unstable locations (Woodworth et al., 2016). Then, another reference point connects the tide gauge benchmark to this geodesic network. Other parameters used as reference levels are the average of a long sea level time series (generally 19 years), the recorded lowest tide, or a chart datum.

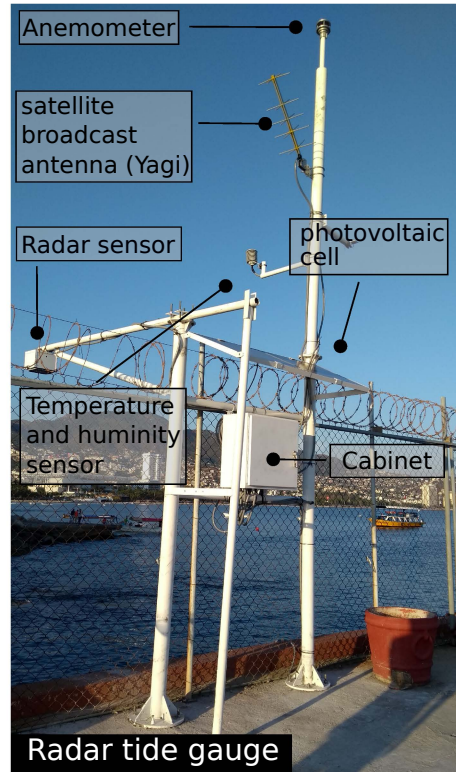
3.2.2 Ocean-bottom pressure sensors

The study of offshore tides was one of the oceanographers' initiatives of the XX century, and it presented some challenges due to the complexity of the marine environment. Pettersson (1925) suggested installing a tide gauge in the sea, which would be fixed to a subsurface buoy (simulating an "artificial island"). Additionally, it could record other parameters, such as pressure, current, and temperature. Therefore, to measure the tides under these conditions, Collar and Cartwright (1972) recorded tidal patterns using strain gauges installed on the western and northern continental shelf of Great Britain; Filloux (1971) obtained a 7-day record of the pressure fluctuations at a depth of 4.4 km with the help of a Bourdon tube pressure transducer, 1,150 km off the coast of Baja California.

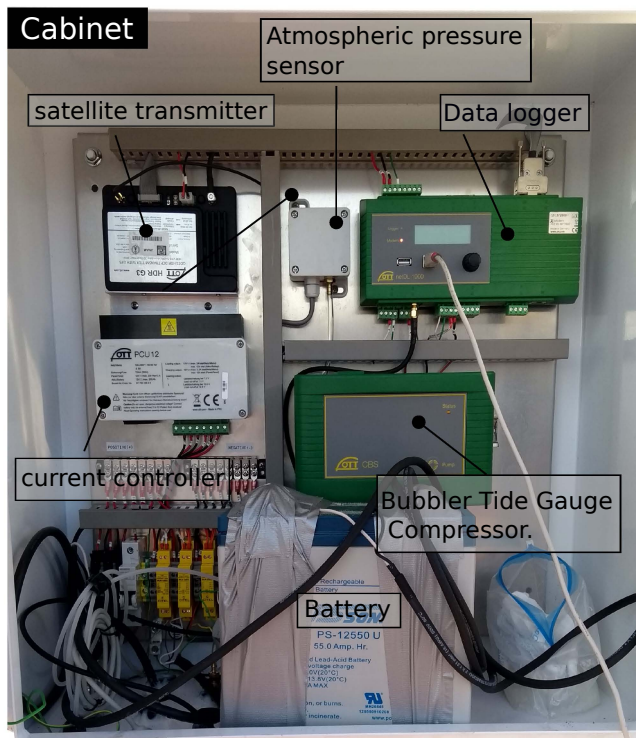
The deployment of seafloor instruments has enabled the recording of additional parameters and oceanographic phenomena, beyond the measurement of bottom pressure. These in-



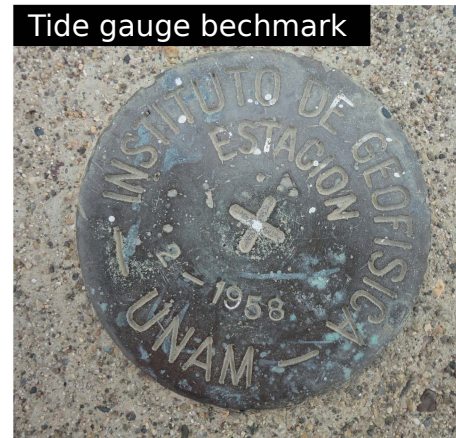
Stilling-well tide gauge



Radar tide gauge



Cabinet



Tide gauge benchmark



Bubbler chamber (bubble tide gauge)



Vertical control of a level benchmark network

Figure 3.9. Some instruments used to measure sea level in Mexico and control of a leveling bench (lower right). Source: photographs by Valente Gutiérrez (SMN, 2024) and José Santiago (IG, 2023).

clude bottom temperature, ocean currents, seismic waves (via ocean-bottom seismometers), and tsunamis. For example, Filloux (1982) recorded the first tsunami using an ocean-bottom pressure sensor located 1,000 km from the Pacific coast of Mexico. As a result, the first network in the Pacific was formed by systems known as DART (Deep-ocean Assessment and Reporting of Tsunamis). These systems are pressure sensors on the seafloor that transmit their information by acoustic telemetry to a buoy on the surface, which transmits the data to a satellite for real-time monitoring.

3.2.3 Satellite altimetry

The idea of launching satellites came from the war context, and the need for military, meteorological, cartographic, and political hegemony pressured governments to invest in space development. As a result, the first satellite⁴ Sputnik 1 (Figure 3.10) was launched on October 4, 1957, then by the USSR (Union of Soviet Socialist Republics). This space mission also consisted of an experiment to measure the variation in electron density in the upper ionosphere (Kuznetsov et al., 2015).

As a result, different fields benefited from the emerging space technology. Oceanography did not benefit until a decade later. It was then that at a conference held in Williamstown, Massachusetts, in 1969, 65 specialists discussed the creation of Satellite Oceanography and simultaneously innovation in satellites for use in the study of Earth Physics (Lundquist, 1970; ESA, 2018). Responding to this proposal, the United States launched the first satellite altimetry in 1973 for oceanographic research (Newkirk and Ertel, 1977): the Skylab. Figure 3.10 illustrates the altimeter releases up to the present.

The basic principle of height measurement of the sea surface (or continental), is the emission of pulses (pulse repetition frequency) to the nadir of the satellite (Figure 3.11), and then the backscattered signal (radar echo) is received by a sensor anchored to the satellite (Chelton et al., 2001). The round-trip time of the signal is used to calculate the distance⁵ between the satellite and the reflective surface (Equation 3.8).

$$R = \frac{c \Delta t}{2} \quad (3.8)$$

R is the altimetric range (satellite-ocean surface distance), c is the speed of light, and Δt is the round travel time of the emitted pulse by the antenna.

Next, the raw data must then be corrected for geodesy and oceanography analyses (Shum et al., 1995). According to Calmant et al. (2016), the main steps can be divided into the

⁴It occurred within the framework of the International Geophysical Year 1957-1958.

⁵Neglecting instrumental and atmospheric effects on travel time.

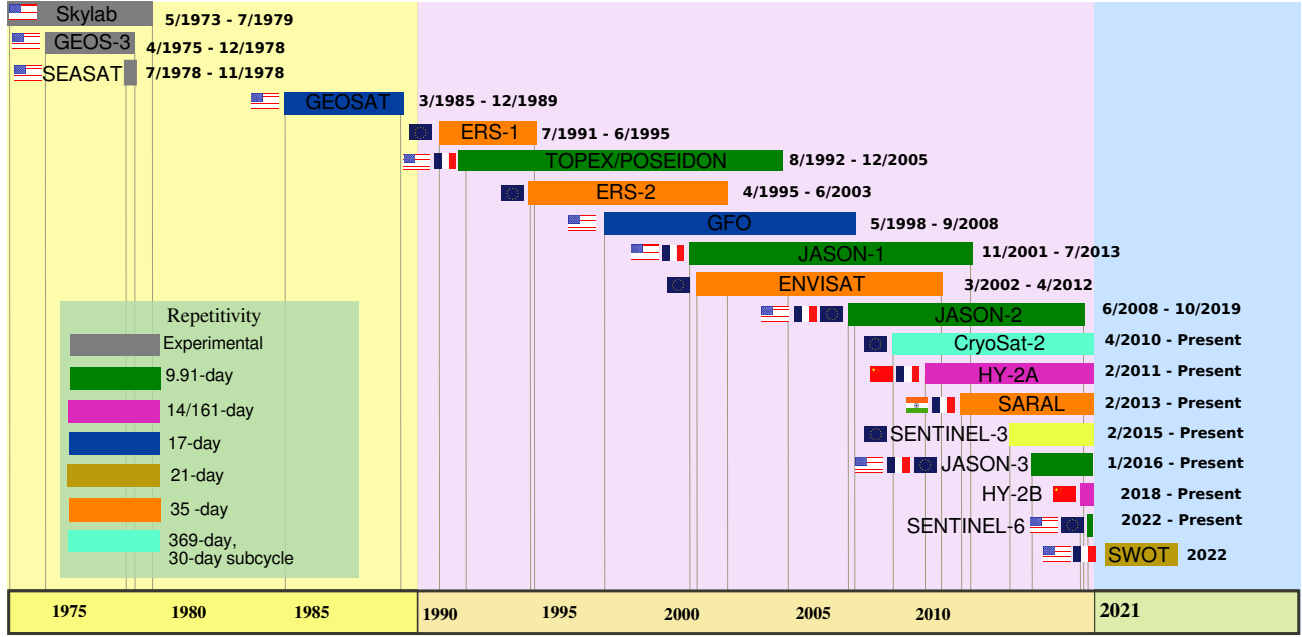


Figure 3.10. Timeline of satellite altimeter missions. Adapted from Grgić and Bašić (2021).

following:

- Propagation corrections (C_p): the passage of a pulse through the atmosphere reduces its speed.
 - Dry tropospheric correction ΔR_{dry}
 - Wet tropospheric correction ΔR_{wet}
 - Ionospheric correction Δ_{ion}
- Geophysical corrections (C_g): they are due to vertical movements of the terrestrial surface.
 - Tidal load correction ΔR_{tides}
 - Atmospheric load correction ΔR_{atm}
 - Earth tide correction (Fernandes et al., 2014)
 - Polar tide correction (Fernandes et al., 2014)

The mean sea surface is calculated as:

$$H_{mss} = H_{sat} - R + \sum C_p + \sum C_g \quad (3.9)$$

where

H_{mss} = Mean sea surface height

H_{sat} = Satellite height (relative to the reference ellipsoid)

$\sum C_p$ = Sum of the propagation corrections

$\sum C_g$ = Sum of the geophysical corrections

In addition, if the height of the geoid (N) is known, it is possible to calculate the mean dynamic topography⁶ (MDT) as follows:

$$T_d = H_{mss} - N \quad (3.10)$$

where T_d is the height of the mean dynamic topography.

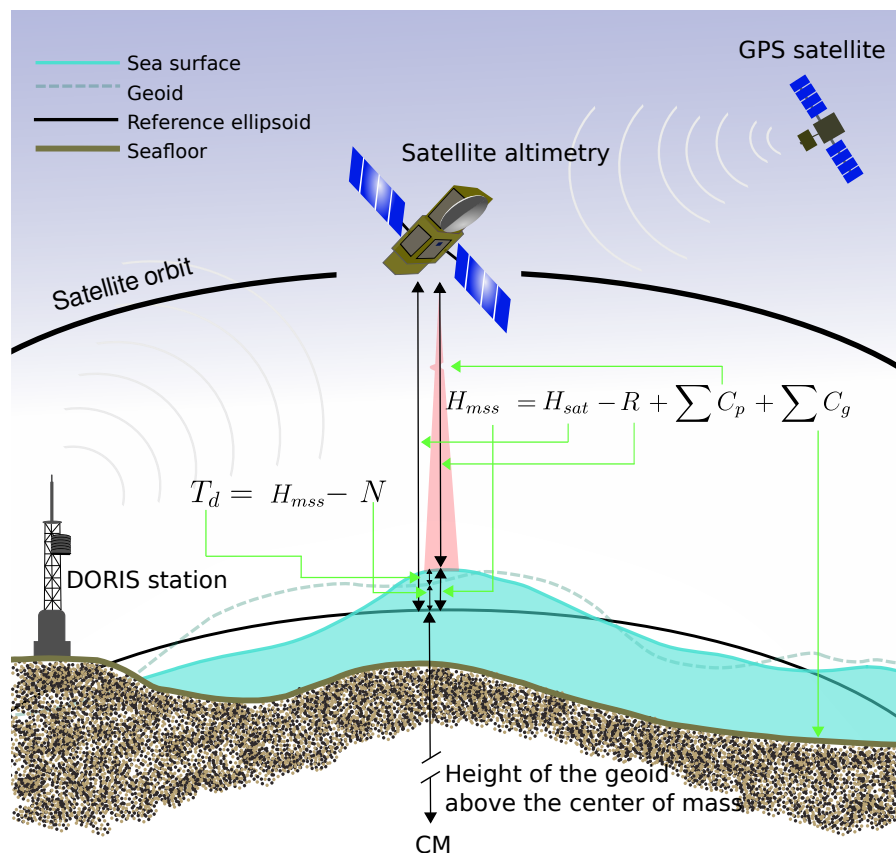


Figure 3.11. Basic principle of altimetric measurements of the mean sea surface. CM: center of mass. Adapted from Shum et al. (1995).

⁶The first satellite to achieve more precise measurements of mean dynamic topography was Seasat (1978). The recording lasted only 100 days.

DATA ANALYSIS

CHAPTER 4

4.1 Signal components

To detect and extract the tectonic signal (e.g., SSE, coseismic displacement) from ocean-bottom pressure or sea level data, we have to reduce our observations for all possible nontectonic factors, including astronomical tides, effects of ocean currents, and ENSO. With this information, Equation 4.1 can represent the factors affecting ocean-bottom pressure measurements.

$$P_{ob}(t) = P_{mob}(t) + AT(t) + S_c(t) + D_{sf}(t) + NT(t) + I(t) \quad (4.1)$$

where

$P_{ob}(t)$ = Ocean-bottom pressure as a function of time t

$P_{mob}(t)$ = Mean ocean-bottom pressure (considered constant during the project)

$AT(t)$ = Astronomical tide

$S_c(t)$ = Seasonal component

$D_{sf}(t)$ = Vertical displacement of the seafloor

$NT(t)$ = Nontidal components (ocean currents, storm surges, tsunamis, etc)

$I(t)$ = Instrumental drift

Furthermore, the sea level equation contains factors similar to the ocean-bottom pressure equation:

$$SL(t) = SL_m(t) + IB(t) + AT(t) + S_c(t) + D_{cc} + NT(t) + I(t) \quad (4.2)$$

where

$SL(t)$ = Sea level as a function of time t

$SL_m(t)$ = Mean sea level (considered constant during the project)

$D_{cc}(t)$ = Vertical displacement of the continental crust

$IB(t)$ = Inverted barometer effect

4.2 Data reduction

Information received from instruments, whether temporary or permanent, likely contains data outside the average (outliers), data gaps, or instrumental drift (Figure 4.1). Hence, before analyzing the data mathematically, it is necessary to visually check and remove erroneous measurements.

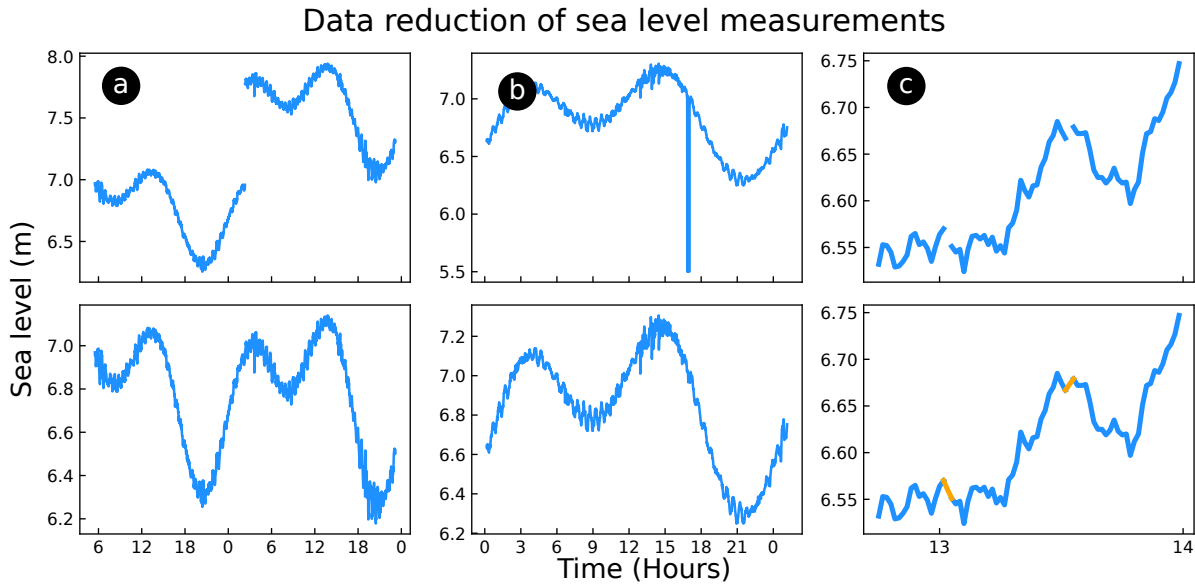


Figure 4.1. Most common practices of sea level data reduction. (a) Interrupted time series are due to replacement of the measurement instrument. (b) Outliers values may be due to errors in the instrument mechanism. (c) If gaps are small, missing values can be filled (orange lines) with a simple interpolation. Personal communication with PSMSL (2023) and SEMAR (2023).

On the other hand, when an instrument is just installed or deployed, as is the case with seafloor pressure sensors, it may suffer from nonlinear drift. This condition is characterized by generally exponential variations in the data and usually lasts up to a month from the start of recording. Therefore, to remove these irregular measurements, it is necessary to cut down the first month of the data or apply some type of correction.

In addition, meteorological and oceanographic measurements commonly contain missing data. If the missing data gaps are short, they can be fixed using, for example, polynomial interpolation. Before performing a harmonic analysis, the time series are averaged into hourly values; next, they are referred to at a zero level by subtracting the mean of the data. Finally (if it would be necessary), the lineal trend is corrected by performing a linear regression model¹ using the following equation:

¹In some cases, an exponential term is included to eliminate the nonlinear drift observed in bottom pressure measurements. Alternatively, the nonlinear drift can be removed by excluding the first month of data.

$$y(t) = m x(t) + b \quad (4.3)$$

where

$y(t)$ = Dependent variable

m = Slope

$x(t)$ = Independent variable

b = Intersection with the y-axis

4.3 Tidal component correction: harmonic analysis

According to the tidal equilibrium theory, sea level depends on the gravitational contribution of the celestial bodies; as these movements are periodic, they can be represented using harmonic constituents of known frequency (see Appendix F). Meanwhile, the amplitude and phase (referred to the Greenwich meridian) are unknown. Therefore, it is possible to obtain these parameters by applying harmonic analysis and then modeling the astronomical tide (Emery and Aubrey, 1991) using Equation 4.4. We then subtract the astronomical tide (AT) from the raw sea level data.

$$AT(t) = SL_m + \sum_{q=1}^{N_h} [A_q \cos(2\pi f_q t) + B_q \sin(2\pi f_q t)] \quad (4.4)$$

the above equation can be expressed in compact form as follows:

$$AT(t) = SL_m + \sum_{q=1}^{N_h} C_q \cos(2\pi f_q t - \phi_q) \quad (4.5)$$

where

q = q th constituent $f_q = q / (N_x \Delta t)$, harmonic constituent frequency expressed in degrees/hour

N_x = Number of measurements

Δt = Sampling rate

N_h = Number of harmonic terms

ϕ_q = Phase lag

A_q, B_q = Constituent coefficients

$C_q = \sqrt{A_q^2 + B_q^2}$

4.4 Nontidal component corrections

4.4.1 Data filtering

Digital filters are mathematical functions that can remove a specific range of frequencies in a sampled signal, which is considered random noise for our purposes. Consequently, the signal of interest can be observed. A filter classification criterion is based on the frequencies that it allows to pass. A high-pass (low-pass) filter allows high (low) frequencies to pass through while attenuating low (high) frequencies. In contrast, a band-pass filter allows only a specific range of frequencies to pass, whereas a band-stop filter attenuates frequencies within a specified range, allowing only the remaining frequencies to pass. The cut-off frequency determines the boundary between the high and low-frequency signals in the filter design (Figure 4.2).

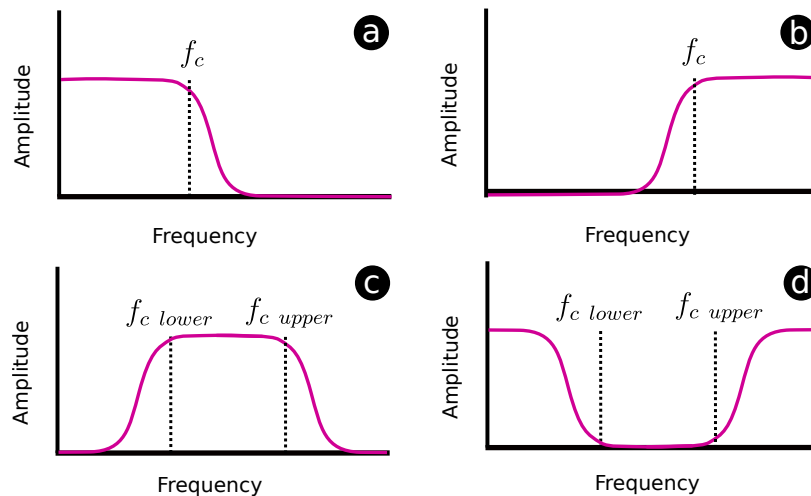


Figure 4.2. Transfer functions. (a) Low-pass, (b) high-pass, (c) band-pass and (d) stop-band filters.

Filter designs are widely used in oceanography and meteorology to analyze temperature, ocean-bottom pressure, atmospheric pressure, sea level, and ocean currents. For this study, we used a low-pass Butterworth filter, which is one of the most widely applied filters in oceanographic data analysis. Its response frequency is known to be “maximally flat”; that is, it does not have ripples in the pass band. However, the transition (roll-off) between the band and stop-band is very broad, but it can be reduced by increasing the Butterworth filter order.

4.4.2 LOWESS smoothing

LOWESS (Locally Weighted Scatterplot Smoothing) is a nonparametric regression technique for fitting a smooth curve into a scatter plot. That means that the fit is not parameterized.

That is, the line is not governed by an equation such as linear (see equation 4.3) or nonlinear regression models, thus it only fits segments of data. To apply the LOWESS smoothing, we must choose the smoothing parameter f_L , a value between $(d_L + 1)/n_L$ and 1, which is equal to the time series fraction chosen. The larger the f_L parameter, the smoother the fitting curve. n_L is the number of data, while d_L is the degree of the local polynomial, and generally, it is the first (locally linear) or second (locally quadratic) order. Tricube weight function W (Equation 4.6) is commonly used in the smoothing procedure.

$$W(u) = \begin{cases} (1 - u^3)^3 & \text{for } 0 \leq u < 1 \\ 0 & \text{for } u \geq 1 \end{cases} \quad (4.6)$$

4.4.3 Simple moving average

It is one of the simplest low-pass filters, and it involves selecting an odd data window to average it and placing it in the middle position of the chosen window. The average is calculated by passing through the observation window in each unit of time, where the first value of the observations is excluded, and the next value in the window is integrated. For this calculation, the half-width $m = (k - 1)/2$ is defined as the number of points to be taken on both sides of the central position of the observations. Thus, the moving average formula defined for odd observations is:

$$T_t = \frac{1}{k} \sum_{j=-m}^m Y_{t+j} \quad (4.7)$$

where

T_t = Filtered value

k = Number of observations

m = Is the half-width

Y = Value centered on observation data

4.5 Ocean-bottom pressure data analysis

Ocean-bottom pressure observations come from sensors deployed off the Guerrero seismic gap, of which only three sensors could be recovered² (Figure 4.3). The pressure recording time was more than four years, and the measurements were taken every half hour. According to Figure 4.3, the measurements from stations 7 and 6 show a remarkable linear trend. Therefore, we carried out an additional analysis (see Section 4.8) to investigate the possible causes of this drift.

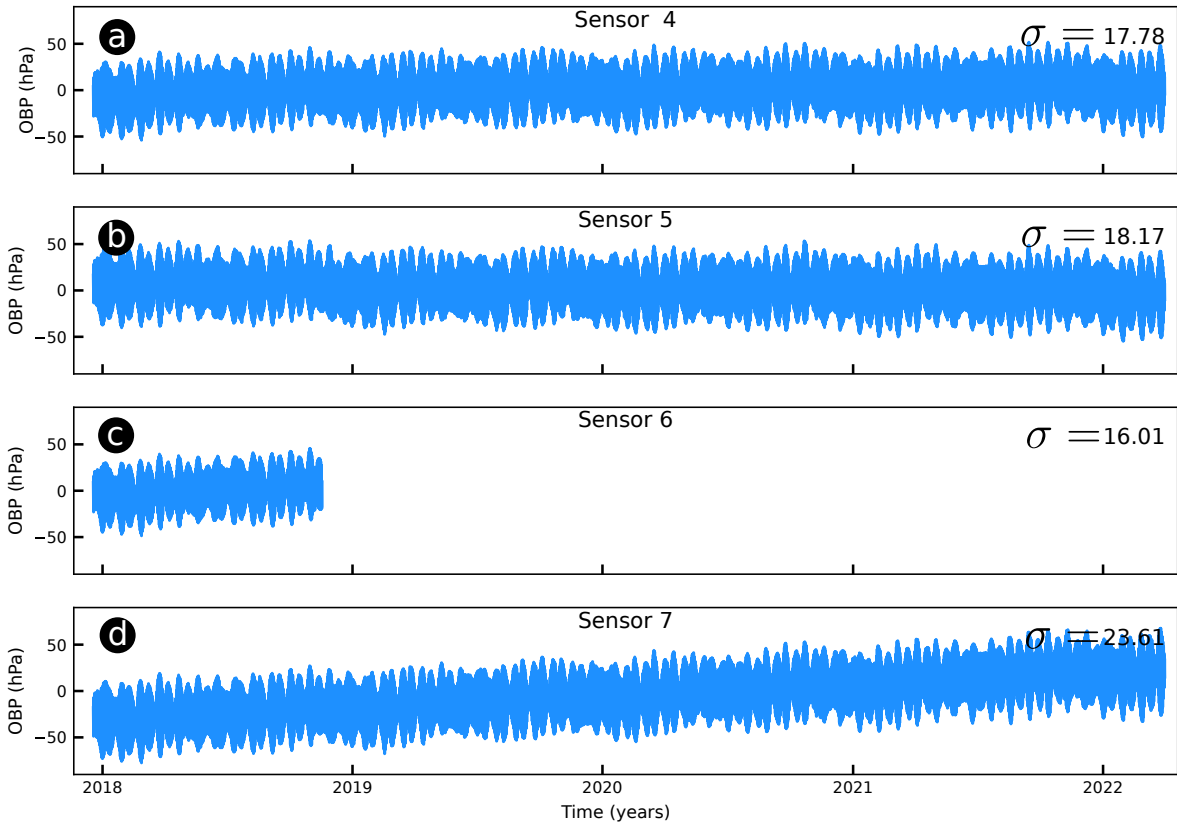


Figure 4.3. Ocean-bottom pressure records from stations (a) 4, (b) 5, (c) 6, and (d) 7. Pressure measurements were taken every half hour. The standard deviation in the upper right corner indicates the variability of the data.

We also recorded ocean-bottom temperature (OBT) measurements at stations 4 and 5. At station 7, the temperature measurements were erroneous (Figure 4.4). A correlation analysis between pressure and temperature allows us to find possible temperature-dependent fluctuations (Itoh et al., 2019). It is also possible to note that OBT-5 measurements are noisier than those of OBT-4 (Figure 4.4). This may have been caused by sensor 5 being at a lower depth where oceanographic variations can be more pronounced than at great depths.

²Additionally, we received 11 months of bottom pressure observations from sensor 6.

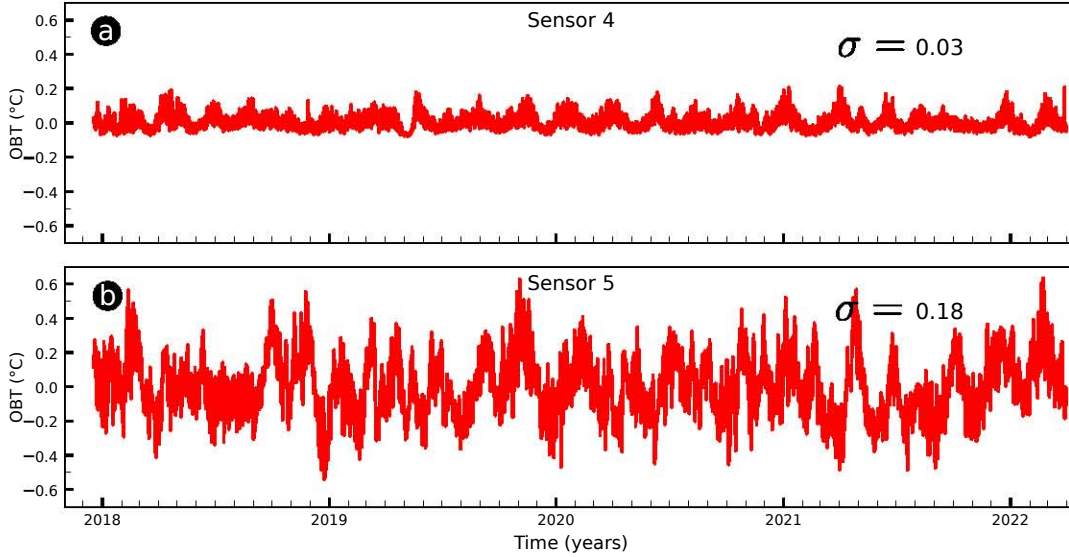


Figure 4.4. Ocean-bottom temperature records from stations (a) 4 and (b) 5. Temperature measurements were taken every half hour

The first month of the pressure and temperature data was excluded, because initial measurements under such conditions often exhibit nonlinear variability (Polster et al., 2009; Inoue et al., 2021). Subsequently, the measurements were resampled from half-hourly to 1-hourly data and referenced to zero by subtracting the mean of the time series. A linear fit³ was then applied and subtracted from the data to correct for sensor drift (Table 4.1).

Table 4.1. Linear trend and intersection of linear fitting model of the OBP data.

Station	Linear trend (m)	Intersection (b)
Sensor 4	1.97 (hPa/yr)	-4.38 (hPa)
Sensor 5	-2.24 (hPa/yr)	5.37 (hPa)
Sensor 6	21.54 (hPa/yr)	-4.82 (hPa)
Sensor 7	12.89 (hPa/yr)	-32.37 (hPa)

The T_Tide program (Pawlowicz et al., 2002) was used to perform harmonic analysis, allowing the calculating of the astronomical tide using 64 harmonic constituents (Figure 4.5). The astronomical tide model was subtracted from each seafloor pressure time series to isolate the residual signal at each site (Figure 4.6).

³The linear trend of a time series is often associated with sensor drift.

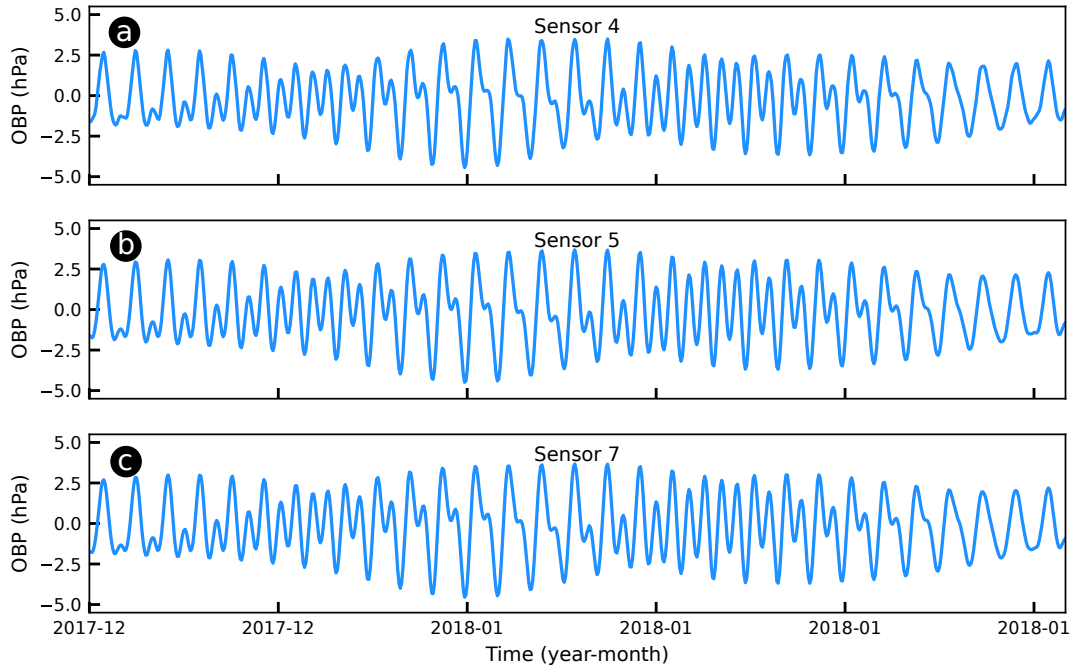


Figure 4.5. Astronomical tide time series calculated from ocean-bottom pressure data collected at sites (a) 4, (b) 5, and (c) 7. The tidal regime is mixed at all three sites.

Finally, we applied a fourth-order low-pass Butterworth filter with a 30-day cutoff period twice to the input signal (once forward, once backward) to eliminate the phase shifting, so there was no delay in the output signal (Figure 4.7). With the previous step, we eliminated signals shorter than 30 days, which would not affect our objective of searching for slow earthquakes that lasted approximately six months.

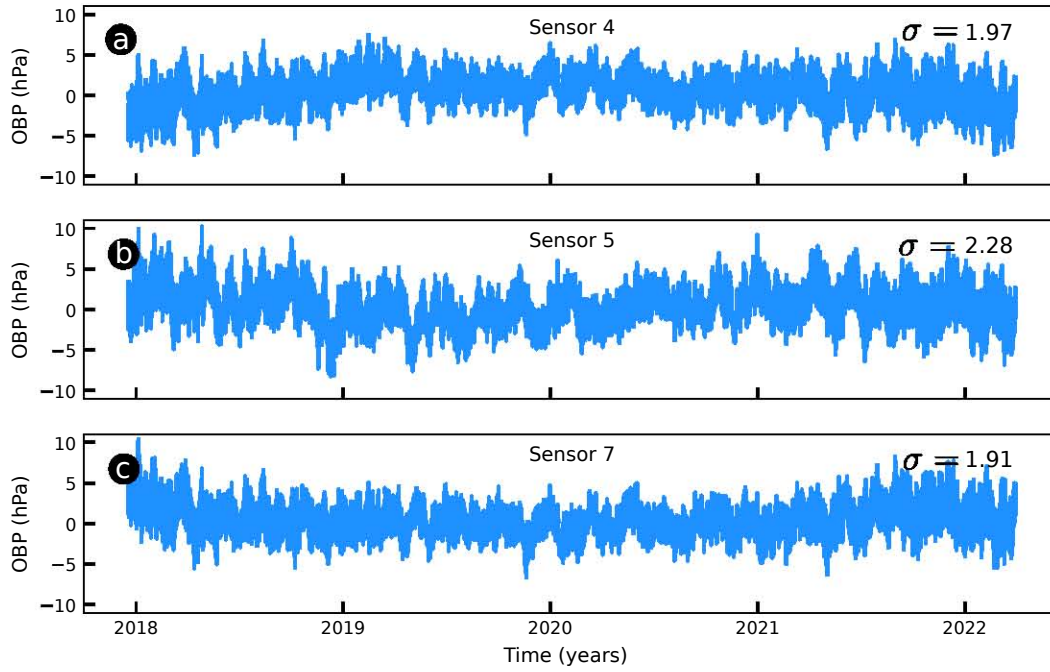


Figure 4.6. Dedided ocean-bottom pressure data from sites (a) 4, (b) 5, and (c) 7.

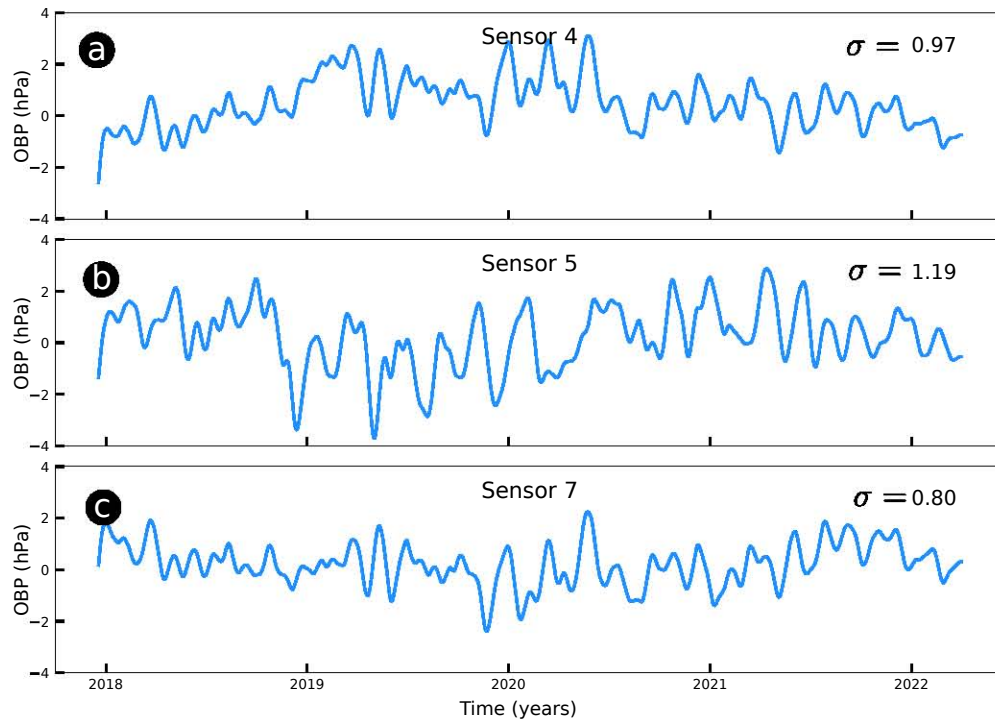


Figure 4.7. Low-pass filtered ocean-bottom pressure measurements from sites (a) 4, (b) 5, and (c) 7.

4.5.1 Correlation analysis with ocean-bottom temperature data

We calculated cross-correlation functions between the ocean-bottom pressure and temperature data (Figure 4.8). According to Gomberg et al. (2019), changes in the pressure gradient are expected to lead to changes in the temperature gradient. Furthermore, Baba et al. (2006) observed a strong correlation between temperature and pressure data with no time lag, so it may be valuable to replicate this analysis with our data and thus correct for temperature-dependent fluctuations.

Figures 4.8a-4.8c show the pressure-temperature plot for each site. Zero lags are observed in some sections.

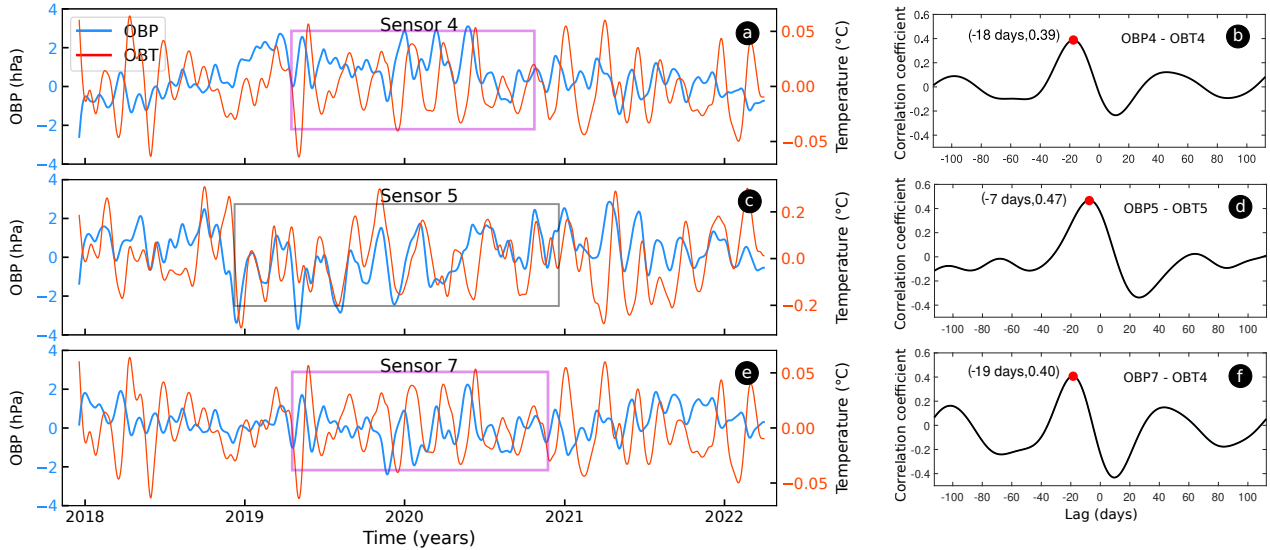


Figure 4.8. Low-pass filtered ocean-bottom pressure and temperature measurements from sites (a) 4, (c) 5, and (e) 7. Gray line box indicates the zero-lag correlation between the fluctuation amplitudes of OBT and OBP. Pink line box indicates that the temperature lags the pressure. Temperature sensor 7 failed. Therefore, the temperature plot of sensor 7 corresponds to the observations of sensor 4. Correlation diagrams correspond to the signals: (b) OBP4-OBT4, (d) OBP5-OBT5, and (f) OBP7-OBT4.

According to Figure 4.8, the similarity between the pressure and temperature variables yielded low values. Therefore, we consider that it is not feasible to apply this correction. Even when taking into account the obtained coefficients and performing the correction, the residual OBP data obtained by the reference-site method (see Section 4.5.3) did not show significant changes compared with the data processed without this correction (see Appendix G).

4.5.2 Correlation analysis with El Niño 3.4 sea surface temperature data

One of the most considerable quasi-periodic contributions to sea level is the effect caused by the El Niño-Southern oscillation (see Section 3.1.4), which Enfield and Allen (1980) studied using sea level records located on the East Pacific coast of the American continent. In this study, a significant correlation was observed between the ENSO period and monthly sea level data. We calculated the cross-correlation between seafloor pressure and sea surface temperature (SST) data for the El Niño 3.4 region. The procedure is summarized below:

1. Weekly SST measurements of El Niño 3.4 region were downloaded from the website <https://www.cpc.ncep.noaa.gov/data/indices/> and, were truncated from December 20, 2016 to March 23, 2022. Subsequently, the sea surface temperature anomalies were derived by subtracting the mean of the time series.
2. Filtered ocean-bottom pressure measurements were resampled from 1-hourly to weekly data to ensure that the sampling coincided with the SST data.
3. Finally, cross-correlation was calculated (Figure 4.9).

The cross-correlation analysis did not produce a favorable result at any site, so this correction was discarded.

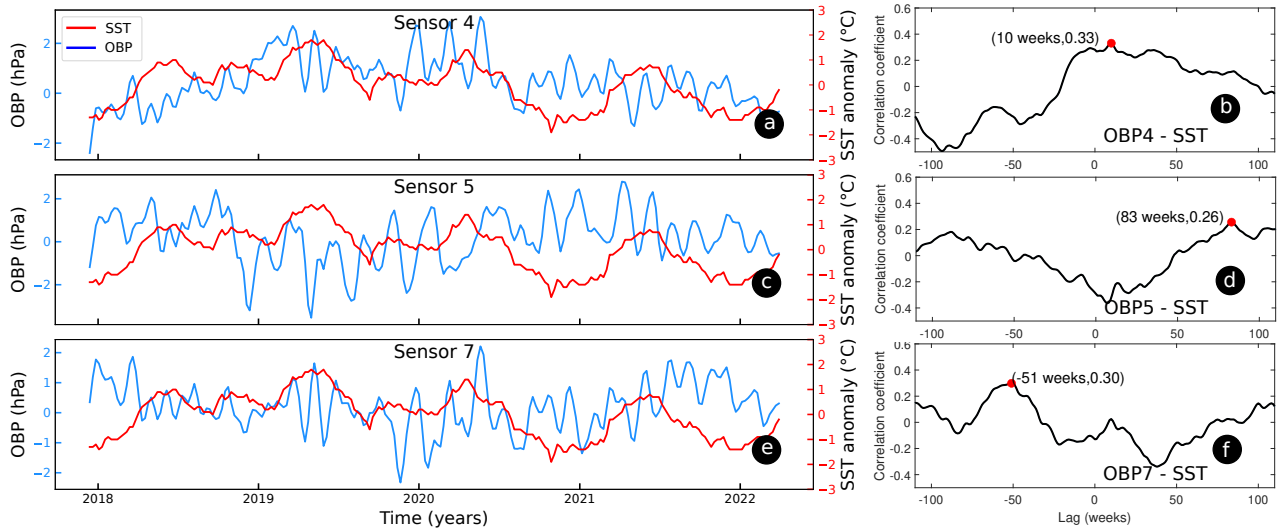


Figure 4.9. Cross-correlation diagrams between sea surface temperature anomalies (El Niño 3.4 region) and ocean bottom-pressure data from sites (a) 4, (c) 5, and (e) 7. (b), (d), and (f) are cross-correlation diagrams.

4.5.3 Methods to identify tectonic deformation signals generated by slow slip events

The reference-site and complex empirical orthogonal function analysis methods were used to identify vertical seafloor deformation signals in residual OBP measurements. In this study, we verify the effectiveness of each technique.

Method 1: Reference site

The reference-site method was the first attempt to search for transient tectonic deformation in subduction zones using ocean-bottom pressure sensors (e.g., Ito et al., 2013; Wallace et al., 2016). This method assumes that an array of instruments on the seabed, placed at a short distance, share the same oceanographic and meteorological noise. In this case, a reference station is used, which is on the subducting cocos plate (station 7), where appreciable tectonic deformation is expected to occur (Figure 1.2). While the remaining stations are on the continental margin off the Guerrero coast (stations 4 and 5), where vertical tectonic deformation may occur.

Therefore, by subtracting the reference station record from a series of ocean-bottom pressures, the expected contributions described by Equation 4.1 or those that could not be eliminated by some other method are eliminated.

Method 2: Complex empirical orthogonal function (CEOF) analysis

Complex empirical orthogonal functions identify orthogonal patterns of variability, in which the first orthogonal component represents the most significant variability, the second component represents the next variability value, and so on (Thomson and Emery, 2014). The CEOF method was initially designed to study weather patterns, and it enabled the discover the El Niño-Southern Oscillation phenomenon. Regarding the application to seafloor pressure data, Watts et al. (2021) used it to study possible slow event signals in the Cascadia subduction zone off the Oregon coast.

There are two ways to calculate complex empirical orthogonal functions: by making (1) the covariance matrix and the (2) singular value decomposition. For this research, we selected the first one. Then the CEOFs are the eigenvectors of the covariance matrix of the data (ocean-bottom pressure series). Next, the pseudocode is shown for calculating the covariance matrix (Björnsson and Venegas, 1997):

1. The matrix M is formed by the 30-day filtered OBP measurements arranged in columns:

$$M = \begin{bmatrix} P_4(1, 1) & P_5(1, 2) & P_7(1, 3) \\ P_4(2, 1) & P_5(2, 2) & P_7(2, 3) \\ \vdots & \vdots & \vdots \\ P_4(t, 1) & P_5(t, 2) & P_7(t, 3) \end{bmatrix} \quad (4.8)$$

2. The normalization of each time series (column) is also carried out by dividing them by their respective standard deviations.
3. The Hilbert transform was then applied to each column of the matrix to rotate the data 90°, resulting in a matrix \tilde{M} with complex values:

$$\tilde{M} = \begin{bmatrix} P_4(1, 1) + iP_4(1, 1) & P_5(1, 2) + iP_5(1, 2) & P_7(1, 3) + iP_7(1, 3) \\ P_4(2, 1) + iP_4(2, 1) & P_5(2, 2) + iP_5(2, 2) & P_7(2, 3) + iP_7(2, 3) \\ \vdots & \vdots & \vdots \\ P_4(t, j) + iP_4(t, j) & P_5(t, j) + iP_5(t, j) & P_7(t, j) + iP_7(t, j) \end{bmatrix} \quad (4.9)$$

4. The covariance matrix M_{cov} is calculated as:

$$M_{cov} = \tilde{M}^t * \tilde{M} \quad (4.10)$$

where \tilde{M}^t is the transpose of \tilde{M} .

5. The eigenvectors and eigenvalues of the covariance matrix M_{cov} are calculated as follows:

$$[C, K] = eig(M_{cov}) \quad (4.11)$$

where C contains the eigenvectors, and K is matrix whose diagonal corresponds to the eigenvalues.

6. The expansion coefficients are calculated as follows:

$$CEOF(i) = M * C(:, i), \quad 1 \leq j \leq 3 \quad (4.12)$$

The results are still complex column vectors; thus, the absolute value of each EOF is calculated. In the previous step, we calculated the magnitude of the analytical signal (envelope effect) of the Hilbert transform.

7. The explained variance of each complex empirical orthogonal function is calculated as:

$$V = \text{diagonal}(L)/\text{trace}(L), \quad (4.13)$$

where V is a column vector of variances, L is a vector with diagonal values (eigenvalues), and its trace is the sum of the diagonal values.

Figure 4.10 shows the three principal components derived from the CEOF technique. Finally, we subtract (1) CEOF-1 and (2) CEOF-1 plus CEOF-2 from the residual pressure time series 5 and 4.

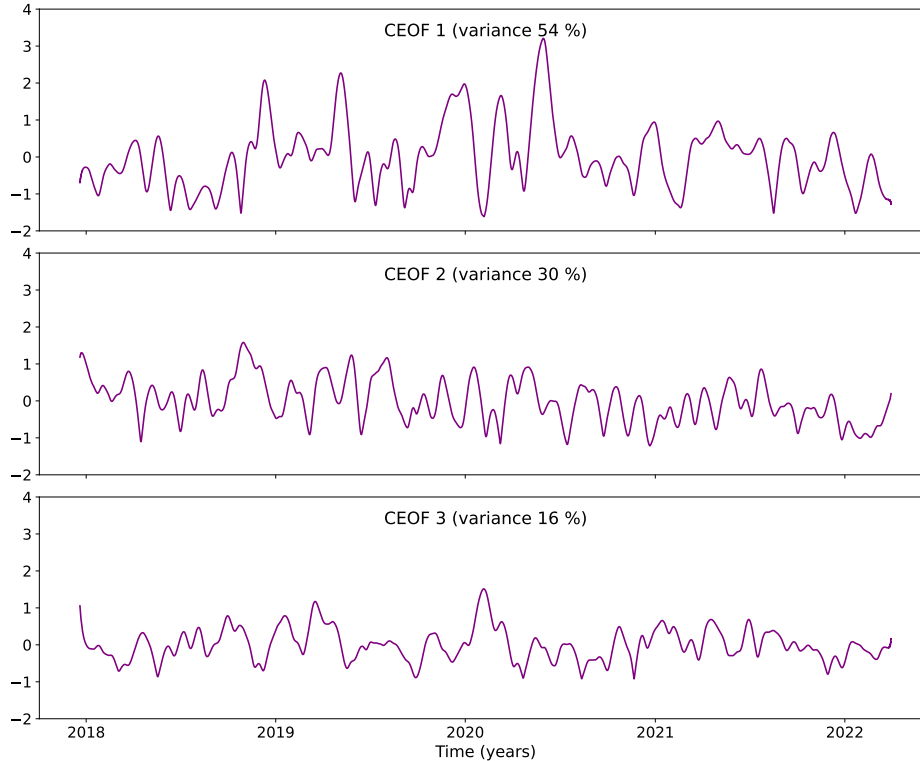


Figure 4.10. Complex empirical functions obtained from the covariance matrix method and their respective variances.

4.6 Ocean-bottom tilt data analysis

Each observation station was integrated with a seafloor tilt sensor. Each sensor recorded tilt observations in degrees in two components: pitch and roll. The specifications are as follows: Range: $\pm 90^\circ$; Accuracy: $\pm 0.01^\circ$; Resolution: 0.01° . The reduction of the tilt data was similar to that of the seafloor pressure data. The steps are as follows:

1. The first 30 days of measurement were eliminated because of the effect of nonlinear drift in the first days of recording (Polster et al., 2009; Inoue et al., 2021).

2. The average value of each time series was then subtracted from the measurements. Then, we modeled a linear fit to remove the sensor drift. Instrumental drift tends to vary and may be caused by differences in installation methods (Tsuji et al., 2023).
3. Slow earthquakes in the Guerrero seismic gap last approximately six months, so we applied smoothing using the moving average technique with a centered window of 61 data points. In this way, fluctuations of less than two months are suppressed.

4.7 Sea level data analysis

4.7.1 Data reduction

Sea level data sampled every minute from 2018 to 2022 at the ports of Acapulco (ACA) and Manzanillo (MZN) were analyzed (Figure 4.11). Initially, the data were averaged to obtain hourly measurements, which were then referenced to the zero level by subtracting the mean. According to the manufacturer, these radar sensors do not suffer instrumental drift. In addition, the coseismic displacement generated by the 2021 Acapulco earthquake (09-08 01:47:46 UTC) was corrected by adding 19.0706^4 cm to the data segment displaced by the seismic event. Subsequently, this corrected segment was concatenated with the rest of the measurements to form a single sea level time series.

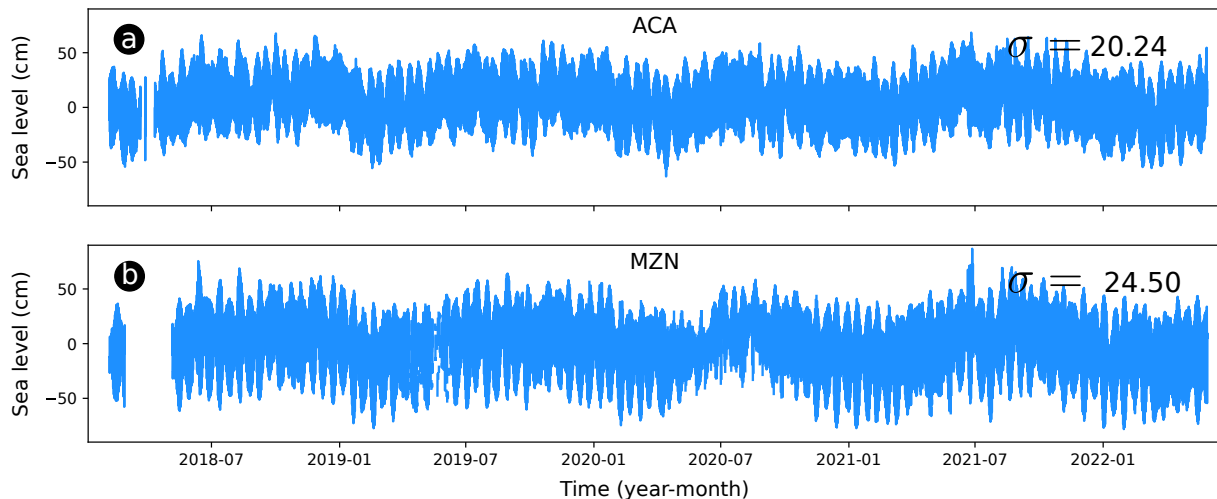


Figure 4.11. Sea level observations from the (a) Acapulco and (b) Manzanillo tide gauge stations. Sea level measurements were taken every minute. The standard deviation in the upper right corner indicates the variability of the data.

⁴This value was obtained from the analysis of the coseismic displacement calculated for the Acapulco station of the Servicio Mareográfico Nacional. See Section 4.10 for more details.

4.7.2 Harmonic analysis

Subsequently, harmonic analysis was performed on the time series from Acapulco and Manzanillo using the T_Tide software. It is easy to notice that the tidal regime is mixed at all three sites (Figure 4.12). Therefore, the residual sea level was calculated by subtracting the astronomical tide from the observed data (Figure 4.13).

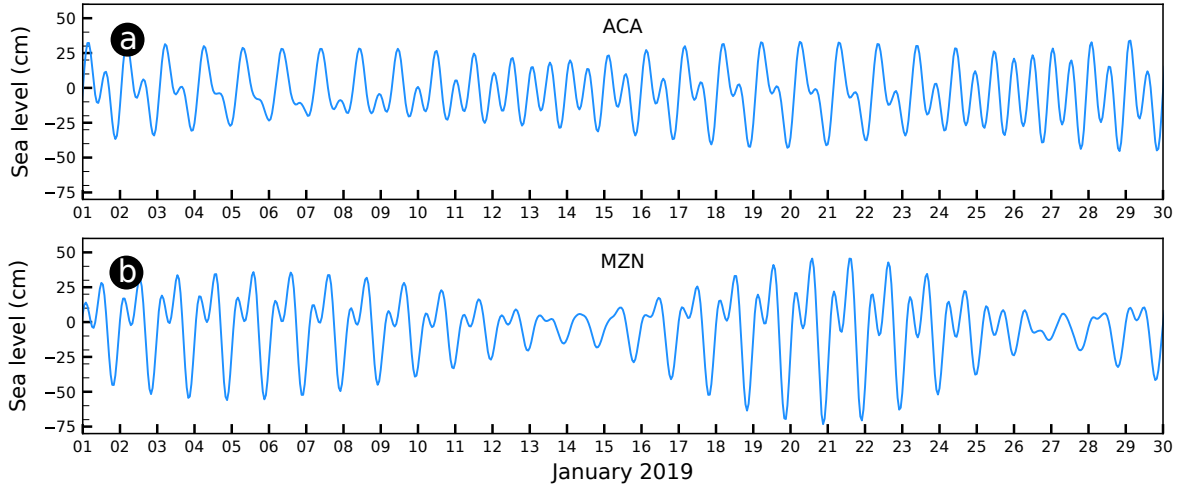


Figure 4.12. Astronomical tide time series calculated from sea level data collected at the (a) Acapulco and (b) Manzanillo tide gauges. It is evident from the tidal predictions that mixed tides prevail at the both Acapulco and Manzanillo ports.

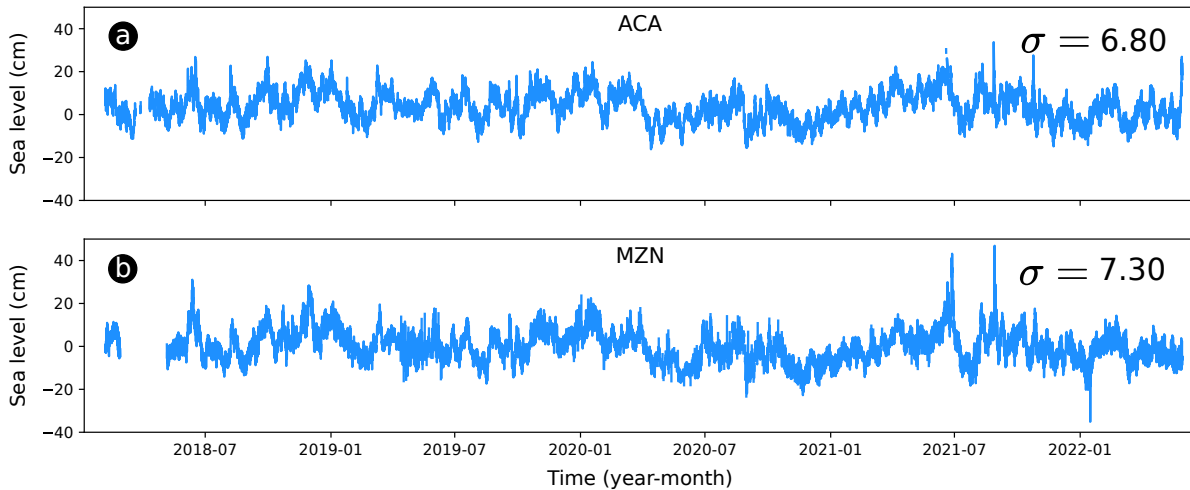


Figure 4.13. Detided sea level time series from (a) Acapulco and (b) Manzanillo. Both series show a linear correlation of 0.81, considering the distance between the tide gauge stations (530 km).

4.7.3 Low-pass filtering

As with the OBP data, a fourth-order Butterworth filter with a cut-off frequency of 30 days was applied to the sea level measurements (Figure 4.14).

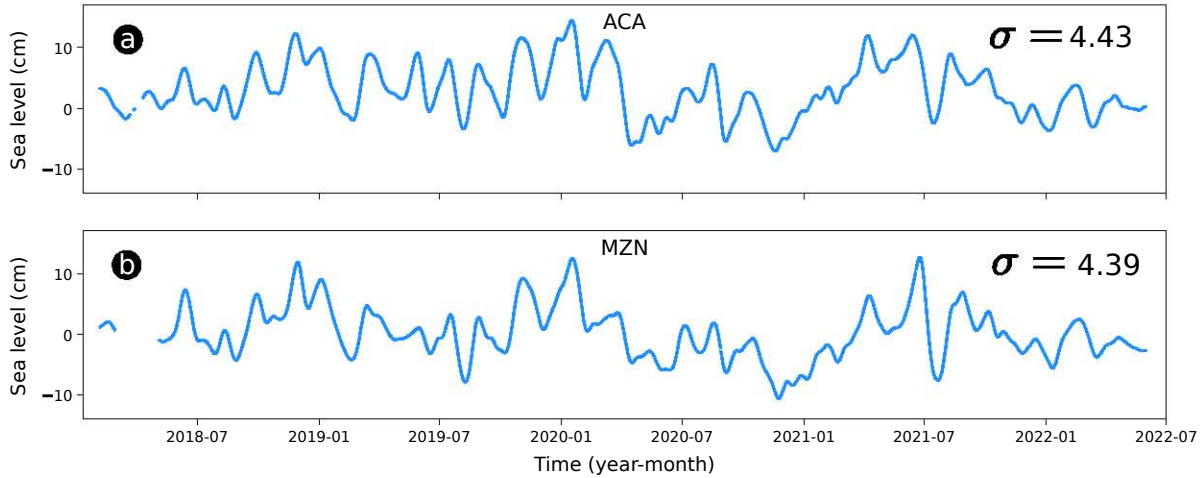


Figure 4.14. 30-day low-pass filtered sea level measurements from (a) Acapulco and (b) Manzanillo ports. The filtering revealed 2-month oscillations. These shorter-period signals are probably caused by local atmospheric forcing, driven by wind and pressure.

4.7.4 Correlation analysis with atmospheric pressure and temperature data

Reducing the sea level signal may require additional steps beyond removing the tidal signal, i.e., identifying whether environmental factors such as atmospheric pressure and temperature affect sea level observations. To evaluate the two contributions from temperature and pressure, we performed a cross-correlation analysis (Figure 4.15). Thus, we can evaluate whether it is feasible to perform these corrections. However, it must be considered that other factors, such as changes in wind direction and pressure gradient, coastal-trapped waves, and local seiches, induce noise in the signals, hindering correlations.

No correction were made for temperature and atmospheric pressure due to the low correlation values (Figure 4.15).

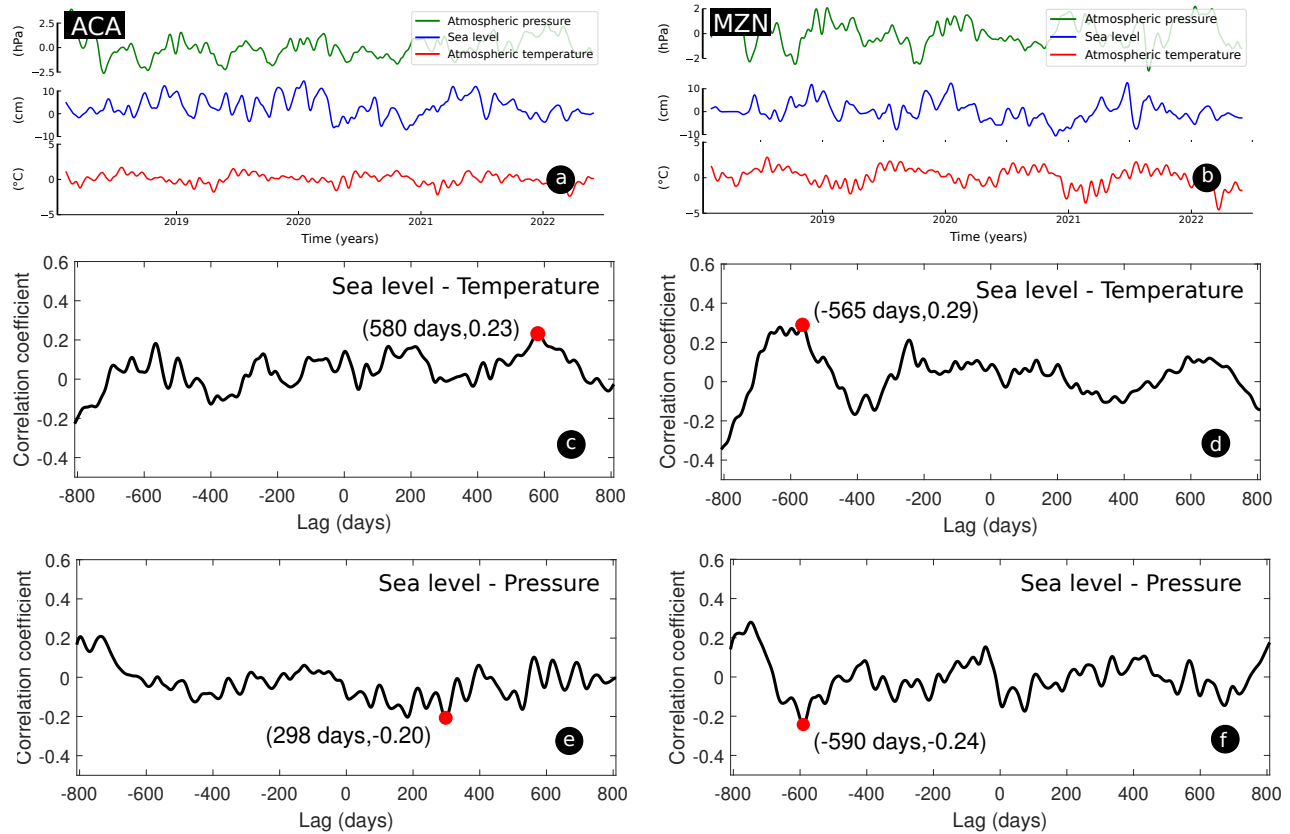


Figure 4.15. Sea level time series and atmospheric temperature and pressure observations from (a) Acapulco and (b) Manzanillo. (c) and (e) show the correlation diagrams of the Acapulco data, and (d) and (f) show the correlation diagrams of the Manzanillo data.

4.7.5 Correlation analysis with El Niño 3.4 sea surface temperature data

We performed a cross-correlation analysis to determine whether there was a correlation between sea surface temperature and sea level observations (Figure 4.16) and to remove any possible ENSO-related low-frequency signals. The procedure is as follows:

1. Weekly sea surface temperature observations (El Niño 3.4 region) were downloaded from the website <https://www.cpc.ncep.noaa.gov/data/indices/> and truncated from January 31, 2018 to May 25, 2022.
2. Filtered sea level measurements were resampled from 1-hourly to weekly data to ensure that the sampling coincided with the SST data.
3. Finally, cross-correlation analysis calculation was performed (Figure 4.16).

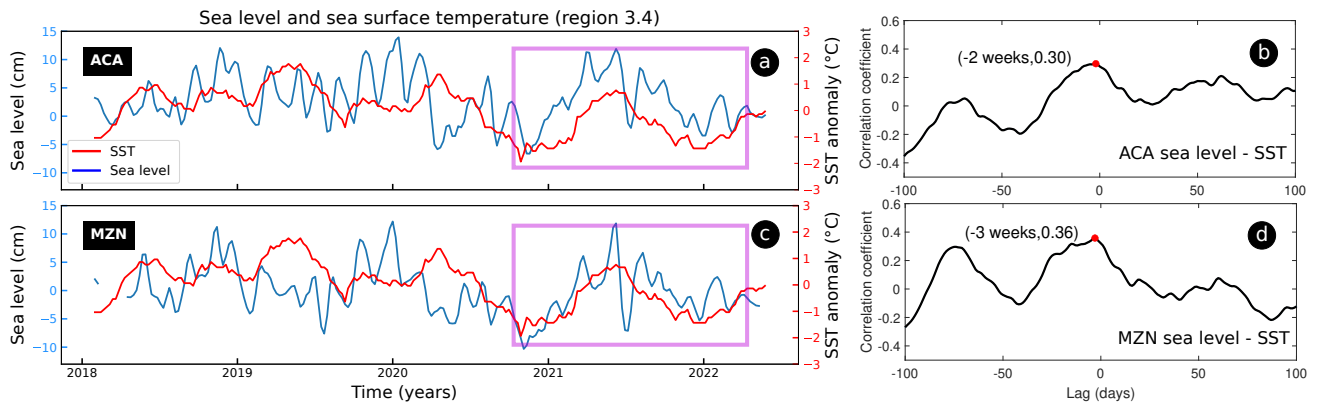


Figure 4.16. (a) Acapulco and (c) Manzanillo sea level time series and the SST anomaly (El Niño 3.4 region). In the pink line box, there is an evident correlation between sea level and surface temperature anomalies, while they do not match up over time in the rest of the time series. (b) and (d) show the correlation diagrams for Acapulco and Manzanillo, respectively.

4.7.6 Reference-site method

To conduct the reference-site method, the Manzanillo station was established as the reference site (Figure 1.2) because it is located on a tectonically different zone from Acapulco. Subsequently, the Acapulco sea level data were subtracted from the Manzanillo sea level data.

4.8 Long-term trend in pressure sensor 7

The linear trends of the pressure records from stations 6 and 7 are 21.54 hPa/yr and 12.89 hPa/yr, respectively, which are greater than the other trends from the linear fitting model, as shown in Table 4.1. We examined whether the observed linear trend in sensor 7 was caused by sensor drift or Cocos plate tectonics.

The procedure is as follows: First, we generate a bathymetric profile oriented parallel to the motion vector (30° clockwise from north) of the Cocos plate, which, in turn, passes through the location of station 7 (Figure 4.17). The bathymetric profile was obtained using GeoMapApp software based on the GEBCO 2024 Gridded Bathymetry Data (Ryan et al., 2009).

We then selected a section of the bathymetric profile where bending of the incoming Cocos plate off the Middle Mesoamerican trench (MAT) was evident. Next, we performed a polynomial fit of different degrees ($n = 3, 4,$ and 5) using data from the bathymetric segment. Finally, we calculate the derivative of each polynomial fit and convert them to degrees (Figure 4.17).

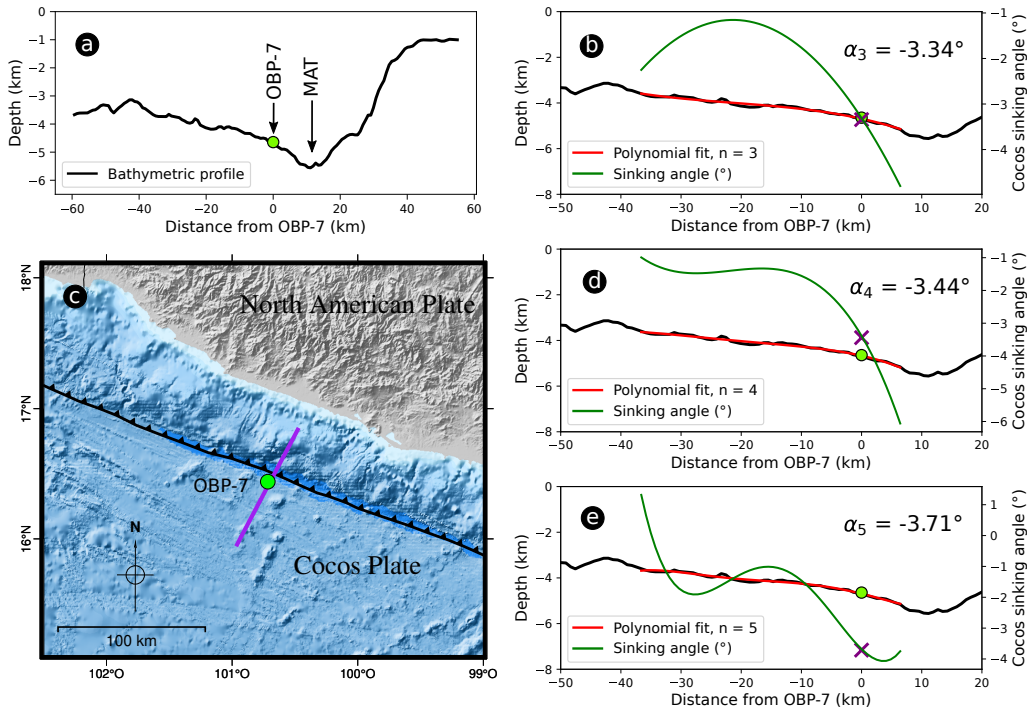


Figure 4.17. (a) Bathymetric profile parallel to the motion vector of the Cocos plate. (c) Location map of the bathymetric profile. Purple line indicates the bathymetry profile. Red line represents the polynomial fit of the bathymetric segment with degrees $n = 3$ (b), 4 (d), and 5 (e). The α angle of bathymetric tilt is calculated at the point where the derivative curve (green line) intersects the x-axis at $x = 0$ (location of OBP-7 on the profile). MAT: Middle American Trench.

To calculate the bathymetric tilt angle (α) of the Cocos plate at the measurement site, we identified the intersection of the derivative curve with the $x = 0$ axis (indicates the position of the OBP station) for each plot.

We modeled the annual sinking rate (H_{sr}) of the Cocos plate at site 7 (Figure 4.18). The sinking rate is equivalent to the effect of the Cocos plate’s motion in the NNR (no-net-rotation) reference system on the linear sensor drift of the ocean bottom pressure data at site 7.

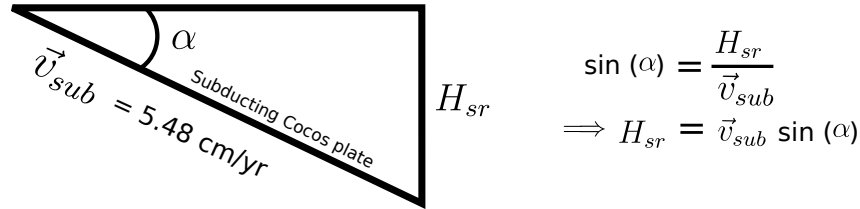


Figure 4.18. Model of the incoming Cocos plate sinking rate at station 7. The Cocos plate’s motion (\vec{v}_{sub}) was obtained from the online tectonic plate motion calculator (<https://www.unavco.org>) using the MORVEL 2010 model (DeMets et al., 2010) fixed to the NNR (no-net-rotation) frame.

Using the formula in Figure 4.18, we calculated the subsidence rate from the tilt angles at site 7 (Table 4.2). This subsidence rate, expressed in cm/yr, is equivalent to hPa/yr because a 1-cm water height corresponds to 1 hPa. Therefore, we can state that this increase in pressure (increase in the water column) linearly affects the seafloor pressure measurements.

Table 4.2. Contribution to the linear pressure data trend due to Cocos plate motion.

	α ($^{\circ}$)	H_{sr} (cm/yr)	Contribution ¹ (%)
Model n = 3	-3.34	-0.32	2.48
Model n = 4	-3.44	-0.33	2.56
Model n = 5	-3.71	-0.35	2.72

¹ It is calculated by a rule of three, where 12.89 hPa/yr corresponds to 100 %.

4.9 Evaluation of variance reduction and coherence between pairs of nontidal ocean-bottom pressure signals.

Each stage of data reduction reduces the variability of the measurements, as this guarantees a decrease in ocean noise, making the tectonic signal distinguishable. Therefore, the standard deviation was used to quantify the reduction in variability (Equation 4.14).

Our approach involves using the Pearson correlation formula (Equation 4.15) to calculate the similarity between nontidal ocean-bottom pressure signals. This method allows us to evaluate the relative depth dependence between measurement sites (Equation 4.15). A 717-day data window (Aug-02-2019 to Jul-19-2021) was used to calculate the correlation. This data range was chosen because in that period, the pressure measurements (stations 4 and 5) are expected to be unaffected by any vertical tectonic deformation associated with slow events.

$$\sigma = \sqrt{\frac{1}{N_x - 1} \sum_{i=1}^{N_x} (x(t) - \overline{x(t)})^2} \quad (4.14)$$

$$C_{pc} = \frac{\sum_{i=1}^N (x_1(t) - \overline{x_1(t)})(x_2(t) - \overline{x_2(t)})}{\sqrt{\sum_{i=1}^N (x_1(t) - \overline{x_1(t)})^2} \sqrt{\sum_{i=1}^N (x_2(t) - \overline{x_2(t)})^2}} \quad (4.15)$$

where

σ = Standar deviation

N_x = Number of measurements

$x(t)$ = Measurements

$\overline{x(t)}$ = Average of the measurements

C_{pc} = Pearson correlation coefficient

4.10 Analysis of the coseismic displacement of the 2021 Acapulco earthquake recorded in sea level measurements

The 2021 M_W 7.1 Acapulco earthquake (01:47:46 UTC) was a reverse faulting event close to the northwest Guerrero seismic gap with an epicenter off the Guerrero coast (Figure 4.19). The study of this seismic event is relevant, given its magnitude and the fact that researchers consider it a repeat of the 1962 M 7.15⁵ Acapulco earthquake. The similar shape of the seismograms suggests that the two events ruptured the same patch on the plate interface (Iglesias et al., 2022). On the other hand, Ortiz et al. (2000) calculated the coseismic displacements of the May 11 (M 7.1) and May 19, 1962 (M 7.0) seismic doublets recorded in sea level data, resulting in coastal uplifts of 15 ± 3 cm and 7 ± 3 cm, respectively.

The coseismic signal recorded in sea level observations is estimated generally using a data window of 12 to 24 h before and after an earthquake. In this study, to estimate the displacement caused by the 2021 Acapulco earthquake in the tide gauge stations located in the port of Acapulco, we used 24 hours (two low tides and high tides) of sea level measurements for the pre-tsunami and post-tsunami signals. Next, we calculated the average of the two segments (pre- and post-tsunami) and their standard deviations. The coseismic displacement was obtained by subtracting the pre-tsunami signal from the post-tsunami signal.

⁵Magnitude M 7.1 was calculated using the formula $M = (2/3) \log M_o - 10.67$ (Ortiz et al., 2000).

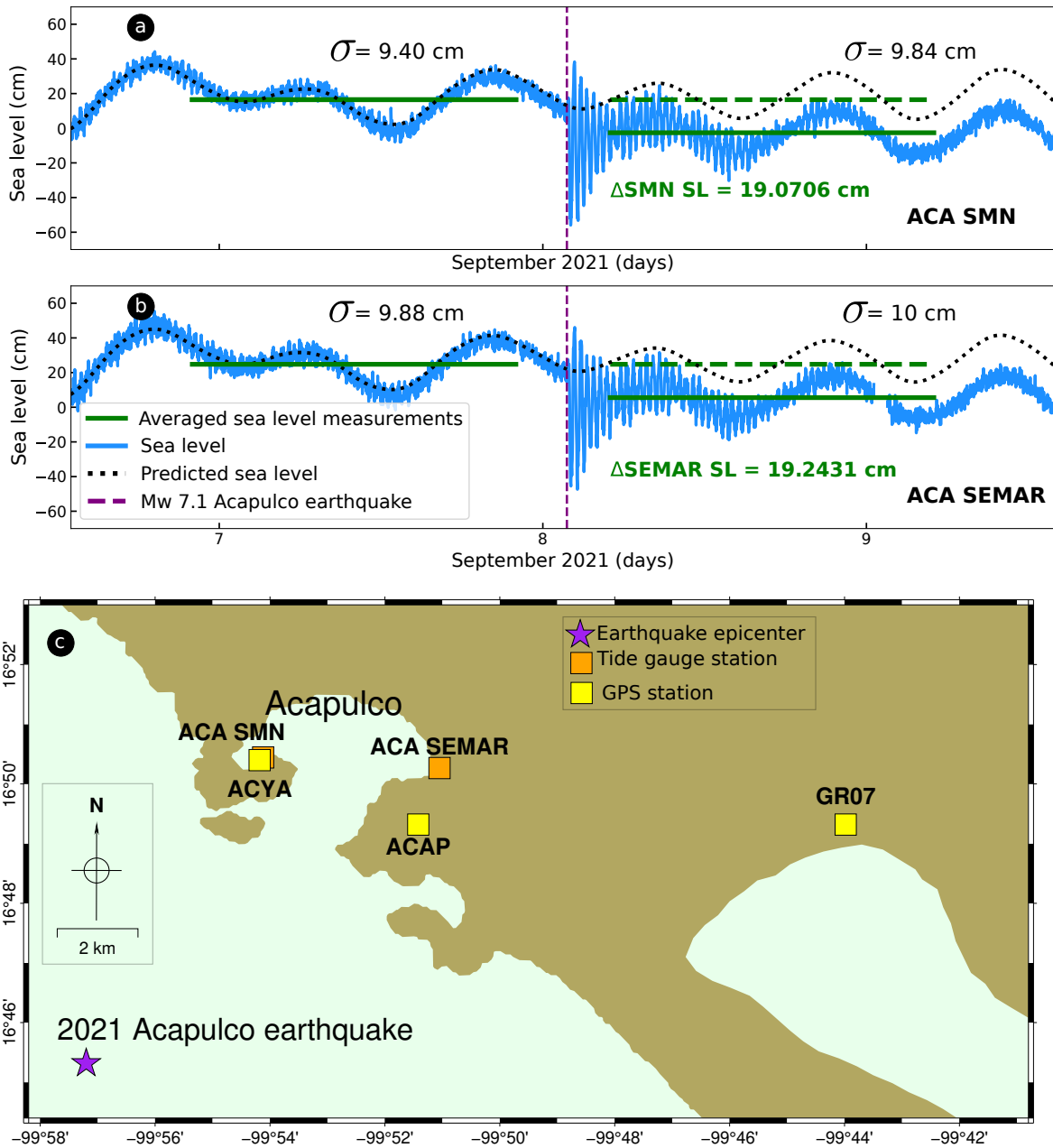


Figure 4.19. Coseismic displacement of the 2021 Acapulco earthquake recorded by two tide gauges in Acapulco Bay. (a) Sea level data from the Servicio Mareográfico Nacional; (b) Sea level data from from the Secretaría de Marina; (c) Location map of the tide gauge stations. The distance between stations is 6.4 km. The subsidence in both sea level records indicates an uplift of the land. Purple dashed line indicates the time origin of the earthquake: 2021-sep-08 01:47:00 UTC (2021-sep-07 20:47:00 local time).

4.11 Analysis of tsunami signals

4.11.1 Main characteristics of tsunami signals

We used sea level time series sampled every minute from Acapulco and Manzanillo tide gauge stations of the Servicio Mareográfico Nacional (SMN) and Secretaría de Marina (SEMAR). From 2017 to 2022, five tsunamis impacted the Mexican Pacific coast. From those three were local events: Chiapas, 2017 (Figure 4.20); Oaxaca, 2018 (Figure 4.21); and Acapulco, 2021 (Figure 4.22); and two tele-tsunamis: New Zealand, 2021 (Figure 4.23) and Tonga, 2022 (Figure 4.24). First, the tidal contribution was removed by performing harmonic analysis. Then, we selected a window of 8,000 measurements (5.55 days) sampled every minute for each event. Next, we performed LOESS smoothing using a 200-sample window ($f_L = 0.025$), and finally, we subtracted the smoothed signal to remove low-frequency oscillations. The residual signal allowed us to clearly observe the recorded tsunami events, making it possible to identify the tsunami arrival time, maximum peak-to-trough height, and maximum amplitude (Table 5.1).

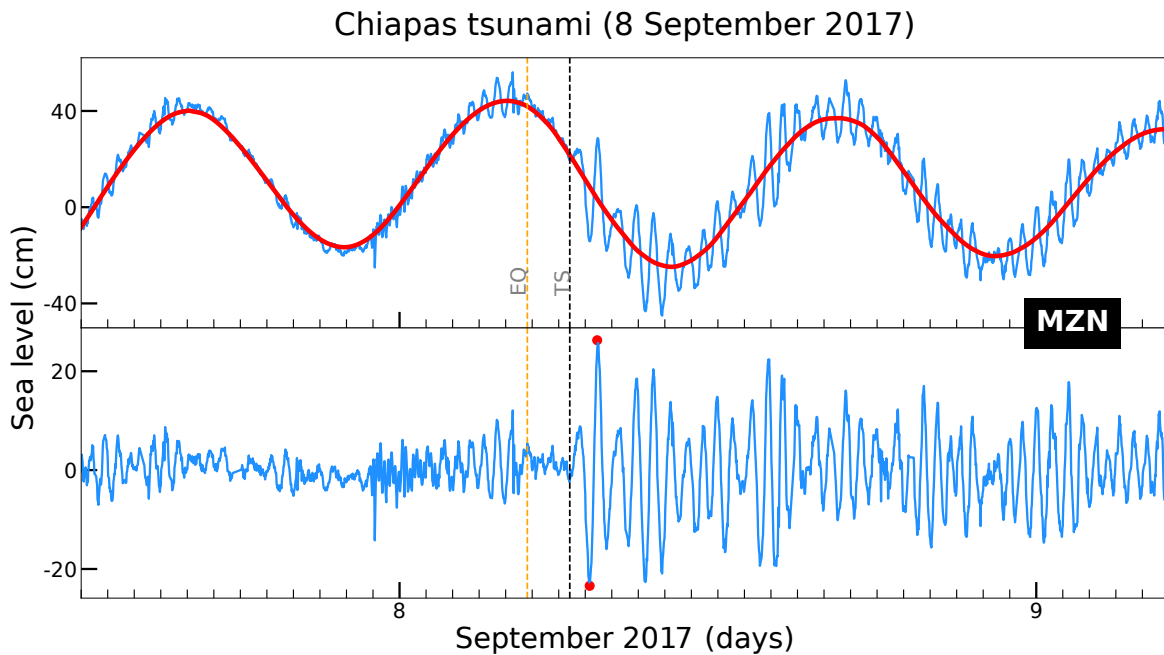


Figure 4.20. Arrival of the 2017 Chiapas tsunami at the Manzanillo tide gauge. (Top) The sea level observations (blue line) were detided and LOESS smoothing was performed (red line). (Bottom) The smoothing was removed, so it was clearer to identify the tsunami arrival time and the maximum peak-to-trough amplitude (red points). EQ: earthquake; TS: tsunami. Orange dashed line represents the origin time of the earthquake, and black dashed line indicates the arrival time of the tsunami wave. UTC time.

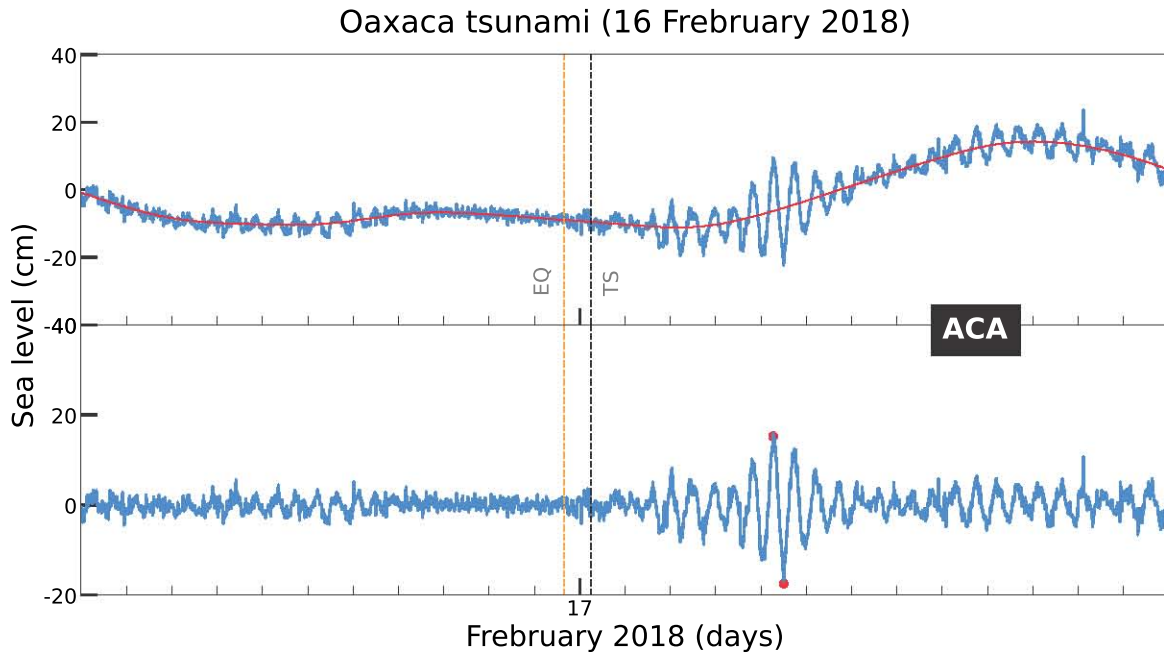


Figure 4.21. Arrival of the 2018 Oaxaca tsunami at the Acapulco tide gauge. (Top) The sea level observations (blue line) were detided, and LOESS smoothing was performed (red line). (Bottom) The smoothing was removed, so it was clearer to identify the tsunami arrival time and the maximum peak-to-trough amplitude (red points). EQ: earthquake; TS: tsunami. Orange dashed line represents the origin time of the earthquake, and black dashed line indicates the arrival time of the tsunami wave. UTC time.

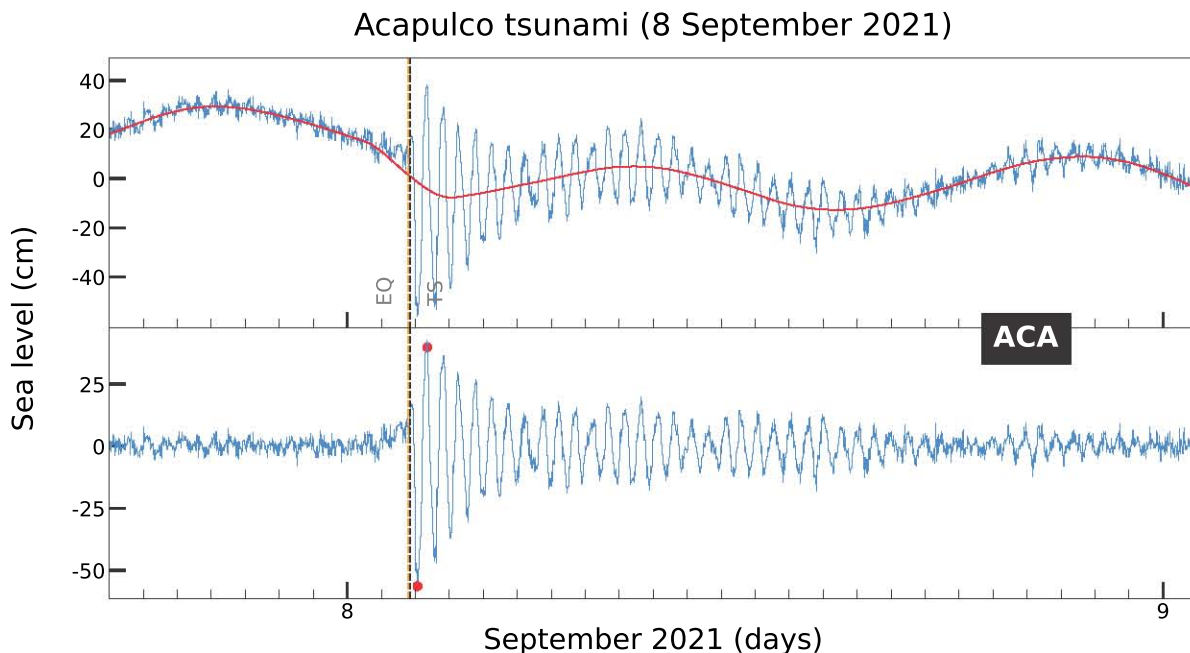


Figure 4.22. Arrival of the 2021 Acapulco tsunami at the Acapulco tide gauge. (Top) The sea level observations (blue line) were detided, and LOESS smoothing was performed (red line). (Bottom) The smoothing was removed, so it was clearer to identify the tsunami arrival time and the maximum peak-to-trough amplitude (red points). EQ: earthquake; TS: tsunami. Orange dashed line represents the origin time of the earthquake, and black dashed line indicates the arrival time of the tsunami wave. UTC time.

New Zealand tsunami (4 March 2021)

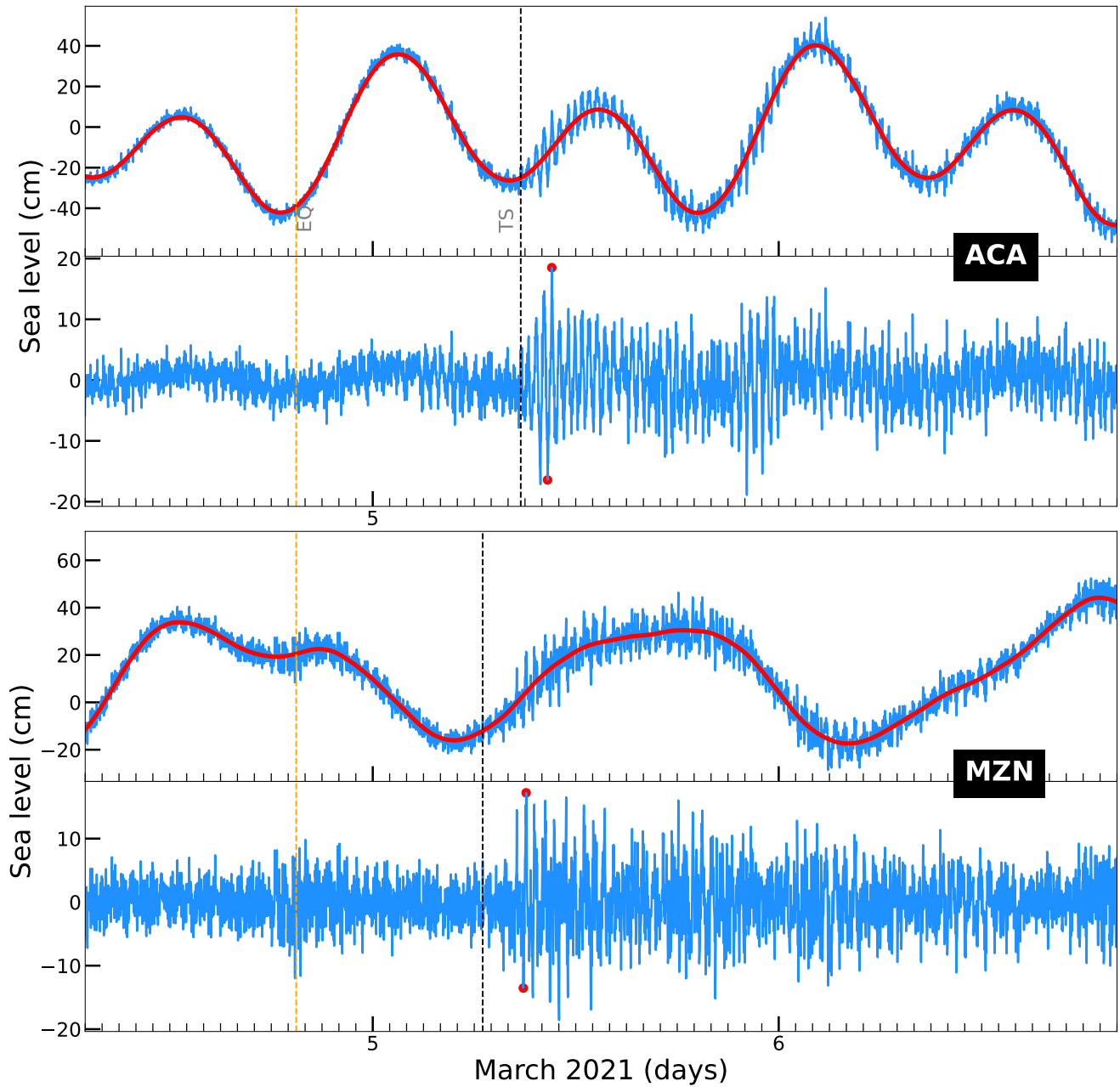


Figure 4.23. Arrival of the 2021 New Zealand tsunami at the Acapulco and Manzanillo tide gauge. (Top of each box) The sea level observations (blue line) were detided, and a LOESS smoothing was performed (red line). (Bottom of each box) The smoothing was removed, so it was clearer to identify the tsunami arrival time and the maximum peak-to-trough amplitude (red points). The Manzanillo sea level data were obtained from the Secretaría de Marina. EQ: earthquake; TS: tsunami. Orange dashed line represents the origin time of the earthquake, and black dashed line indicates the arrival time of the tsunami wave. UTC time.

Tonga tsunami (15 January 2022)

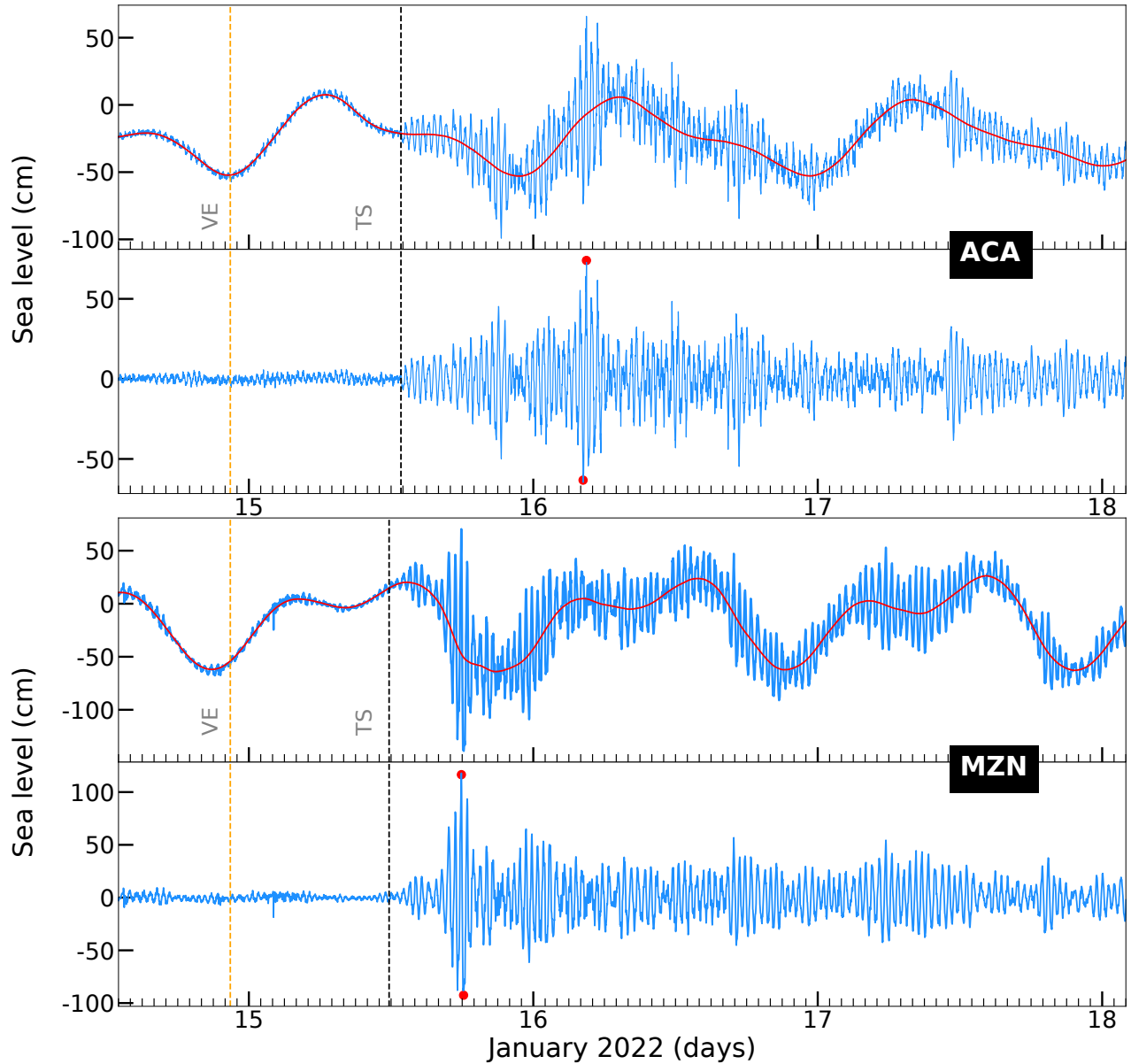


Figure 4.24. Arrival of the 2022 Tonga tsunami at the Acapulco and Manzanillo tide gauges. (Top of each box) The sea level observations (blue line) were detided, and LOESS smoothing was performed (red line). (Bottom of each box) The smoothing was removed, so it was clearer to identify the tsunami arrival time and the maximum peak-to-trough amplitude (red points). VE: volcanic explosion; TS: tsunami. Orange dashed line represents the origin time of the earthquake, and black dashed line indicates the arrival time of the tsunami wave. UTC time.

4.11.2 Amplitude spectrum: characteristic frequencies

It is known that different tsunamis recorded at the same tide gauge station show characteristic frequencies, which are excited due to sea level perturbations. To analyze the detided sea level data, we first replaced missing null values with zero values. In addition, the time series were normalized using the minimum-maximum normalization method. Equation 4.16 shows the procedure followed.

$$x_{nor} = \frac{x - x_{min}}{x_{max} - x_{min}} \quad (4.16)$$

where

x_{nor} = Normalized value

x = Arbitrary value of the time series

x_{min} = Minimum value of the time series

x_{max} = Maximum value of the time series

Then, we used a 1-day data window (1440 samples) starting from the tsunami arrival time. After that, we applied a cosine window (CW) to reduce the leakage effect in the Fourier spectrum (FS), and then we multiplied the CW by the data window of each tsunami. Finally, we obtain the Fourier amplitudes by applying the Fourier transform (FT) to each data segment. After calculating the Fourier amplitude of each tsunami recorded at the same station, the peak frequencies were identified.

4.11.3 Spectral ratios: tsunami source model

The spectral ratio method (SRM) proposed by Rabinovich (1997) is an adaptation for studying tsunami signals that comes from the assumption of using the P and S waves of earthquakes to aim to characterize the site effect. With the SRM, we pretend to know the source function of the tsunamis by dividing the tsunami signal (disturbed sea level) over the background one (sea level before the tsunamigenic event). The sea level measurements not only recorded the tsunami energy but also reflected and refracted signals from islands and seamounts, mixed waves in the harbor, and distorted waves due to continental shelf bathymetry (Heidarzadeh et al., 2022). Therefore, by dividing the two signals, the noise, as mentioned above, is expected to be eliminated. The formula of the observed tsunami spectrum can be represented as:

$$S_{obs}(\omega) = S_{tsu}(\omega) + S_{bg}(\omega) + S_{\epsilon}(\omega), \quad (4.17)$$

where

ω = Angular frequency
 S_{obs} = Observed tsunami spectrum
 S_{tsu} = Tsunami spectrum
 S_{bg} = Background spectrum
 S_{ϵ} = Noise spectrum

We constructed the background and tsunami spectrum of the 2022 Tonga tsunami using a methodology similar to that used by Zaytsev et al. (2017). First, we took a 4.3-day data segment⁶ for the background signal and a 34-hour data segment⁷ for tsunami signal and replaced the null values with zeros. Then, we implemented the Welch algorithm (Welch, 1967), where the data segments are divided into blocks of 512 samples (1-minute), the overlap is 50 %, and a Kaiser-Bessel window is applied to reduce leakage sidelobes. Finally, the Fourier transform was applied to the data, and the Fourier amplitudes were squared to get the power spectral density (PSD). Then, the spectral ratios, $S_{ratio}(\omega)$, were calculated by dividing the tsunami spectrum, $S_{tsu}(\omega)$, over the background spectrum, $S_{bg}(\omega)$ (Equation 4.18).

$$S_{ratio}(\omega) = \frac{S_{tsu}(\omega)}{S_{bg}(\omega)} \quad (4.18)$$

⁶2048 (minutes) \div 1440 (minutes) = 1.42 (days) \sim 34 (hours).

⁷(3 \times 2048 (minutes) \div 1440 (minutes)) = 4.26 (days) \sim 4.3 (days).

RESULTS AND DISCUSSIONS

CHAPTER 5

In this study we used ocean-bottom pressure and sea level data corrected for tidal signals and smoothed using a 30-day low-pass Butterworth filter. The reference-site and CEOF methods were used for the OBP data, whereas the reference-site method was used for the sea level data. In both cases, the objective was to reveal the vertical tectonic deformation associated with slow earthquakes. The relevance of seismogeodetic measurements off the Guerrero gap coast lies in knowing the extent of slow slip events. In addition, signals from five tsunamis were analyzed, given the importance of this seismogeodetic study to seismic risk mitigation in the Guerrero seismic gap and nearby communities.

5.1 Tectonic deformation in seafloor pressure and sea level data

5.1.1 Ocean-bottom pressure

Residual seafloor pressure time series for sites 4 and 5 were obtained using station 7 as the reference pressure, CEOF1, and CEOF1+2. In addition, each station recorded the seafloor tilt (pitch and roll) to which a moving average filter with a centered window of 61 sample points was applied. The three residual pressure time series obtained at each site were compared with their respective residual tilt data and GPS measurements from the CAYA station.

Correlations with bottom temperature and environmental observations

After removing the tidal effects, adjusting for sensor drift, and signal filtering, we conducted a cross-correlation analysis between the ocean-bottom pressure and temperature data. In the case of site 7, the temperature sensor failed; therefore, we used temperature observations from station 4 because the pressure signals from both sites were quite similar (see Section 5.3).

The correlation coefficients (Figure 4.8) for adjusting temperature-related fluctuations in seafloor pressure data were 0.39, 0.47, and 0.40 for sites 4, 5, and 7, respectively. These low correlation values are because the pressure and temperature signals exhibit zero-lag correlations

in some sections and lagged correlations in others, where temperature lags the pressure (Figures 4.8a, 4.8c, and 4.8e). Even if we consider the correlation coefficients as acceptable and correct the pressure data for temperature fluctuations, no appreciable changes are observed in the output signal (see Appendix G). We also observed that the lag of the temperature variable increased with increasing distance from the coast (Figure 4.8). Gombert et al. (2019) obtained similar results.

Similarly, we correlated sea surface temperature data (El Niño 3.4 region) with ocean-bottom pressure observations to find ENSO-related low-frequency oscillations that could mask the slow events. We obtained peak correlation values of 0.33 and 0.26 for sites 4 and 5, respectively, where SST lags seafloor pressure (Figure 4.9). In contrast, the correlation with site 7 yielded a peak value of 0.30, where SST precedes the pressure (Figure 4.9). In this analysis, we expected sea surface temperature to precede pressure as in the latter case, because the ENSO signal induces changes in sea level height. However, the correlation value at site 7 was too low.

We know that the El Niño phenomenon is originated by equatorial Kelvin waves propagating along the Equator until they reach the west coast of South America, where they become coastal Kelvin waves. Then, Kelvin waves propagate poleward in both hemispheres along the eastern Pacific coast. Our results do not show any significant relation between seafloor pressure and SST because ENSO Kelvin coastal waves decrease exponentially as they move away from the coastline (Wang, 2002). Consequently, we did not perform this correction.

Tectonic deformation

From 2018 to 2022, three slow earthquakes occurred (see Figure 2.10): (1) Nov-11-2018 to Jul-20-2019, (2) Feb-18-2018 to Jun-1-2018, and (3) Aug-1-2021 to Mar-1-2022. Figure 5.1 shows that using the reference pressure decreased the oceanographic noise at site 4. However, there are still oscillations at site 5 that could not be eliminated, which obscures the tectonic signal of interest. This analysis confirms that nontidal noise is optimally eliminated when the depth difference is small (see Section 5.3 for more details). However, that difference at both sites is still significant.

We also used the complex empirical orthogonal function method to reduce the variability in the ocean-bottom pressure measurements. The advantage of the CEOF method over the basic empirical orthogonal function method is that it can capture temporal and non-temporal effects co-occurring at different points in a region (Watts et al., 2021). Here, CEOF1 represents low-frequency or seasonal variations, whereas the other CEOF modes capture high-frequency or non-seasonal variations.

Then, CEOF1 and CEOF1+2 were subtracted from observation stations 4 and 5. At site

4 (Figure 5.1), in addition to increasing the variability by 0.01 hPa, both methods failed to reveal any possible tectonic deformation pattern in the periods when slow earthquakes occurred according to the CAYA GPS displacement plot. Interestingly, the residual time series of CEOF1 and CEOF1+2 made the signal at site 4 noisier; therefore, it was more difficult to detect any slow slip (Figure 5.1).

The results for site 5 (Figure 5.2) probably suggest trends associated with tectonic deformation of the seafloor. In the residual time series obtained using the reference pressure, SSE-like pressure changes are observed, e.g., during SSE-2¹ occurs a decrease in pressure (seabed uplift) and subsequently a positive pressure trend (seabed subsidence). Prior to the release of seismic energy in a SSE, the upper plate undergoes subsidence (inter-SSE stage), while in the development of a slow earthquake, the plate is expected to rise (co-SSE stage, see Figure 2.7). This same trend was observed in the residual time series of CEOF1, and even more evident in CEOF1+2 (Figure 5.2). The deformation of SSE-3 is only clearly seen in the reference time series, and to a lesser extent in that of CEOF1+2.

Regarding the pressure signals corrected for temperature fluctuations for sites 4 and 5 (Figure G.3), the reduction in variability was quite similar to that observed in the signals shown in Figures 5.1 and 5.2. Furthermore, it was not possible to eliminate the short-period signals after filtering at site 5.

At site 5, nontidal oscillations² may have distorted the recorded signals of slow events. We know this because the standard deviation of the seafloor temperature at site 5 is 0.18, i.e., six times higher than that at station 4. Therefore, it is likely that a combination of local oceanographic and meteorological phenomena (e.g., Niiler et al., 1993; Inazu and Hino, 2011) or seafloor topography affected the pressure gradient, increasing the noise in the observations and, consequently, the bottom temperature at site 5.

Our research suggests that ocean-bottom currents could perturb the pressure gradient, which would explain the high variability observed at site 5. In addition, ocean internal waves can travel for many hours because their amplitude is greater than that of surface waves (Munk, 1981). There are three internal wave generation mechanisms: wind, Moon- and Sun-generated tidal flow (breaking lee waves), and quasi-steady flow (MacKinnon, 2013). The latter two mechanisms interact nonlinearly with the rough seafloor topography, contributing to turbulent deep-ocean mixing (e.g., Garabato et al., 2004).

¹If SSE-2 is used as a proxy in the search for its offshore propagation, it is possible that an SSE in the area between the coast and the trench may occur just before SSE-2. The notable pressure decline by approximately 2-3 hPa just before SSE-2 may be indicative of an independent offshore SSE.

²Chierici et al. (2016) studied the seafloor deformation of Campi Flegrei Caldera using bottom pressure and sea level data, which allowed identification of the tectonic signals associated with volcanic activity at this site. However, the residual bottom pressure data exhibit significant notidal oscillation.

It is well known that internal waves generated by tidal flow and wind forcing on the ocean surface occur on a global scale (Nikurashin and Ferrari, 2013), then, all the pressure measurement sites in this study were subject to internal wave effects. In addition, the interaction of tidal flow over ocean floor topography (such as ocean ridges and seamounts) generates another type of internal wave, known as internal lee waves (Garrett and Kunze, 2007). When they become unstable, these internal waves break, transferring their energy to local turbulent processes (Aucan et al., 2006). Therefore, we believe that small-scale topography played a key role in changes to the pressure gradient and, in turn, in the bottom temperature at site 5 (Figure 5.4). This would explain why the residual pressure signal at station 5 differs from the other observations (see Section 5.3).

The difference in the residual signals obtained from the three methods at both sites is crucial in determining whether the amplitude of slow events propagated beyond the coast. At site 5, we observed changes in the pressure trend that suggest tectonic deformation by slow earthquakes, while at site 4, there is no such trend. This difference may suggest that the deformation did not propagate to that site or that the signal was too weak to be recorded by the pressure sensor.

Power spectra of the residual bottom pressure

We further calculated the power spectrum of the ocean-bottom pressure signal after applying the methods of reference-site, CEOF1, and CEOF1+2. In this case, the power spectrum helps determine the frequency band in which the corrections effectively reduce the variability (Muramoto et al., 2019). Figure 5.5a shows that at site 4, correction using the reference pressure was effective for the entire frequency band. However, the CEOF1 and CEOF1+2 methods failed to reduce low- and high-frequency oscillations.

At site 5, a strong peak is observed in all three time series, indicating that none of the three corrections were effective (Figure 5.5b). In the 0.011-0.016 CPD frequency band (90-60 days), all three corrections reduced the high-frequency variability, with the reference method being the most effective (Figure 5.5b). In the low-frequency band, the CEOF1 correction performs slightly better than the CEOF1+2 correction, whereas the CEOF1+2 correction is more effective at high frequencies. We can confirm that subtracting a nearby station effectively reduced seasonal and long-period oscillations. Furthermore, the CEOF1 correction at both sites achieves a slightly higher variance reduction at low frequencies.

Pitch and roll measurements

The tilt measurements at site 4 are noisier than those at site 5, where it was assumed that greater oceanographic noise was caused by the interaction of bottom currents with the local

topography. There was no evidence of slow earthquakes at either site. However, the coseismic signal of the 2021 Acapulco earthquake was observed at site 5. The next question is why the bottom pressure sensor did not record the coseismic displacement. It is possible that the Acapulco earthquake resulted in a permanent tilt change at the OBP-5 location despite the absence of vertical motion of the pressure sensor. This hypothesis is based on the fact that tiltmeter 5 did not register the earthquake as a “peak” (see Tsuji et al., 2023) but rather as a “discontinuity” in the data.

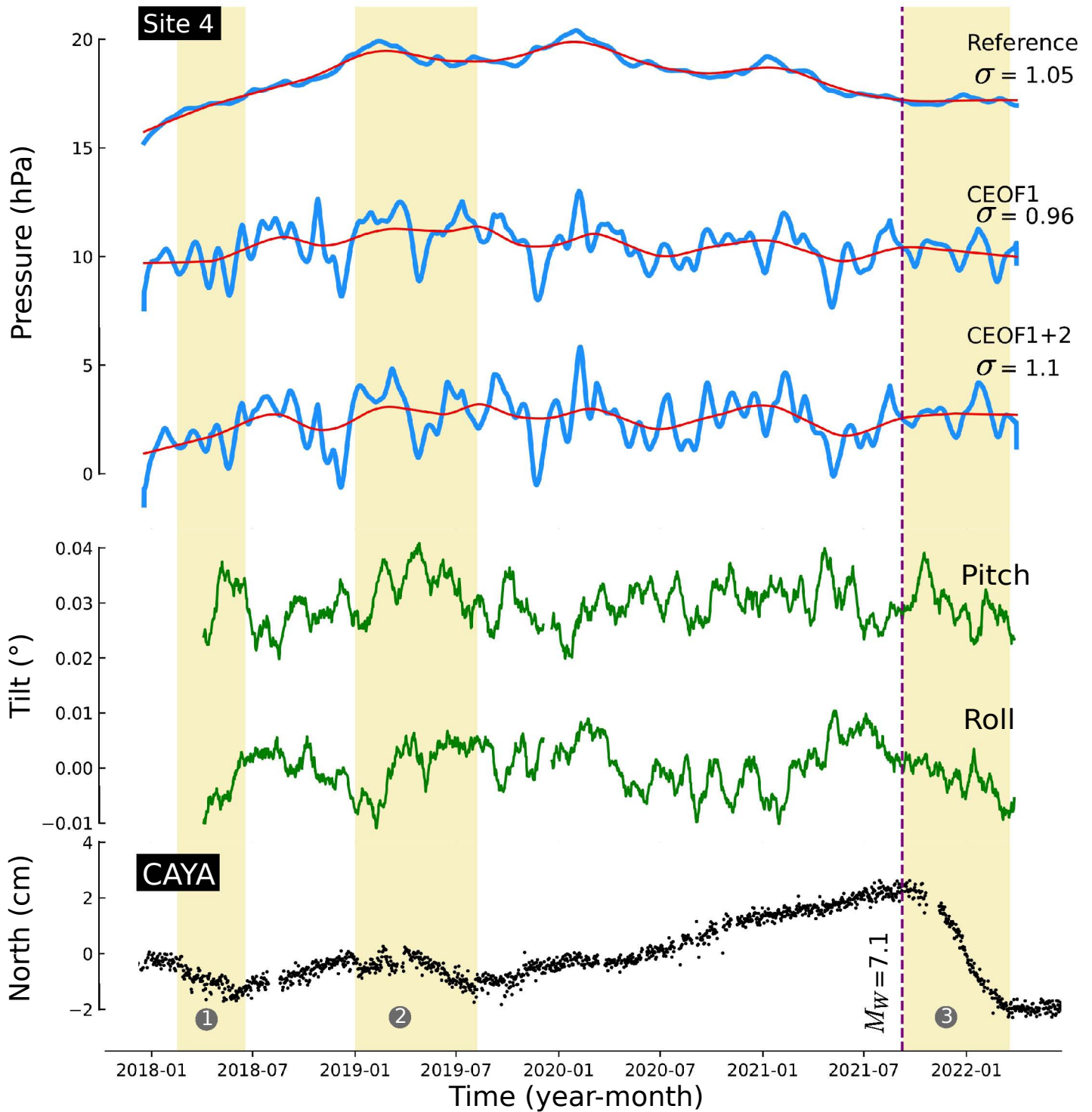


Figure 5.1. Residual ocean-bottom pressure time series at site 4 obtained using three methods: reference, CEOF1, and CEOF1+2 (the first three upper time series). Pitch and roll time series after applying a 61-day centered moving average showed no evidence of coseismic displacement or transient deformation associated with SSEs. GPS displacement at CAYA provides the first evidence of slow earthquakes (yellow vertical bands) in the Guerrero seismic gap. LOESS smoothing was applied with a window parameter of $f_L = 0.15$.

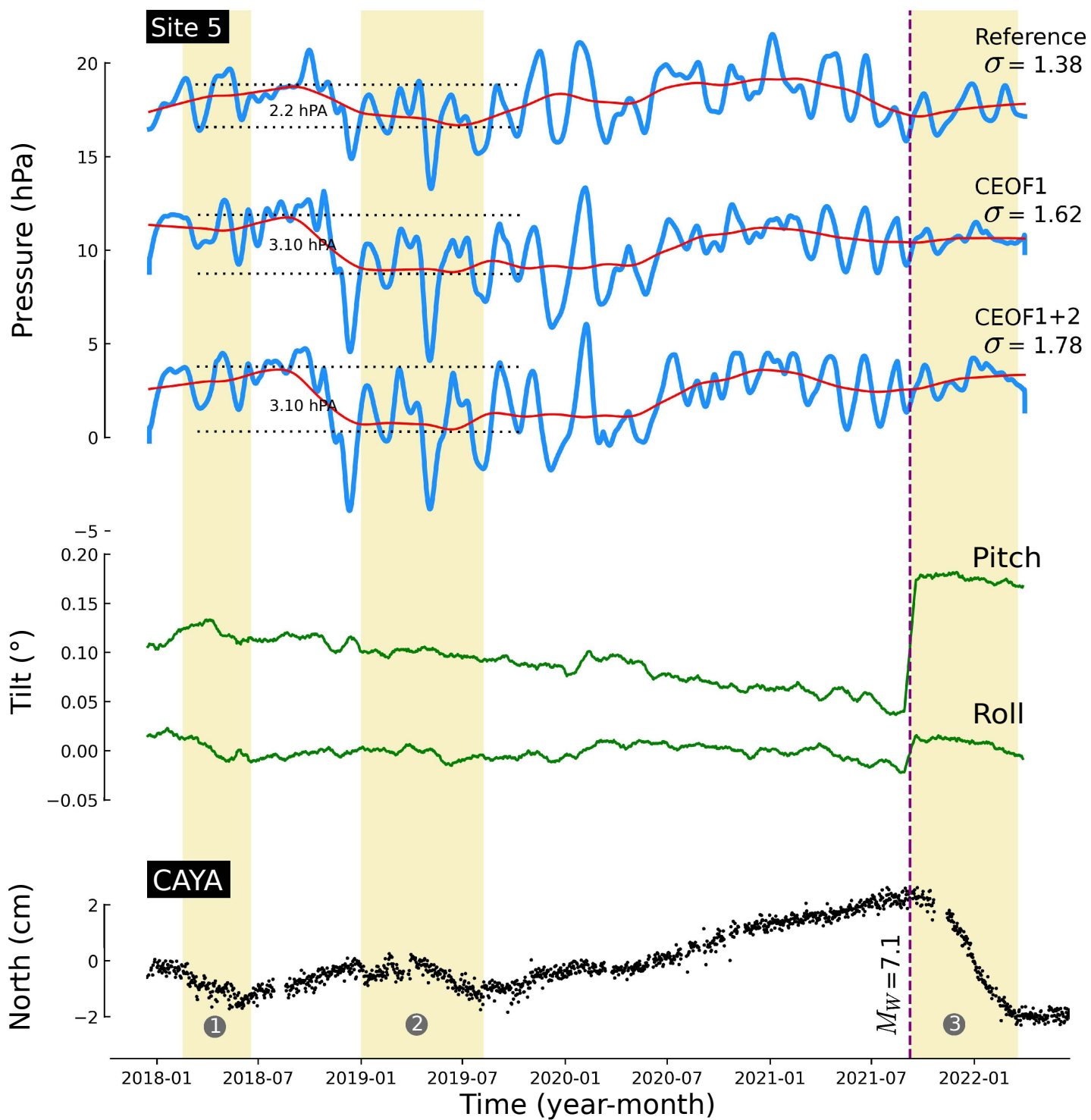


Figure 5.2. Residual ocean-bottom pressure time series at site 5 obtained using three methods: reference, CEOF1, and CEOF1+2 (the first three upper time series). Pitch time series shows a 0.02° coseismic displacement related to the 2021 $M_W 7.1$ Acapulco earthquake, while in the roll measurements the coseismic displacement is of 0.0059° . GPS displacement at CAYA provides the first evidence of slow earthquakes (yellow vertical bands) in the Guerrero seismic gap. LOESS smoothing was applied with a window parameter of $f_L = 0.15$

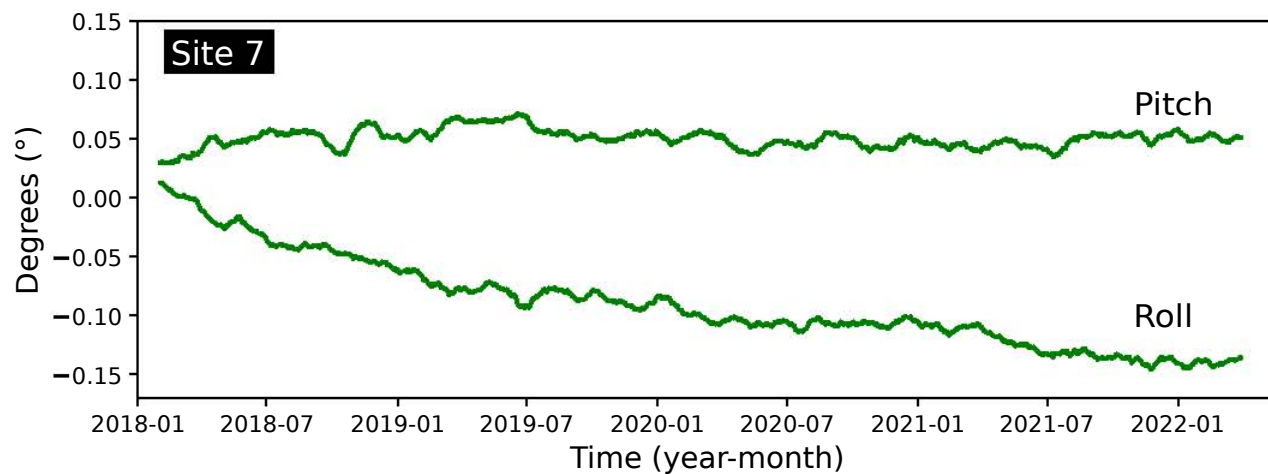


Figure 5.3. Seafloor tilt measurements at site 7. The series do not show any coseismic displacement, only the long-term trend of the roll sensor seems to indicate Cocos plate subduction.

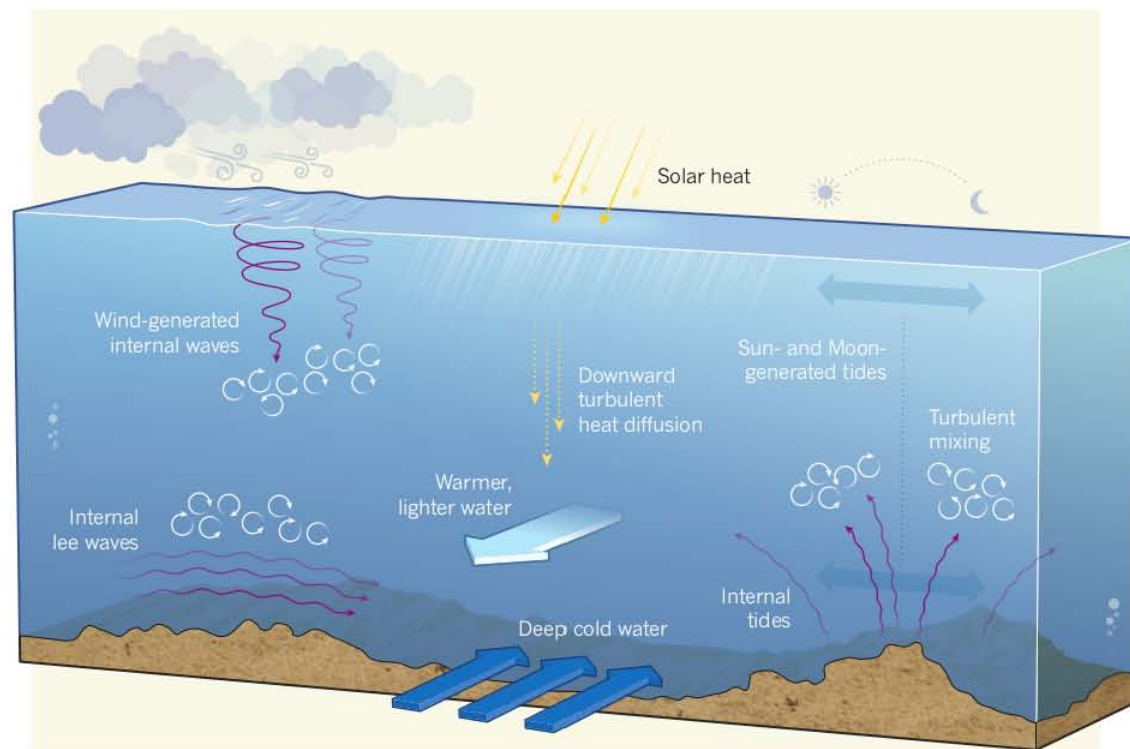


Figure 5.4. Turbulent mixing in the deep ocean due to the interaction of internal waves with the seafloor topography. Most of the deep-ocean mixing is caused by breaking lee waves. From MacKinnon (2013).

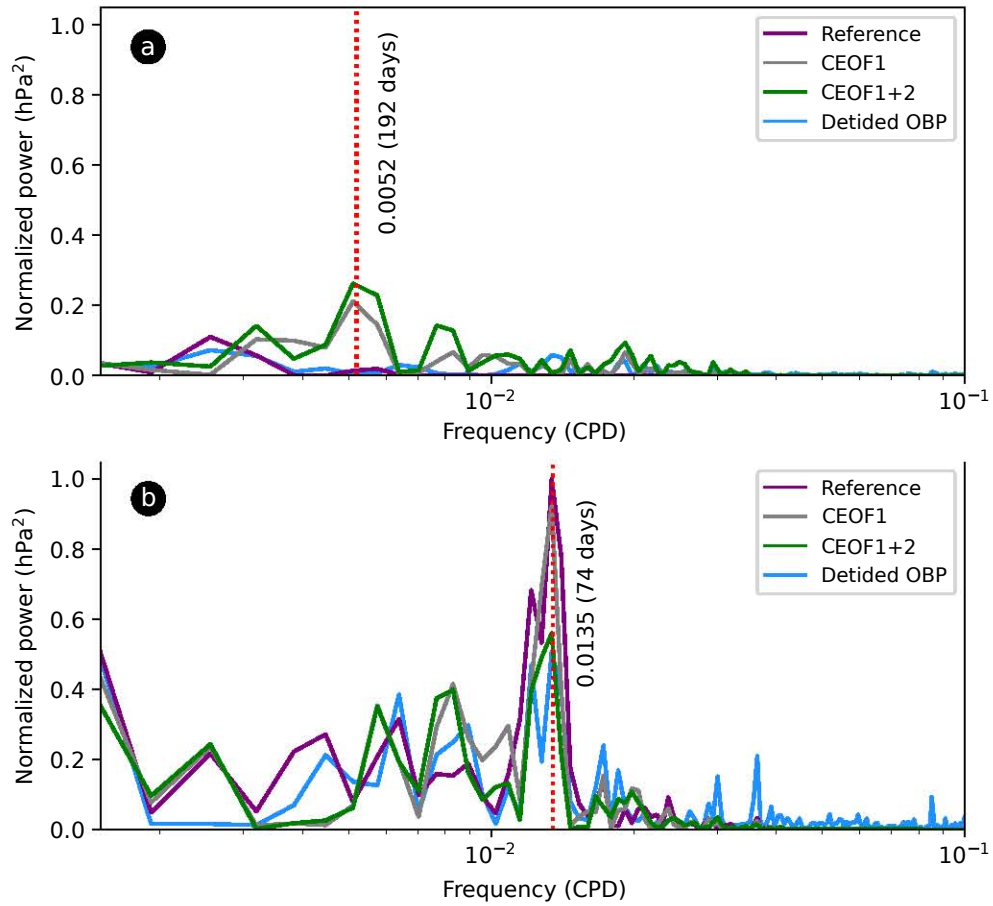


Figure 5.5. Normalized power spectra of seafloor pressure data corrected using the reference-site, CEOF1, and CEOF1+2 methods. (a) Site 4 and (b) site 5. The energy spectra were normalized by the corresponding maximum spectral peak. CPD: cycles per day.

5.1.2 Coastal sea level

Correlations with environmental observations

We did not correct the sea level data for temperature and atmospheric pressure because the correlation functions showed no significant similarity throughout the observation period (Figure 4.15). To measure the effectiveness of such corrections, mathematical evaluations should be performed, and other external factors should be taken into account because the maximum positive correlations oscillate sharply at both sites.

On the other hand, the correlation functions of the sea level and sea surface temperature data (El Niño 3.4) produced low similarity values: 0.30 at Acapulco station and 0.36 at Manzanillo station (Figure 4.16). It is expected that coastal sea level observations are affected by low-frequency ENSO signals because these waves travel as coastal trapped Kelvin waves. According to Figure 4.14, the Acapulco and Manzanillo sea level time series after filtering revealed shorter-period fluctuations that were probably related to atmospheric forcing. Therefore, these fluctuations also affect the correlation analysis. It is important to consider that we are only using 4 years of observation; therefore, at least 20 years are needed to correlate with phenomena of this type (Chelton, 2024). According to Table H.1, during the period of this experiment ³, the intensity of El Niño/La Niña was weak or moderate.

Tectonic deformation

We also analyzed sea level data from Acapulco bay (located at the southern end of the seismic gap) and Manzanillo stations to identify tectonic signals of slow events. In this case, we used only the reference station method.

According to Figure 5.6, there is no indication of a signal trend associated with SSE-2. In SSE-3, which started at the same time as the 2021 Acapulco earthquake, we observe a decrease in sea level, i.e., a coastal uplift. Effectively, vertical displacement occurred tectonically to generate the observed signal trend. However, it is difficult to attribute the cause to a single phenomenon (SSE-3 or the postseismic deformation of the 2021 earthquake) or both.

Although, we can be sure that the decrease in sea level (coastal uplift) in yellow band 3 (Figure 5.6) was mainly due to the postseismic deformation of the September 8, 2021 earthquake because we have evidence of that coseismic signal (see Section 5.4).

Given that the Acapulco tide gauge station is located on the coast, where GPS⁴ stations

³Independent component analysis (ICA) method has produced excellent results in identifying the ENSO wave signal using sea level data from other periods. However, differences in the amplitude and duration between ENSO signals and sea level have been observed. More research is needed on this topic.

⁴The CAYA station is located ~ 60 northwest of Acapulco. Hence, it is essential to have more GPS stations in

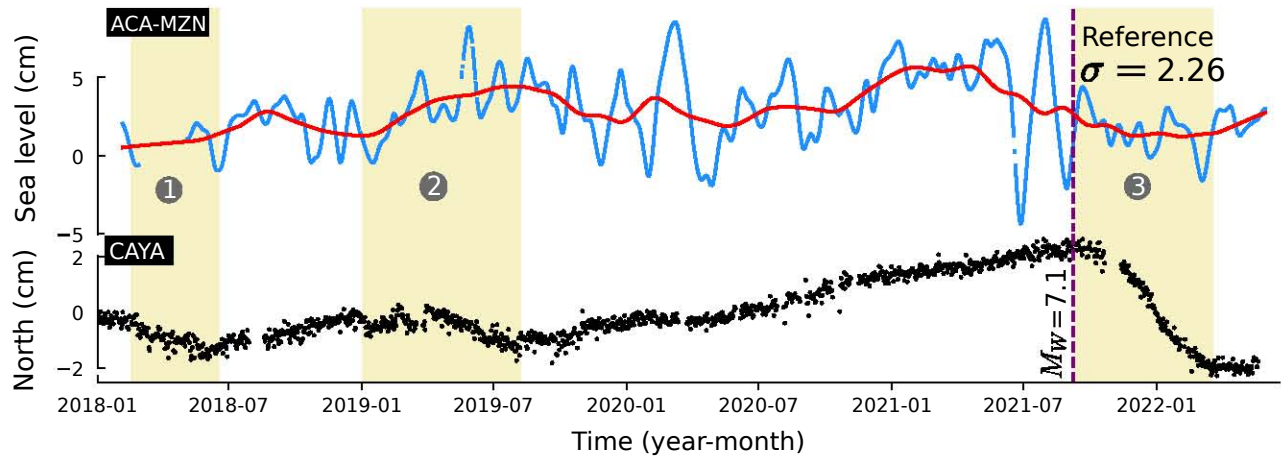


Figure 5.6. Residual sea level time series obtained using the reference-station method. The coseismic displacement generated by the 2021 Acapulco earthquake was corrected by adding 19.156 cm to the displaced signal. LOESS smoothing was applied with a window parameter of $f_L = 0.1$

record slow earthquakes, the following question arises: Why is it not possible to detect slow earthquakes in coastal sea level observations? This may occur because the vertical displacement amplitudes of slow events are not spatially uniform (e.g., Cruz-Atienza et al., 2021), indicating that slips from slow events vary across the seismic gap.

Another possibility is that the tide gauge station is located on a seismic asperity (Das and Kostrov, 1983), implying that significant deformation occurs only in coseismic slip areas that rupture such asperities, as observed in the 2021 Acapulco earthquake. It is important to keep in mind that the Acapulco tide gauge station is outside the zone of slow slip events (Cruz-Atienza et al., 2021). Another point to consider is how slow earthquakes in the Guerrero seismic gap interact with seismic asperities and how they affect the stress fields of these patches (Rousset, 2019).

In addition, it is essential to mention that the standard deviation of the sea level time series, $\sigma = 2.26$, is 2.15 and 1.64 times higher than the pressure data obtained at sites 4 and 5, respectively. This result proves that coastal measurements are more susceptible to nontidal signals. Therefore, advanced techniques for removing environmental effects, such as those caused by pressure and temperature, are required to detect relatively slow vertical displacements in sea level data.

the Guerrero seismic gap region.

5.2 Long-term trend in pressure sensor 7

By analyzing the bathymetric tilt angles at site 7, we found that the incoming Cocos plate's motion contributes $\sim 3\%$ (Table 4.1) to the sensor tilt observed in the pressure measurements. Therefore, subduction of the Cocos plate did not affect the seafloor pressure measurements significantly.

Among the factors that could have influenced the observed long-term drift values (Table 4.2, reference sites 6 and 7) is the installation depth. It has been documented that the deeper the pressure sensors are installed, the more likely they are to experience significant sensor drift. However, this correlation does not always hold (Polster et al., 2009). Therefore, sensor tests, such as simulations of *in situ* pressure conditions, are recommended to find a possible correlation between sensor drift and depth (e.g., Matsumoto and Araki, 2021).

Another possible cause could be related to the motion of the faulting structures of the subducting Cocos plate, such as horsts and grabens, where reference pressure sensors are assumed to have been placed (Figure 5.7). Ranero et al. (2003) identified bending-related faulting structures in the Cocos plate off Costa Rica by studying the structure of the incoming plate with seismic profiles, suggesting that similar structures also exist in the Middle American trench off the Guerrero coast. Chapple and Forsyth (1979) concluded that normal faults are the predominant structures in trench environments, and compressional faulting systems are rare.

Outer-rise seismicity could significantly affect the ocean-bottom pressure signals recorded at the reference sites. The sensor at site 7 may have experienced additional subsidence. However, it is still difficult to separate the effects of the tectonic environment from the long-term instrumental drift that sensors may experience. It follows that tectonic conditions and sensor drift caused the observed long-term trends in the pressure measurements at sites 6 and 7.

As mentioned above, tests must be performed before deploying this type of instrumentation in future experiments. This is especially important because the study of slow earthquakes in deep-sea environments is carried out using instruments deployed on the ocean floor, and long-term pressure records may be obscured not only by nontidal signals but also by sensor drift. Numerous studies of sensor drift have been conducted using ocean-bottom sensors (e.g., Matsumoto and Araki, 2021; Polster et al., 2009; Watts and Kontoyiannis, 1990), but more effective methods for drift removal are needed for long-term observations.

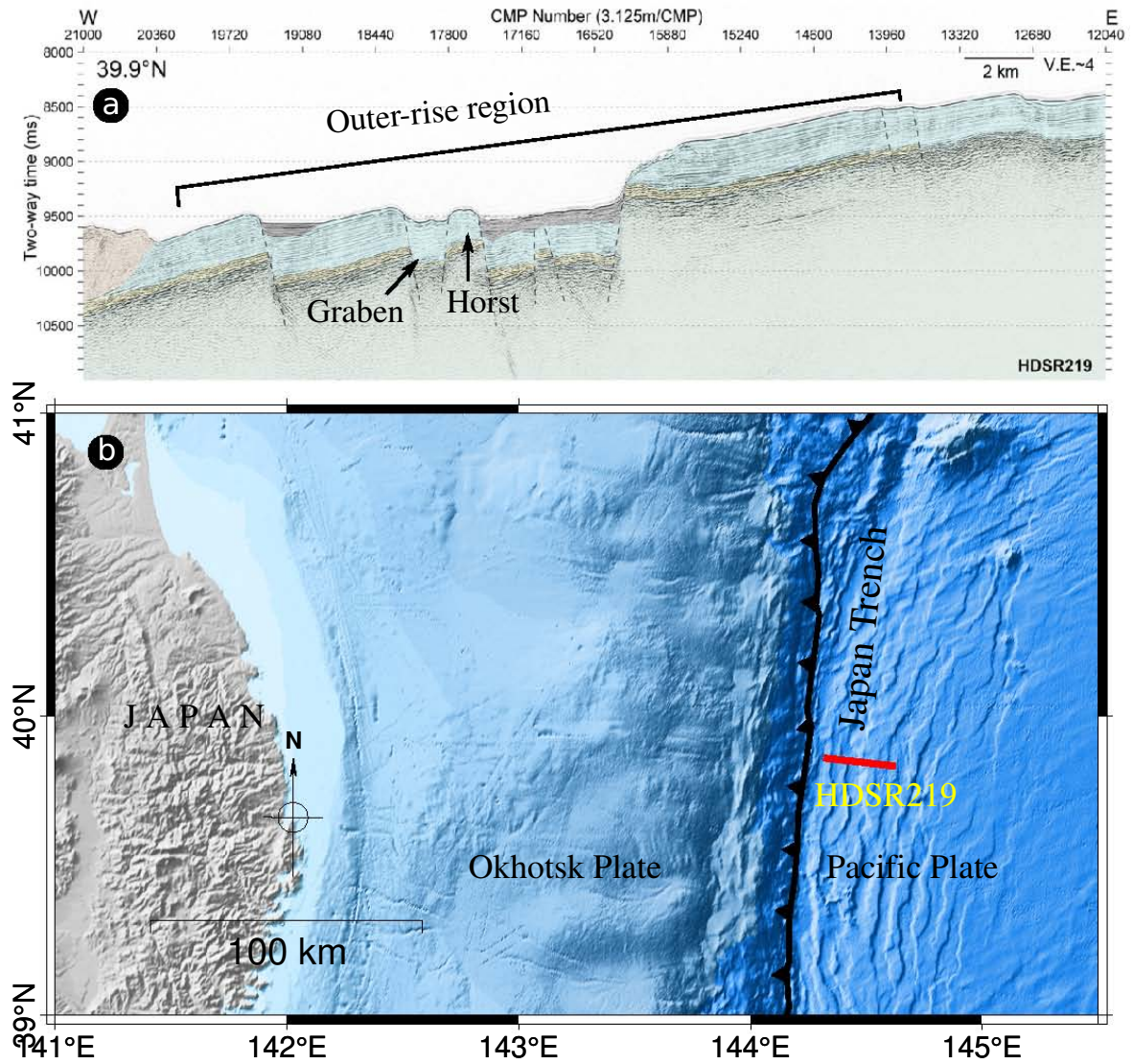


Figure 5.7. Seismic line in the Japan Trench. (a) Bending-related normal faults are represented by black dashed lines. Outer-rise seismicity originates in bending-related faulting systems (outer-rise region) where the incoming plate curvature is highest. (b) Map of the seismic line (red line). Adapted from Nakamura et al. (2023).

5.3 Coherence between pairs of nontidal ocean-bottom pressure signals

We assessed the design of the SATREPS seafloor sensor array by computing the coherence between the nontidal pressure observations, considering both the distance and depth differences between pair-wise pressure signals. According to the Pearson correlation (C_p) values obtained for the three pairs of stations, the similarity value of $C_p = 0.68$ for pair 4-7 (2,618 m depth difference) was better than that for pair 4-5 (1,401 m depth difference), where a value of $C_p = 0.05$ was obtained (Figure 5.8). The pair 5-7, which had the largest difference in depth, had the lowest similarity ($C_p = -0.08$). Figure 5.8 shows that site pairs 4-7 and 4-5 had the same separation distance of 22 km. However, Inoue et al. (2021) and Fredrickson et al. (2019) concluded that an excellent correlation between two seafloor pressure time series can be achieved when the difference in depth between the two observation sites is small.

It is clear that the depth distance between stations 4 and 5 was the smallest in the sensor array; consequently, the question arises as to why the correlation was very low. There are two explanations for the above situation: (1) Only three stations were evaluated compared with the many measurement sites used in previous studies. For example, Inoue et al. (2021) also obtained some results that do not agree with the difference in depth, but there were few exceptions; therefore, our results may be in that group. (2) According to Figure 5.8, the signal shapes of sensors 4 and 7 are similar to that of sensor 5. This difference may be attributed to the strong influence of internal waves on the seafloor topography at site 5, which affects the pressure gradient.

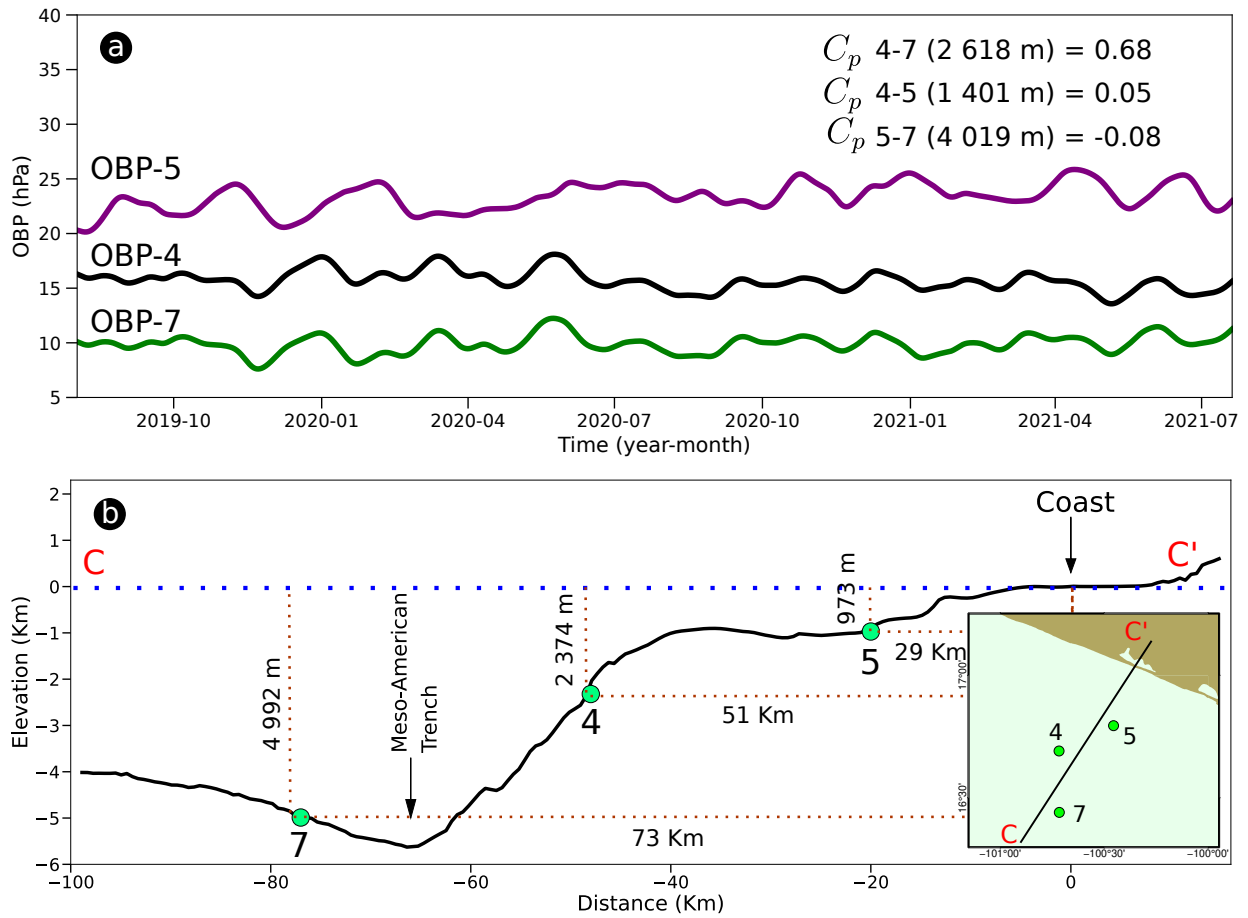


Figure 5.8. Coherence between 30-day filtered seafloor pressure signals. (a) Correlation coefficients and depth differences for each wise-pair residual pressure. We used a 717-day data window (Aug-02-2019 to Jul-19-2021) for each site, in which we omitted SSE-1 and SSE-2. (b) Bathymetric profile along OBP-7. The depths of each station and their distances from the Pacific coast of Guerrero are shown. See the map on the lower right side for a reference.

5.4 Coseismic signal of the 2021 Acapulco earthquake

The vertical coseismic displacement of the Acapulco earthquake of September 7, 2021 (01:47:46 UTC), with a magnitude of $M_W = 7.1$, was calculated using sea level measurements. These measurements were obtained from the Acapulco tide gauge stations of the SMN and SEMAR. At the SMN station, the displacement was 19.071 cm, while at the SEMAR station, which is 6.4 km away, the displacement was 19.243 cm. This resulted in an average coseismic displacement $\bar{D}_c = 19.157$ cm and an absolute difference between the values of $|\Delta D_c| = 0.172$ cm, indicating an excellent consistency of the coseismic uplift at both stations.

It is important to mention that the coseismic signal recorded by both tide gauges, SMN and SEMAR, coincided with the displacement recorded in the GPS data from the ACYA station, which was 19.21 cm. In contrast, at the ACAP and GR07 stations, the displacement was 24.2 cm and 23.55 cm, respectively (Figure 5.9). The difference is evident between the two groups of stations: those closer to Acapulco City and those farther away to the southeast. The map in Figure 5.9d shows the distribution of the InSAR LOS displacement during the Acapulco seismic event. Acapulco City is located near the edge of the 2021 earthquake rupture zone. Therefore, stations located farther from the zone of greatest ground displacement (ACYA, SMN and SEMAR) recorded smaller coseismic displacements compared to the ACAP and GR07 stations (Figure 5.9).

The above demonstrates that in cases where GPS data are not available, an alternative method to calculate the coseismic displacement of an earthquake and other parameters, such as the rupture area, is to use sea level observations (e.g., Ortiz et al., 2000).

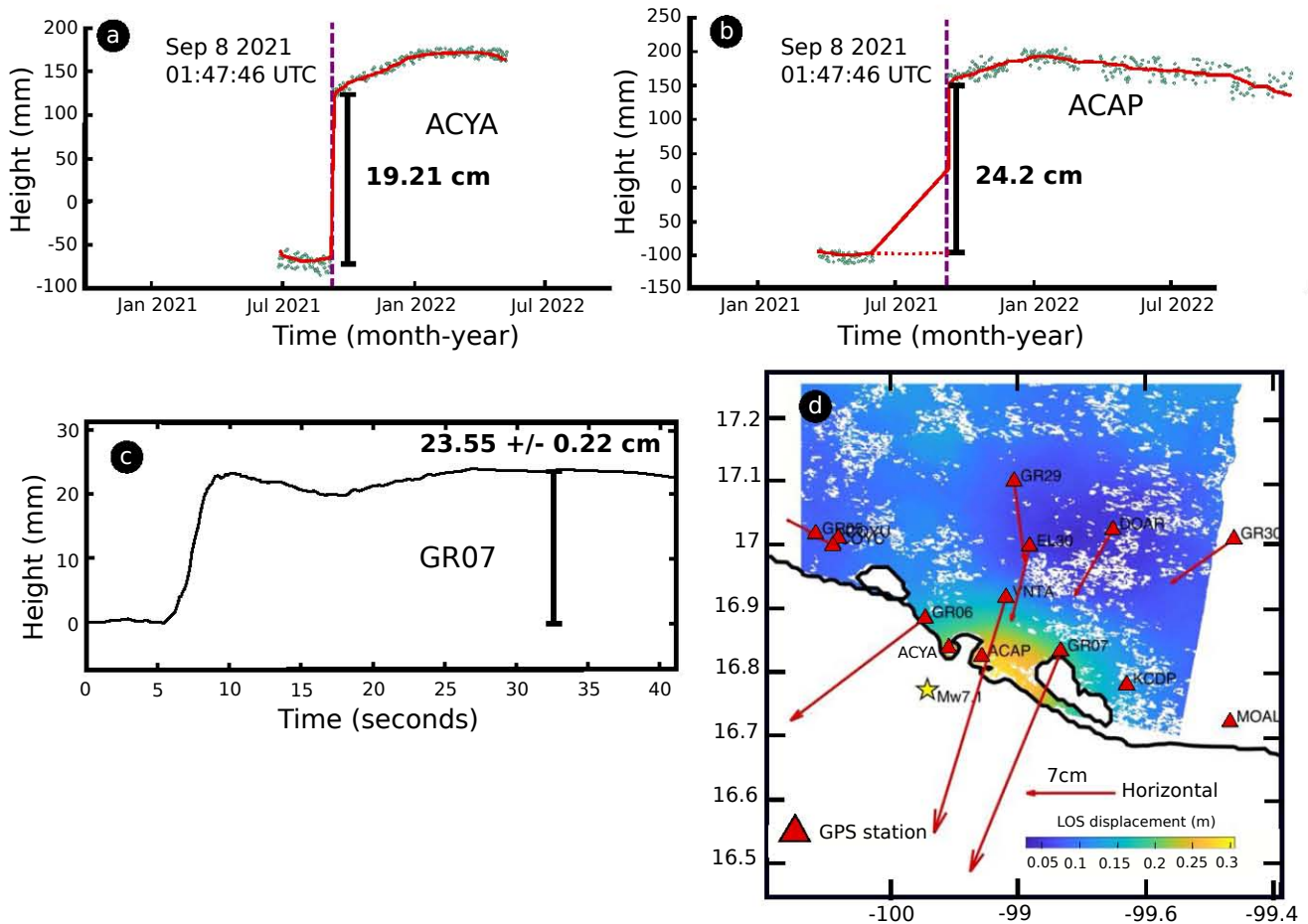


Figure 5.9. GPS time series of the (a) ACYA and (b) ACAP stations located in Acapulco Bay. These stations recorded the coseismic signal generated by the 2021 Acapulco earthquake. The coseismic displacement at the ACYA station matches the value obtained from the two tide gauge stations. The ACYA station and the Acapulco tide gauge station are at the same site. The ACAP and (c) GR07 stations recorded similar vertical displacements. (d) InSAR LOS displacement map of the 2021 Acapulco earthquake. Sources: Suárez (2024) and Cruz-Atienza (2024).

5.5 Tsunamis

5.5.1 Main characteristics of tsunami signals

According to the tsunami event records (Figures 4.20, 4.21, 4.22, 4.23, and 4.24), the arrival time, maximum amplitude, and maximum valley-crest distance of the wave train are summarized in Table 5.1. It can be observed that the 2022 Tonga eruption, despite the remoteness of the sea level stations from the source region, produced the maximum tsunami amplitudes during the period 2017-2022. This tsunami had a maximum amplitude of 111.53 cm and a crest-valley distance of 209.08 cm at Manzanillo station. A minimum amplitude of 17.21 cm and a crest-valley distance of 30.74 cm (New Zealand tsunami) were recorded at the same station.

5.5.2 Characteristic frequencies

Figures 5.10 and 5.11 show the results of the Fourier spectra of the tsunamis recorded at the Acapulco and Manzanillo stations, respectively. In Acapulco Bay, the peak periods of 29, 28, 25, and 11 minutes (2.02, 2.16, 3.36, and 5.45 CPH) are common in the tsunami spectra, indicating that these are bathymetric resonance properties of the basin, which are excited in an event of this magnitude regardless of its remoteness (Zavala-Hidalgo et al., 2020). The highest linear correlation between the Fourier spectra was observed between the 2022 Tonga tsunami and the 2018 Oaxaca tsunami, with a value of 0.69. In contrast, the lowest correlation was 0.43 between the 2021 Acapulco earthquake and the 2021 New Zealand tsunami (Table 5.2).

In Manzanillo, the dominant periods are 34, 27, and 8 minutes (1.75, 2.22, and 7.40 CPH). Regarding the correlation values of the spectra, the maximum correlation was 0.77 between the 2022 Tonga and 2021 Acapulco tsunamis, and the lowest correlation was 0.61 between the 2021 New Zealand and 2017 Pijijiapan tsunamis (Table 5.2).

Table 5.1. Tsunami characteristics recorded at the Acapulco and Manzanillo tide gauge stations. TG: Tide gauge; LT: Local Time.

TG	First wave arrival (UTC)	Max. amplitude (cm)	Max. peak-to-trough height (cm)	ΔS -TG (Km)
Tonga volcanic eruption Jan/15/2022 04:14:45 UTC (Jan/14/2022 22:14:45 LT)				
ACA	Jan/15/2022 12:50:00	73.98 cm (+)	137.21	9,230
MZN	Jan/15/2022 09:00:00	116.54 cm (+)	209.08	8,910
M_W 7.1 Acapulco earthquake Sep/08/2021 01:47:46 UTC (Sep/07/2021 20:47:46 LT)				
ACA	Sep/08/2021 01:50:00	56.38 (-)	96.25	13
M_W 8.1 New Zealand earthquake Mar/04/2021 13:28:31 UTC (Mar/04/2021 13:28:31 LT)				
ACA	Mar/05/2021 08:45:00	18.55 (+)	34.87	9,775
MZN	Mar/05/2021 06:30:00	17.21 (+)	30.74	9,515
M_W 7.1 Oaxaca earthquake Feb/17/2018 17:38:00 UTC (Feb/17/2018 23:38:00 LT)				
ACA	Feb/17/2018 01:20:00	17.45 (-)	32.7	212
M_W 8.1 Chiapas earthquake Sep/08/2017 04:49:21 UTC (Sep/08/2017 23:49:21 LT)				
MZN	Sep/08/2017 06:30:00	26.27 (+)	49.68	1,190

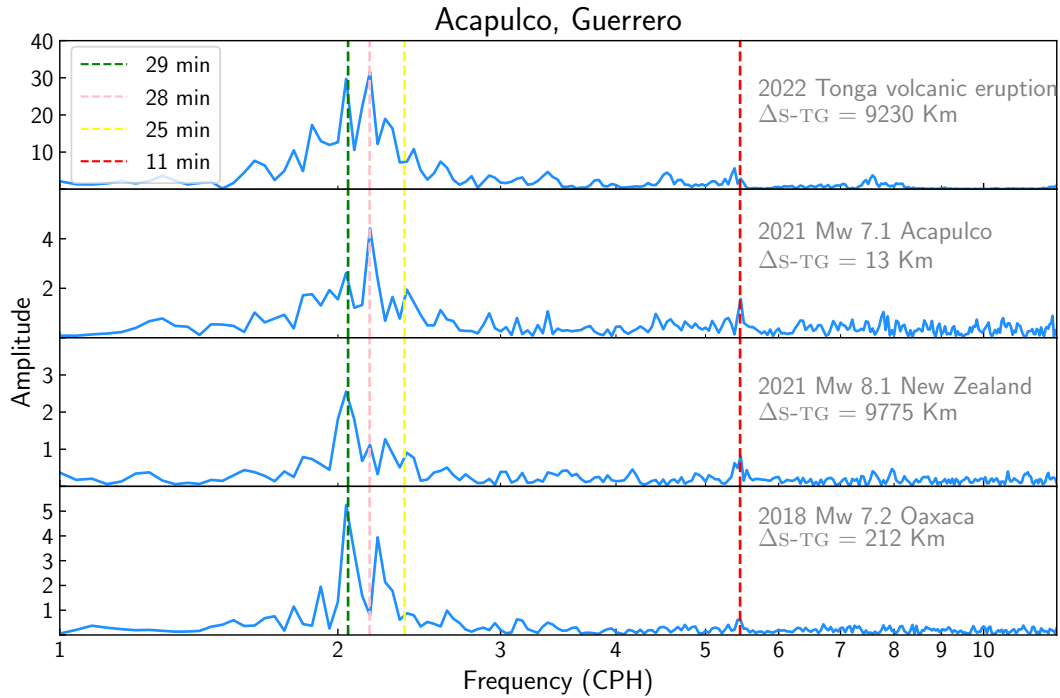


Figure 5.10. Amplitude spectra of the tsunamis recorded at the Acapulco tide gauge station. The source-to-station distances (ΔS -TG) are shown for each tsunami. The peak frequencies are indicated by dashed lines. CPH: cycles per hour.

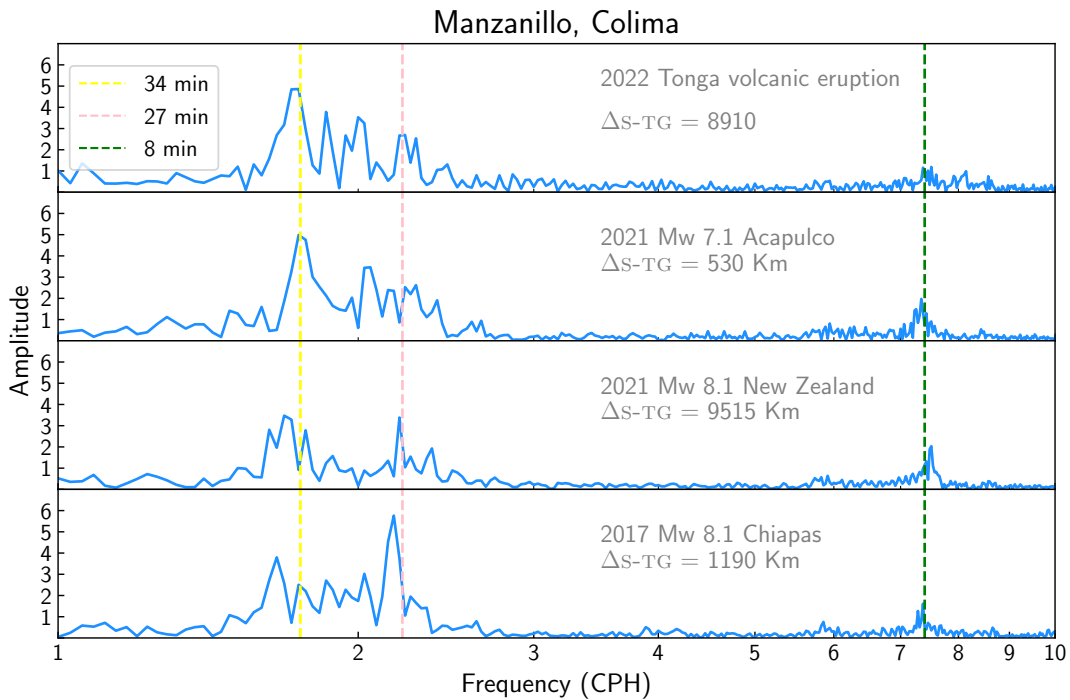


Figure 5.11. Amplitude spectra of the tsunamis recorded at the Manzanillo tide gauge station. The source-to-station distances (ΔS -TG) are shown for each tsunami. The peak frequencies are indicated by dashed lines. CPH: cycles per hour.

Table 5.2. Pearson correlation coefficients of tsunami spectral signals.

Tsunami				
Acapulco tide gauge station				
	Tonga, 2022	Acapulco, 2021	New Zealand, 2021	Oaxaca, 2018
Tonga, 2022	1	0.67	0.65	0.69
Acapulco, 2021	0.67	1	0.43	0.48
New Zealand, 2021	0.65	0.43	1	0.65
Oaxaca, 2018	0.69	0.48	0.65	1
Manzanillo tide gauge station				
	Tonga, 2022	Acapulco, 2021	New Zealand, 2021	Pijijiapan, 2017
Tonga, 2022	1	0.77	0.69	0.65
Acapulco, 2021	0.77	1	0.66	0.67
New Zealand, 2021	0.69	0.66	1	0.61
Pijijiapan, 2017	0.65	0.67	0.61	1

5.5.3 Spectral ratios

The spectra obtained for the background signal and the Tonga tsunami signal at the Acapulco and Manzanillo tide gauges (Figure 5.12), along with their corresponding spectral ratios, are crucial for reconstructing the spectral characteristics of the tsunami waves in the open ocean. According to Figure 5.12, the energy of the spectral ratios was concentrated in the frequency band of 0.3–10 CPH (200–6 minutes). The frequencies higher than 10 CPH (< 6 min) are caused by infragravity waves.

According to Rabinovich et al. (2013), in addition to reconstructing the tsunami source, tsunami spectra ratios also contain secondary signals resulting from the reflection and scattering of waves in the ocean and infragravity wave signals. Infragravity waves are ocean surface gravity waves that result from nonlinear interactions between wind waves and swell (Webb et al., 1991). Zaytsev et al. (2017) showed that the spectral signal of infragravity waves contained in spectral ratios of coastal sea level data is smaller than that obtained with ocean-bottom pressure data; this is because the design of the ports attenuates the effects of infragravity waves on the coastal sea level.

Therefore, a comparative analysis between the spectral ratios of sea level and seafloor pressure data would enable us to effectively discriminate the infragravity wave signal from the tsunami wave spectrum. This underscores the need for a permanent network of ocean-bottom pressure sensors designed to record high-frequency signals. Such a network would significantly enhance our ability to obtain more robust conclusions about tsunamis.

It is necessary to mention that the 2022 Tonga tsunami was an event that had two origins: (1) due to land displacement by the explosion of the volcano and (2) due to Lamb waves radiated by the volcanic explosion (Hu et al., 2023). Therefore, using the spectral ratio technique, we can reconstruct the source function caused by the displacement of water masses during an eruption; however, no methodology is available for the second case.

Once we calculated the source function of the 2022 Tonga tsunami for each site, we averaged the two spectral ratios of both stations to attenuate possible low-frequency noise and thus enhance the characteristic frequencies. Figure 5.13 shows the average of the ratios superimposed on those from Acapulco and Manzanillo. Spectral peak frequencies of 32, 22, 15, 7, and 5 minutes are identified for the 2022 Tonga event. These frequencies contrast with the frequency peaks typical of the Acapulco and Manzanillo basins, which are excited during tsunamigenic events (see Figures 5.10 and 5.11). However, to narrow down the above frequencies, it is necessary to expand the set of tide gauge stations used for the calculation and thus find frequencies more representative of the source that triggered the tsunami.

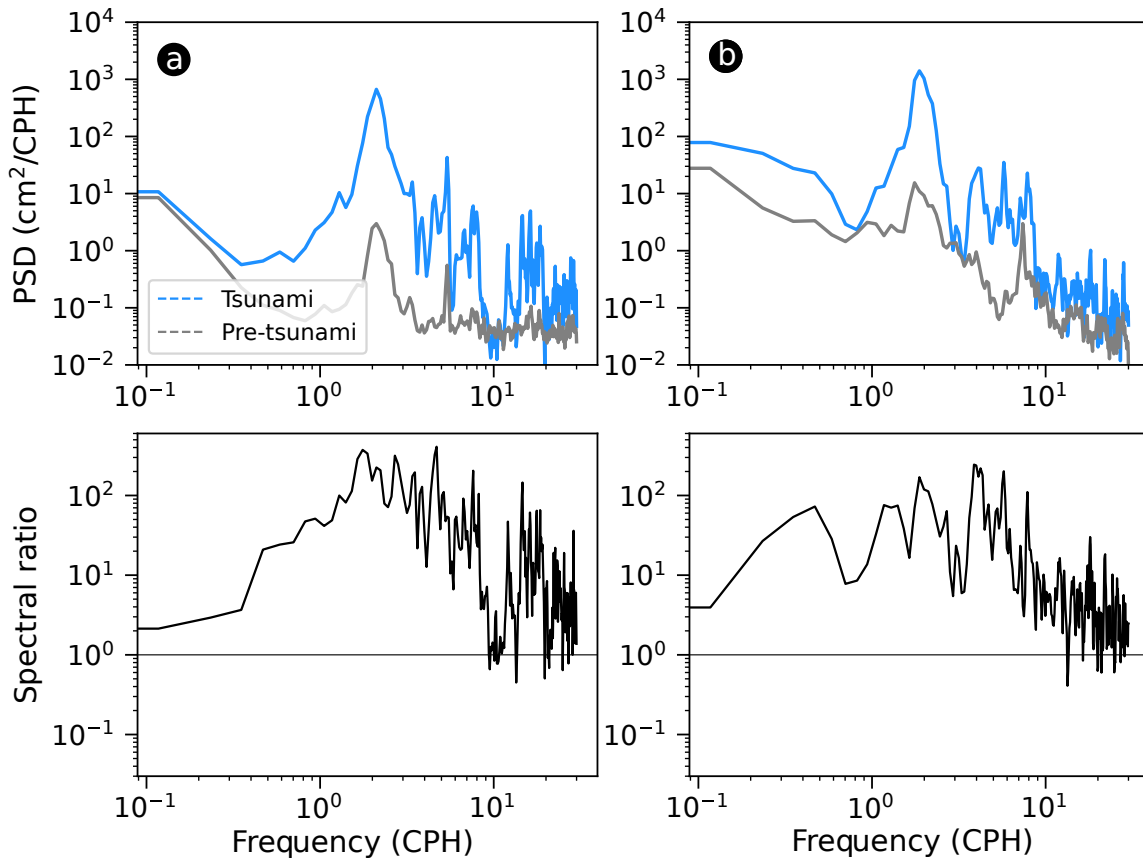


Figure 5.12. Pre-tsunami and tsunami signal spectra of the Tonga tsunami recorded by the (a) Acapulco and (b) Manzanillo tide gauge stations, as well as their (bottom) respective spectral ratios.

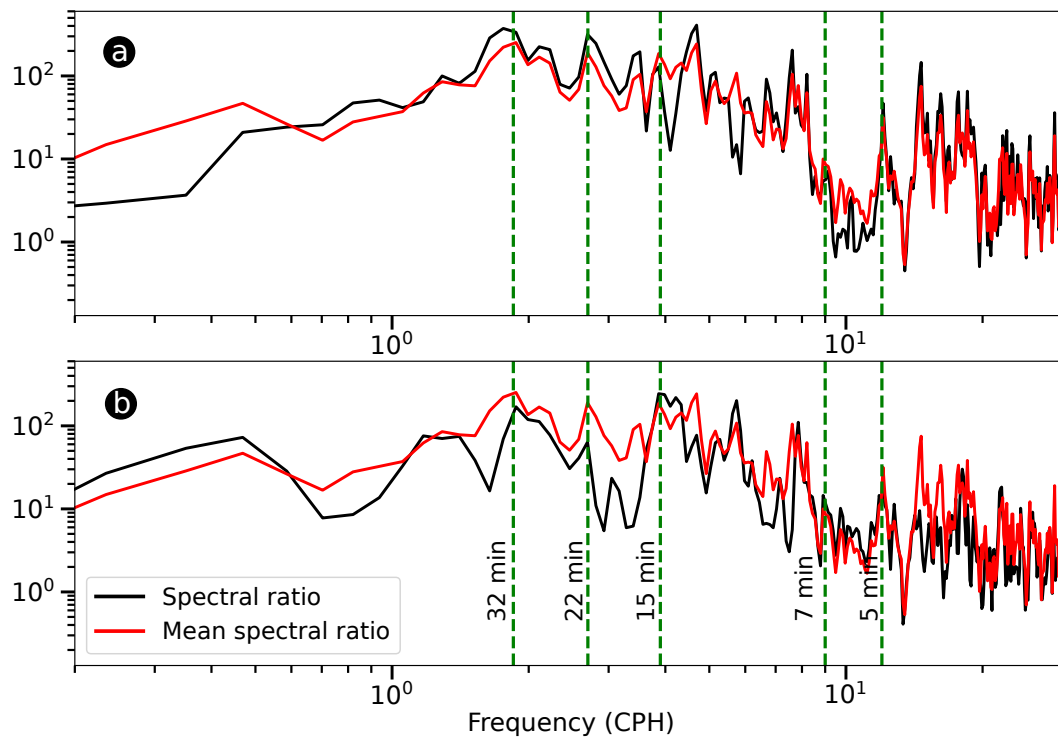


Figure 5.13. Mean spectral ratio (source function) of the 2022 Tonga tsunami obtained from the (a) Acapulco and (b) Manzanillo spectral ratios. Using the mean spectral ratio, the characteristic frequencies corresponding to periods of 32, 22, 15, 7, and 5 minutes from the Tonga tsunami’s source function were identified in both signals.

CONCLUSIONS

CHAPTER 6

Ocean-bottom pressure and sea level measurements

[1] In the residual bottom pressure measurements at site 5, signals of slow slip events are likely present, with SSE-2 being more evident than the others. However, these results are uncertain because of the pronounced residual oscillations. These oscillations are attributed to the interaction of internal waves with local topography, which contributes to turbulent deep-ocean mixing (e.g., Garabato et al., 2004).

[2] At site 4, there is no clear expression for slow earthquake signals. On the other hand, the use of CEOF1 and CEOF1+2 did not reduce the oceanographic and meteorological noise; on the contrary, it added oscillations.

[3] The pressure signals corrected for seafloor temperature fluctuations for sites 4 and 5 did not improve the detection of slow earthquake signals.

[4] The correlations of the bottom pressure observations at sites 7 and 4 have a similarity of C_p 4-7 = 0.68, while for the 5-7 pair, it is C_p 5-7 = -0.08, and the 4-5 pair, it is C_p 4-5 = 0.05. The difference in the pressure signal at site 5 to sites 4 and 7 is caused by the combination of internal waves and local seafloor topography, which caused changes in the pressure gradient and, in turn, in the bottom temperature. This is evidenced by the variability of the temperature data; at site 5, the standard deviation is $\sigma = 0.18$, 6 times larger than that at site 4 ($\sigma = 0.03$).

[5] The residual sea level measurements during SSE-1 and SSE-2 showed no evidence of tectonic signals associated with slow slip events. In contrast, deformation was clearly observed during SSE-3, which could be attributed to either the postseismic deformation of the 2021 event or a slow slip event. However, it is believed that this deformation is more likely related to the postseismic effects of the 2021 Acapulco earthquake, as the coseismic displacement of this event was recorded.

[6] Among the reasons why no slow slip event signal was observed in the sea level measurements are the fact that the amplitudes of slow events are not spatially uniform (Cruz-Atienza et al., 2021), or the location of the Acapulco tide gauge was on a seismic asperity (Das and Kostrov, 1983), which broke due to the 2021 M_W 7.1 earthquake. This explains why only the coseismic signal of this event was recorded.

[7] According to the ocean-bottom pressure and temperature plots, there is a correlation between these two signals, suggesting that a change in the pressure gradient induces changes in the bottom temperature. However, the correlations oscillate with zero lags to 7, 18, and 19 days at sites 5, 4, and

7, respectively. This is reflected in the low values obtained in the cross-correlation analysis. On the other hand, no correlation was found with SST measurements (El Niño 3.4 region).

[8] The coseismic signal of the 2021 M_W 7.1 Acapulco earthquake was not recorded in any seafloor pressure observation station; however, the vertical displacement was clear in the tilt measurements at site 5. It is possible that the OBP-5 location experienced a permanent tilt change without apparent vertical ground motion.

Long-term drift at site 7

[9] The Cocos plate's motion contributes $\sim 3\%$ to the sensor tilt observed in the pressure measurements at site 7. Therefore, the main cause of the linear trend in seafloor pressure was the sensor drift effect combined with local motion generated by the bending-related faulting structures (horsts and grabens) of the incoming Cocos Plate.

Coseismic signal of the 2021 Acapulco earthquake

[10] Sea level measurements in Acapulco bay from the Servicio Mareográfico Nacional (SMN) and Secretaría de Marina (SEMAR) tide gauges recorded the coseismic displacement caused by the Acapulco earthquake that occurred on September 8, 2021 (01:47:46 UTC). The magnitude of the coseismic displacement at the SMN tide gauge was 19.071 cm and 19.243 cm at the SEMAR station. Both measurements are similar to the displacement recorded at the ACYA station located in Acapulco Bay, which was 19.21 cm.

[11] The coseismic displacement recorded in the sea level measurements obtained in this study demonstrates that in situations where GPS measurements are not available, they can be used for studies related to tsunami and subduction zone earthquakes.

Tsunamis

[12] At the Manzanillo tide gauge station, a maximum amplitude of 116.54 cm and a corresponding crest-valley height of 209.08 cm were recorded for the 2022 Tonga tsunami. At the same time, the minimum amplitude was 17.21 cm, and the crest-valley height was 30.74 cm due to the 2021 New Zealand tsunami, as well as at the Manzanillo station.

[13] Acapulco Bay and the port of Manzanillo have particular resonance frequencies that are excited regardless of the distance from the tsunami source. In Acapulco Bay, the periods are 29, 28, 25, and 11 minutes (2.02, 2.16, 2.36, and 5.45 CPH), which coincide with those obtained by Zavala-Hidalgo et al. (2020). The port of Manzanillo has periods of 34, 27, and 8 minutes (1.75, 2.22, and 7.40 CPH).

[14] In Acapulco Bay, the highest correlation ($C_p = 0.69$) was between the 2021 Tonga and 2018 Oaxaca tsunamis, while the lowest ($C_p = 0.43$) was between the 2021 Acapulco and 2021 New Zealand tsunamis. In Manzanillo, the highest correlation ($C_p = 0.77$) was between the 2022 Tonga and 2021

Acapulco tsunamis, and the lowest ($C_p = 0.6$) was between the 2021 New Zealand and 2017 Chiapas tsunamis.

[15] The spectral ratios for the 2021 Tonga tsunami were obtained using the methodology of Rabinovich (1997), using coastal sea level observations from the Acapulco and Manzanillo ports. To suppress the frequencies associated with other types of noise and to emphasize the characteristics of the tsunami source in the open ocean, the spectral ratios were averaged. As a result, dominant periods of 32, 22, 15, 7, and 5 minutes (1.85, 2.70, 3.90, 9, and 12 CPH) were identified.

Considerations for future research

[1] The tiltmeters must have a compass, as the lack of these in this study made it difficult to estimate their orientation. As in the case of ocean-bottom pressure sensors, it is recommended that the stations be anchored on a fixed and stable base, as is usually the case in other seismic geodetic measurement networks.

[2] It is vital to constantly maintain tide gauge stations, including installing more on the Pacific coast of Mexico. The lack of data can severely affect phenomena of long duration, such as deformation by slow earthquakes, whereas in phenomena of short duration, such as tsunamis, valuable information about the source of the tsunamigenic event and the frequencies of the basin is lost.

[3] A real-time monitoring of ocean-bottom pressure off the Guerrero seismic gap, like a cable seafloor observation system, is essential for assessing seismic and tsunami hazards.

[4] Expanding the GPS network around the Guerrero seismic gap is necessary to enhance the detection and precise location of both conventional and slow earthquakes.

[5] Integrating current meters into the seafloor observation network is essential for calculating geostrophic contributions to currents and exploring potential correlations with seafloor pressure measurements.

APPENDIX A. SEISMIC SIGNALS

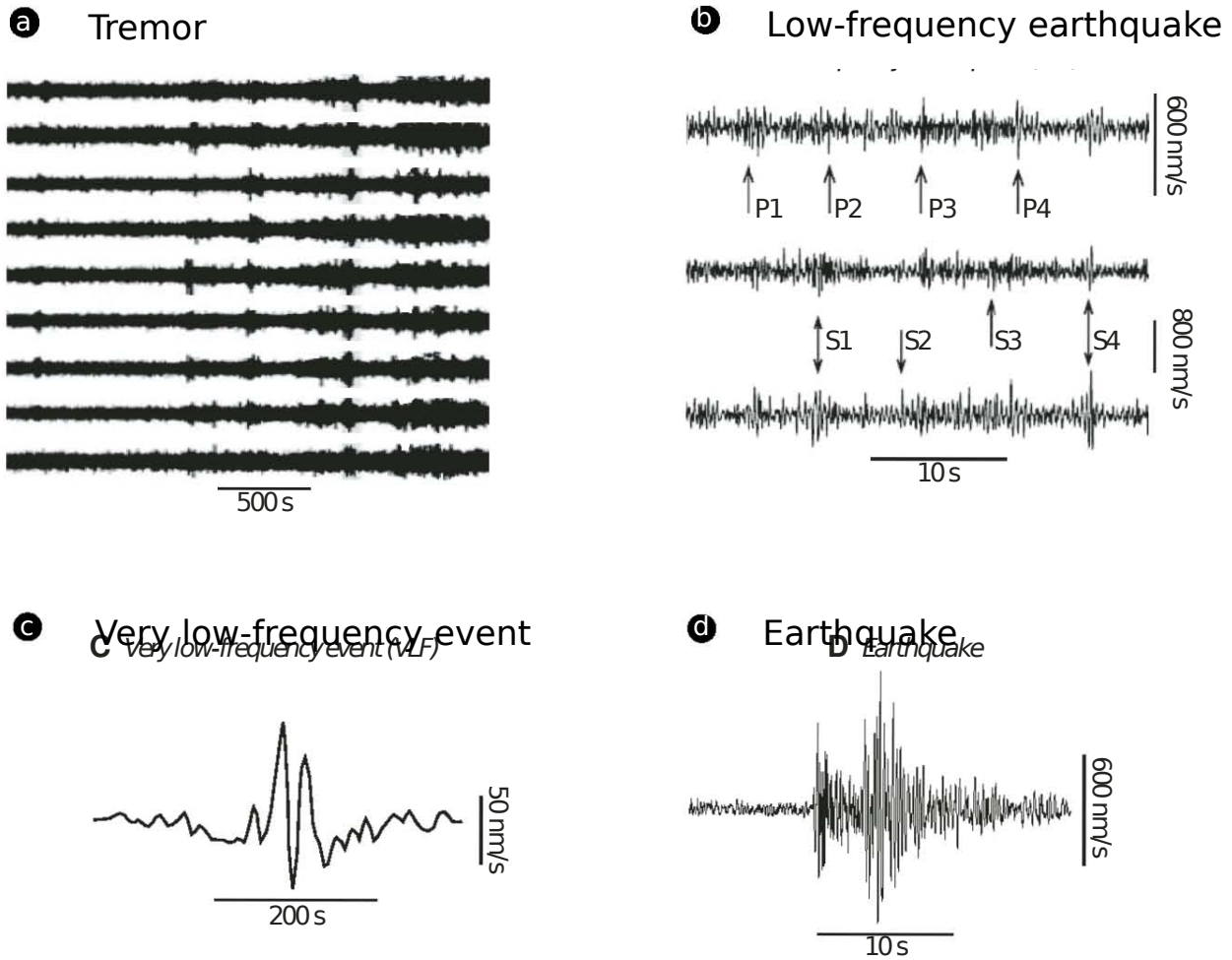


Figure A.1. Seismic signals. (a) Tremor signal recorded in Vancouver Island; (b) Low-frequency earthquakes from western Washington; (c) Very low-frequency earthquakes from the Kii Peninsula, Japan; (d) M 1.9 earthquake recorded in western Washington. Adapted from Gomberg et al. (2010).

APPENDIX B. GPS DISPLACEMENT

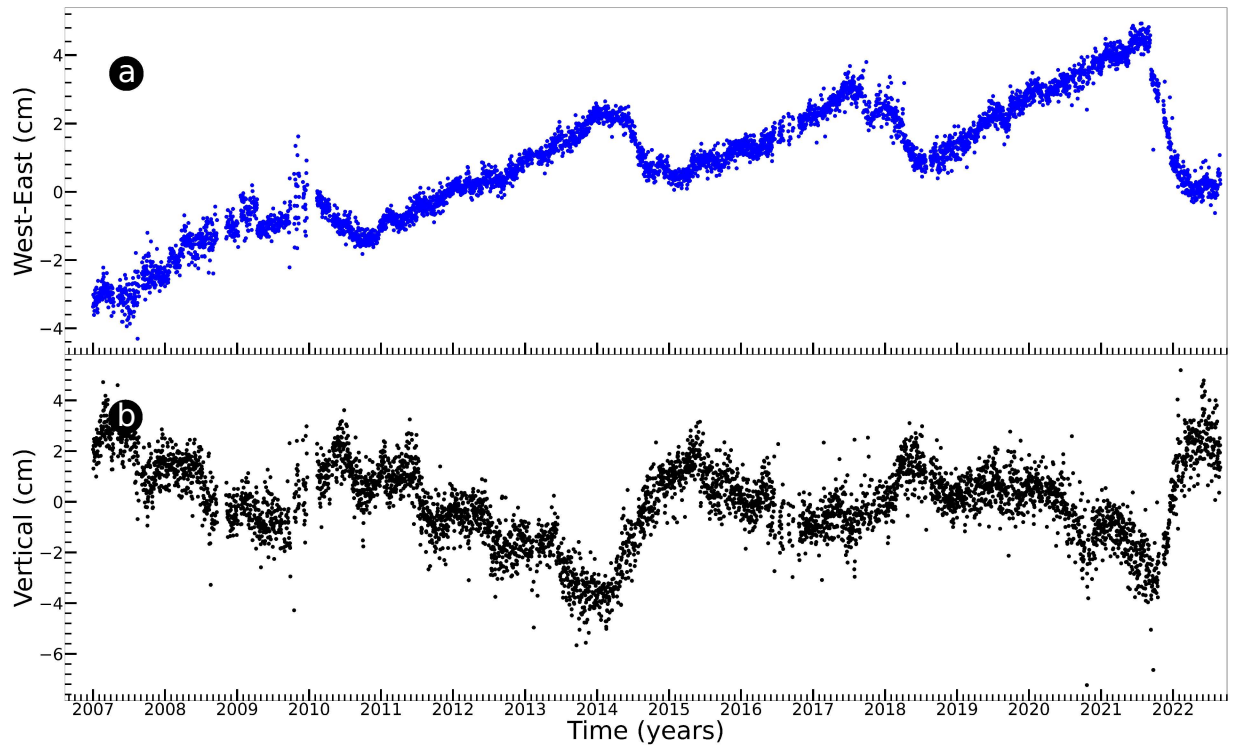


Figure B.1. GPS displacement of the CAYA station. The GPS vertical sensor records the “true ground displacement” during a SSE cycle. Although, west-east displacement signal is clearer than the vertical displacement signal. This is why in studies of slow earthquakes, it is preferred to show horizontal GPS records because vertical records are more susceptible to seasonal phenomena. Source: LAGEOS (2014).

APPENDIX C. EARTH STRUCTURE

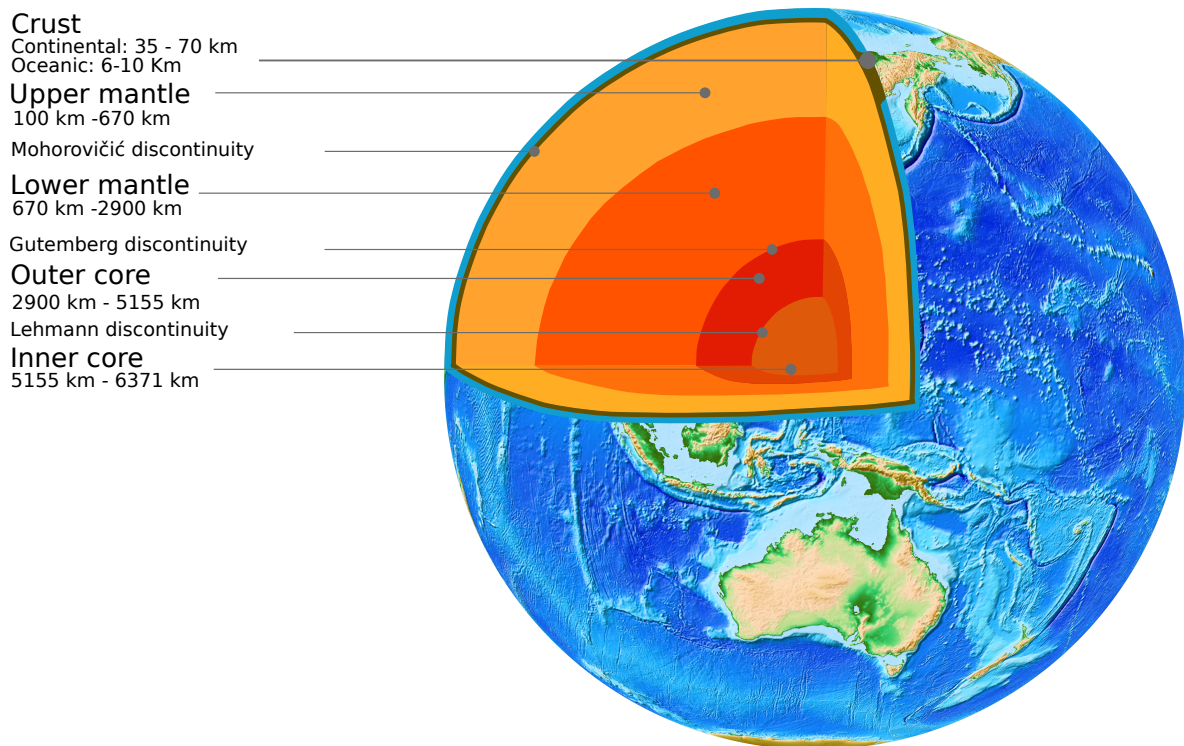


Figure C.1. Diagram of the internal structure of the Earth. Source: Van der Pluijm and Marshak (2004).

APPENDIX D. SEA SURFACE TEMPERATURE ANOMALIES OF 1997 AND 1999

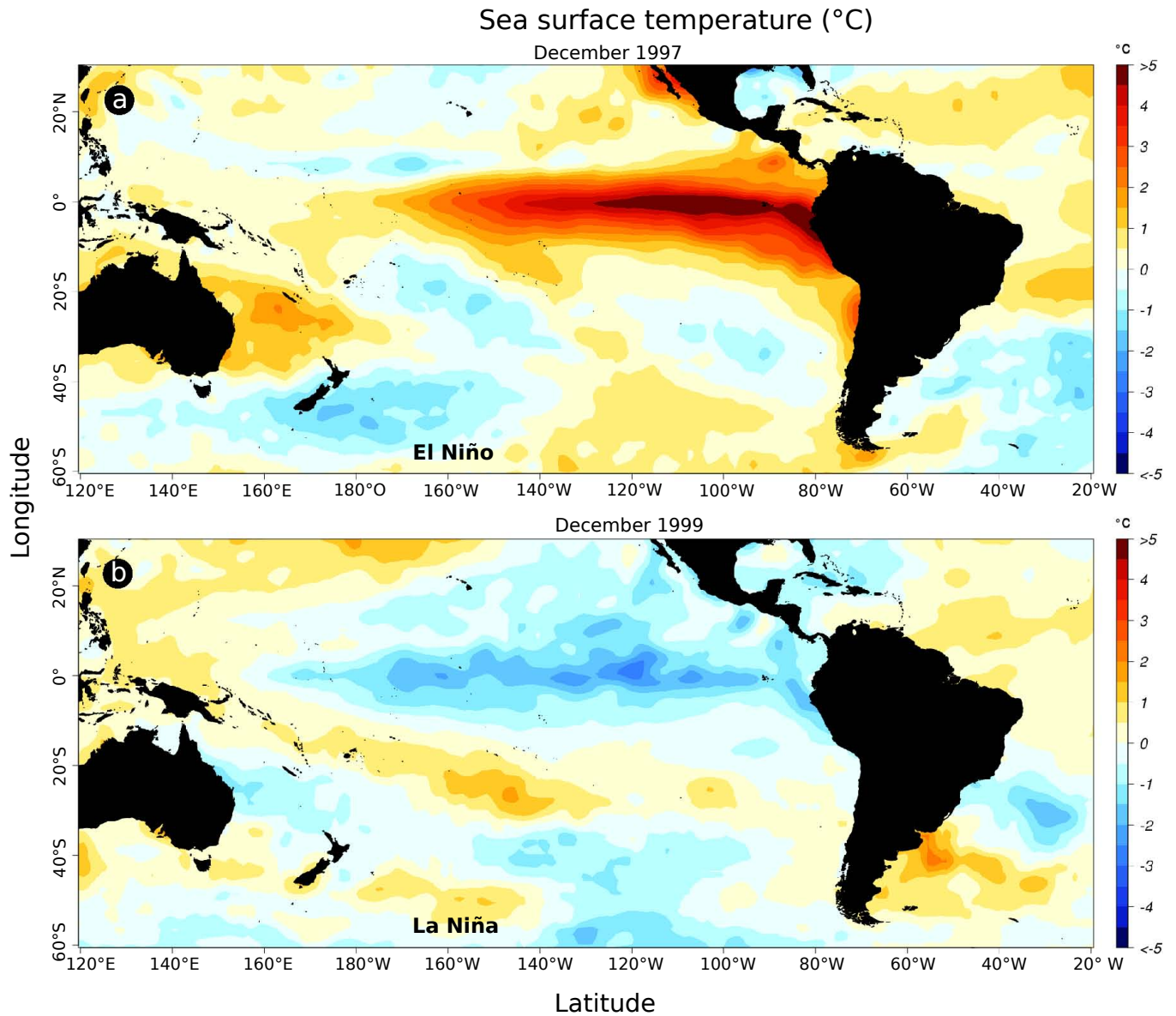


Figure D.1. Map of sea surface temperature anomalies. The warm phase correspond to an (a) El Niño event, while the cold phase to (b) La Niña. Adapted from CIFEN (2022).

APPENDIX E. SAFFIR-SIMPSON SCALE

Table E.1. Classification of tropical cyclones.

Storm category	Wind speed (km/h)	Central low pressure (millibar)
Tropical depression ¹	$61 \leq$	
Tropical storm ¹	63-117	
Category 1	119-153	≥ 980
Category 2	155-177	965-979
Category 3	178-208	945-964
Category 4	209-251	920-944
Category 5	≥ 252	920 <

Adapted from Paul and Rashid (2017).

¹ Although the formative nature of a depression and tropical storm precede a hurricane, they are not part of the Saffir-Simpson scale for hurricanes.

APPENDIX F. PRINCIPAL TIDAL CONSTITUENTS

Table F.1. Principal tidal constituents

Name	Symbol	Period (hours)
Higher harmonics		
Shallow water overtides of principal lunar	M_4	6.210300601
Shallow water overtides of principal lunar	M_6	4.140200401
Shallow water terdiurnal	Mk_3	8.177140247
Shallow water overtides of principal solar	S_4	6
Shallow water quarter diurnal	MN_4	6.269173724
Shallow water overtides of principal solar	S_6	4
Lunar terdiurnal	M_3	8.280400802
Shallow water terdiurnal	$2''MK_3$	8.38630265
Shallow water eighth diurnal	M_8	3.105150301
Shallow water quarter diurnal	MS_4	6.103339275
Semi-diurnal		
Principal lunar semidiurnal	M_2	12.4206012
Principal solar semidiurnal	S_2	12
Larger lunar elliptic semidiurnal	N_2	12.65834751
Larger lunar evectional	ν_2	12.62600509
Variational	MU_2	12.8717576
Lunar elliptical semidiurnal second-order	$2''N_2$	12.90537297
Smaller lunar evectional	λ_2	12.22177348
Larger solar elliptic	T_2	12.01644934
Smaller solar elliptic	R_2	11.98359564
Shallow water semidiurnal	$2SM_2$	11.60695157
Smaller lunar elliptic semidiurnal	L_2	12.19162085
Lunisolar semidiurnal	K_2	11.96723606

Table F.1 Continue

Diurnal		
Lunar diurnal	K_1	23.93447213
Lunar diurnal	O_1	25.81933871
Lunar diurnal	OO_1	22.30608083
Solar diurnal	S_1	24
Smaller lunar elliptic diurnal	M_1	24.84120241
Smaller lunar elliptic diurnal	J_1	23.09848146
Larger lunar evectional diurnal	ρ	26.72305326
Larger lunar elliptic diurnal	Q_1	26.86835
Larger elliptic diurnal	$2Q_1$	28.00621204
Solar diurnal	P_1	24.06588766
Long period		
Lunar monthly	M_m	661.3111655
Solar semiannual	S_{sa}	4383.076325
Solar annual	S_a	8766.15265
Lunisolar synodic fortnightly	M_{sf}	354.3670666
Lunisolar fortnightly	M_f	327.8599387

APPENDIX G. TEMPERATURE-CORRECTED BOTTOM PRESSURE RECORDS

To correct the bottom pressure data, we first performed a linear robust fit using the Huber function with the pressure and temperature data (Figure G.1). This robust regression model reduces the effects of outliers.

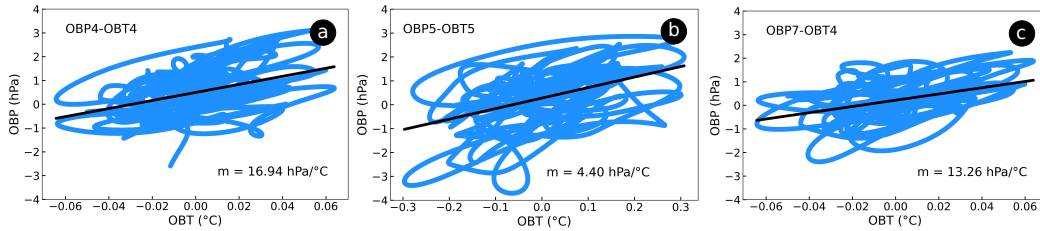


Figure G.1. Scatter plots of the filtered seafloor pressure and temperature signals. Before performing robust linear regression, the seafloor temperature signals were lagged by (a) -18, (b) -7, and (c) -19 days.

Then, we calculated the seafloor temperature contribution to the pressure by multiplying the temperature measurements by the slope (hPa/°C) of the robust regression. In this way, a temperature-derived pressure time series was obtained for each site (Figure G.2). Temperature-dependent fluctuations were corrected by subtracting the temperature-derived pressure time series from the filtered pressure signals (Figure G.2). Finally, we applied the reference site method (Figure G.3).

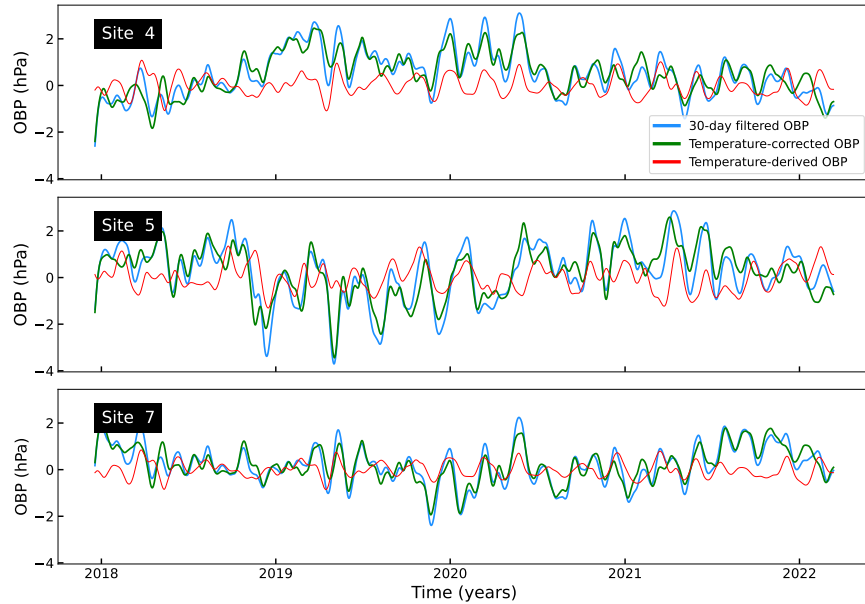


Figure G.2. Temperature-corrected seafloor pressure measurements.

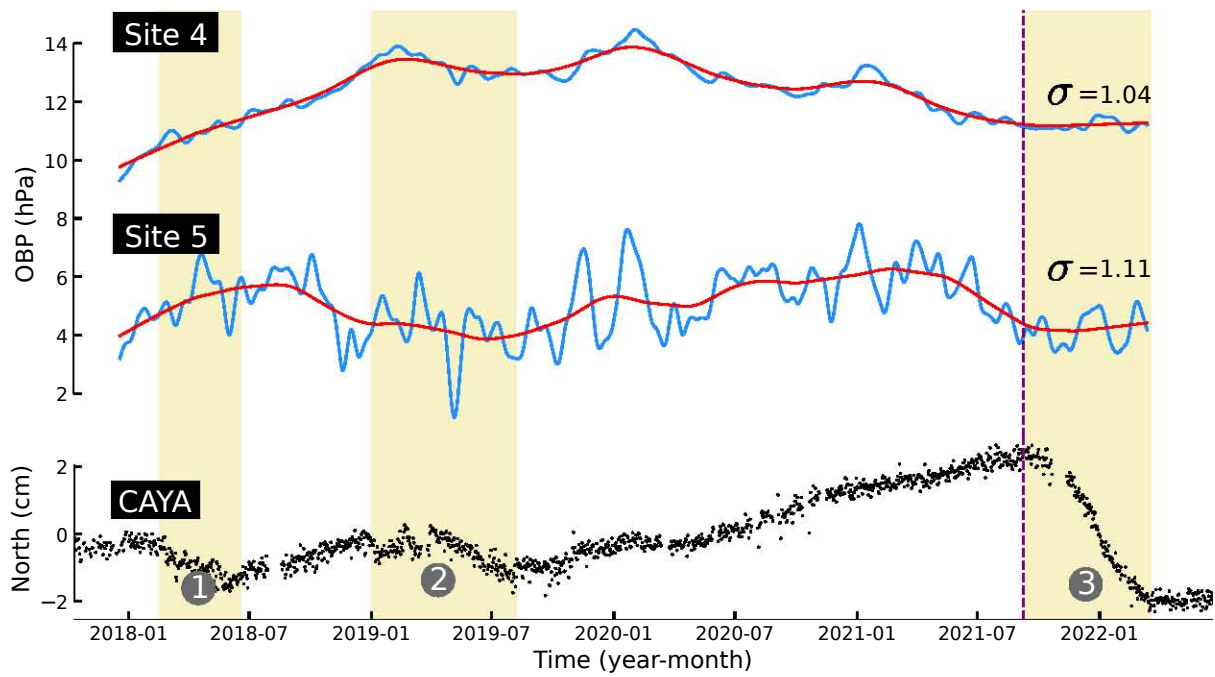


Figure G.3. Temperature-corrected filtered OBP signals after applying the reference-site method did not significantly reduce residual data variability. It is evident that these signals are similar to those in Figures 5.1 and 5.2. LOESS smoothing was applied with a window parameter of $f_L = 0.15$.

APPENDIX H. INTENSITY CLASSIFICATION OF EL NIÑO AND LA NIÑA EVENTS

Table H.1. Intensity classification of El Niño and La Niña events. Based on Oceanic Niño Index (ONI).

El Niño				La Niña		
Weak	Moderate	Strong	Very strong	Weak	Moderate	Strong
1952-53	1951-52	1957-58	1982-83	1954-55	1955-56	1973-74
1953-54	1963-64	1965-66	1997-98	1964-65	1970-71	1975-76
1958-59	1968-69	1972-73	2015-16	1971-72	1995-96	1988-89
1969-70	1986-87	1987-88		1974-75	2011-12	1998-99
1976-77	1994-95	1991-92		1983-84	2020-21	1999-00
1977-78	2002-03	2023-24		1984-85	2021-22	2007-08
1979-80	2009-10			2000-01		2010-11
2004-05				2005-06		
2006-07				2008-09		
2014-15				2016-17		
2018-19				2017-18		
				2022-23		

Source: Null (2024).

REFERENCES

- Anderson, D.L., Ben-Menahem, A., Archambeau, C.B., 1965. Attenuation of seismic energy in the upper mantle. *Journal of Geophysical Research* 70, 1441–1448. <https://doi.org/10.1029/JZ070i006p01441>.
- Atwater, B.F., Cisternas V., M., Bourgeois, J., Dudley, W., Hendley, J.W., Stauffer, P.H., 2001. *Sobreviviendo a un tsunami: lecciones de Chile, Hawaii, y Japón*. volume 1218. Departamento del Interior de los EE. UU., Servicio Geológico de los EE. UU.
- Aucan, J., Merrifield, M.A., Luther, D.S., Flament, P., 2006. Tidal mixing events on the deep flanks of Kaena ridge, Hawaii. *Journal of Physical Oceanography* 36, 1202–1219.
- Baba, T., Hirata, K., Hori, T., Sakaguchi, H., 2006. Offshore geodetic data conducive to the estimation of the afterslip distribution following the 2003 Tokachi-oki earthquake. *Earth and Planetary Science Letters* 241, 281–292.
- Bath, M., 2013. *Introduction to seismology*. volume 27. Birkhäuser.
- Ben-Menahem, A., Singh, S.J., 2012. *Seismic waves and sources*. Springer Science & Business Media. ISBN:978-1-4612-5858-2.
- Beroza, G.C., Jordan, T.H., 1990. Searching for slow and silent earthquakes using free oscillations. *Journal of Geophysical Research: Solid Earth* 95, 2485–2510. <https://doi.org/10.1029/JB095iB03p02485>.
- Bjerknes, J., 1969. Atmospheric teleconnections from the equatorial pacific. *Monthly weather review* 97, 163–172. [http://doi.org/10.1175/1520-0493\(1969\)097<0163:ATFTEP>2.3.CO;2](http://doi.org/10.1175/1520-0493(1969)097<0163:ATFTEP>2.3.CO;2).
- Björnsson, H., Venegas, S., 1997. A manual for EOF and SVD analyses of climatic data. *CCGCR Report* 97, 112–134.
- Bletery, Q., Nocquet, J.M., 2020. Slip bursts during coalescence of slow slip events in cascadia. *Nature communications* 11, 1–6. <https://doi.org/10.1038/s41467-020-15494-4>.
- Boore, D.M., 1989. The Richter scale: its development and use for determining earthquake source parameters. *Tectonophysics* 166, 1–14.
- Brace, W., Byerlee, J.D., 1966. Recent experimental studies of brittle fracture of rocks, in: *The 8th US Symposium on Rock Mechanics (USRMS)*, OnePetro.
- Brush, S.G., 1980. Discovery of the Earth's core. *American Journal of Physics* 48, 705–724. <https://doi.org/10.1119/1.12026>.
- Calmant, S., Crétaux, J.F., Rémy, F., 2016. Chapter 4: Principles of radar satellite altimetry for application on inland waters, in: *Microwave Remote Sensing of Land Surface*. Elsevier, pp. 175–218. <https://doi.org/10.1016/B978-1-78548-159-8.50004-9>.
- Cane, M.A., 1983. Oceanographic events during El Niño. *Science* 222, 1189–1195. <http://doi.org/10.1126/science.222.4629.1189>.
- Centro Internacional para la Investigación del Fenómeno de El Niño (CIIFEN), 2022. *El Niño Oscilación del Sur*. <http://ciifen.org/>.
- Cervelli, P., Segall, P., Johnson, K., Lisowski, M., Miklius, A., 2002. Sudden aseismic fault slip on the south flank of Kilauea volcano. *Nature* 415, 1014–1018. <https://doi.org/10.1038/4151014a>.
- Chapple, W.M., Forsyth, D.W., 1979. Earthquakes and bending of plates at trenches. *Journal of Geophysical Research: Solid Earth* 84, 6729–6749.
- Chelton, D.B., 2024. Personal communication. Oregon State University.

- Chelton, D.B., Ries, J.C., Haines, B.J., Fu, L.L., Callahan, P.S., 2001. Chapter 1 satellite altimetry, in: Fu, L.L., Cazenave, A. (Eds.), *Satellite Altimetry and Earth Sciences: a handbook of techniques and applications*. Academic Press. volume 69 of *International Geophysics*, pp. 1–122. [https://doi.org/10.1016/S0074-6142\(01\)80146-7](https://doi.org/10.1016/S0074-6142(01)80146-7).
- Chierici, F., Iannaccone, G., Pignagnoli, L., Guardato, S., Locritani, M., Embriaco, D., Donnarumma, G.P., Rodgers, M., Malservisi, R., Beranzoli, L., 2016. A new method to assess long-term sea-bottom vertical displacement in shallow water using a bottom pressure sensor: Application to Campi Flegrei, southern Italy. *Journal of Geophysical Research: Solid Earth* 121, 7775–7789.
- Collar, P., Cartwright, D., 1972. Open sea tidal measurements near the edge of the northwest European continental shelf, in: *Deep Sea Research and Oceanographic Abstracts*, Elsevier. pp. 673–689. [https://doi.org/10.1016/0011-7471\(72\)90060-5](https://doi.org/10.1016/0011-7471(72)90060-5).
- Cruz-Atienza, V.M., 2024. Personal communication. Instituto de Geofísica, Universidad Nacional Autónoma de México.
- Cruz-Atienza, V.M., Ito, Y., Kostoglodov, V., Hjörleifsdóttir, V., Iglesias, A., Tago, J., Calò, M., Real, J., Husker, A., Ide, S., et al., 2018. A seismogeodetic amphibious network in the Guerrero seismic gap, Mexico. *Seismological Research Letters* 89, 1435–1449. <https://doi.org/10.1785/0220170173>.
- Cruz-Atienza, V.M., Tago, J., Villafuerte, C., Wei, M., Garza-Girón, R., Dominguez, L.A., Kostoglodov, V., Nishimura, T., Franco, S., Real, J., et al., 2021. Short-term interaction between silent and devastating earthquakes in Mexico. *Nature communications* 12, 1–14. <https://doi.org/10.1038/s41467-021-22326-6>.
- Das, S., Henry, C., 2003. Spatial relation between main earthquake slip and its aftershock distribution. *Reviews of Geophysics* 41. <https://doi.org/10.1029/2002RG000119>.
- Das, S., Kostrov, B., 1983. Breaking of a single asperity: Rupture process and seismic radiation. *Journal of Geophysical Research: Solid Earth* 88, 4277–4288.
- DeMets, C., Gordon, R.G., Argus, D.F., 2010. Geologically current plate motions. *Geophysical journal international* 181, 1–80.
- DeMets, C., Traylen, S., 2000. Motion of the Rivera plate since 10 ma relative to the Pacific and North American plates and the mantle. *Tectonophysics* 318, 119–159.
- Departamento de Sismología, Instituto de Geofísica (IG), Universidad Nacional Autónoma de México, México., 2023. <http://www.geofisica.unam.mx/>.
- Devine, P., 2000. Radar level measurement: the user’s guide. Vega Controls Burgess Hill, UK.
- Dirección General Adjunta de Oceanografía, Hidrografía y Meteorología (DIGAOHM), Secretaría de Marina Armada de México (SEMAR), 2023. <http://digaohm.semar.gob.mx>.
- Dragert, H., Wang, K., James, T.S., 2001. A silent slip event on the deeper Cascadia subduction interface. *Science* 292, 1525–1528. <https://doi.org/10.1126/science.106015>.
- Dragert, H., Wang, K., Rogers, G., 2004. Geodetic and seismic signatures of episodic tremor and slip in the northern Cascadia subduction zone. *Earth, planets and space* 56, 1143–1150. <https://doi.org/10.1186/BF03353333>.
- Eaton, J.P., Richter, D.H., Ault, W.U., 1961. The tsunami of May 23, 1960, on the Island of Hawaii. *Bulletin of the Seismological Society of America* 51, 135–157. <https://doi.org/10.1785/BSSA0510020135>.
- Emery, K.O., Aubrey, D.G., 1991. Sea levels, land levels, and tide gauges. Springer Science & Business Media. <https://doi.org/10.1007/978-1-4613-9101-2>.
- Enfield, D.B., Allen, J., 1980. On the structure and dynamics of monthly mean sea level anomalies along the Pacific coast of North and South America. *Journal of Physical Oceanography* 10, 557–578. [http://doi.org/10.1175/1520-0485\(1980\)010<0557:OTSADO>2.0.CO;2](http://doi.org/10.1175/1520-0485(1980)010<0557:OTSADO>2.0.CO;2).

- European Space Agency (ESA), 2018. Satellite radar altimetry: past and future. <https://earth.esa.int/eogateway/news/satellite-radar-altimetry-past-and-future>.
- Ewing, J., Ewing, M., 1959. Seismic-refraction measurements in the Atlantic Ocean basins, in the Mediterranean Sea, on the Mid-Atlantic Ridge, and in the Norwegian Sea. *Geological Society of America Bulletin* 70, 291–318. [https://doi.org/10.1130/0016-7606\(1959\)70\[291:SMITAO\]2.0.CO;2](https://doi.org/10.1130/0016-7606(1959)70[291:SMITAO]2.0.CO;2).
- Farsangi, E.N., 2021. *Natural Hazards: Impacts, Adjustments and Resilience*. BoD–Books on Demand.
- Fedotov, S., 1965. Regularities of the distribution of strong earthquakes in Kamchatka, the Kuril Islands, and northeastern Japan. *Tr. Inst. Phys. Earth Acad. Sci. USSR* 36, 66–93.
- Fernandes, M.J., Lázaro, C., Nunes, A.L., Scharroo, R., 2014. Atmospheric corrections for altimetry studies over inland water. *Remote Sensing* 6, 4952–4997. <https://doi.org/10.3390/rs6064952>.
- Filloux, J., 1982. Tsunami recorded on the open ocean floor. *Geophysical Research Letters* 9, 25–28. <https://doi.org/10.1029/GL009i001p00025>.
- Filloux, J.H., 1971. Deep-sea tide observations from the northeastern Pacific, in: *Deep Sea Research and Oceanographic Abstracts*, Elsevier. pp. 275–284. [https://doi.org/10.1016/0011-7471\(71\)90118-5](https://doi.org/10.1016/0011-7471(71)90118-5).
- Fowler, C.M.R., Fowler, C.M.R., Fowler, M., 1990. *The solid earth: an introduction to global geophysics*. Cambridge University Press.
- Frank, W.B., Brodsky, E.E., 2019. Daily measurement of slow slip from low-frequency earthquakes is consistent with ordinary earthquake scaling. *Science advances* 5, eaaw9386.
- Fredrickson, E.K., Wilcock, W.S., Schmidt, D.A., MacCready, P., Roland, E., Kurapov, A.L., Zumberge, M.A., Sasagawa, G.S., 2019. Optimizing sensor configurations for the detection of slow-slip earthquakes in seafloor pressure records, using the Cascadia subduction zone as a case study. *Journal of Geophysical Research: Solid Earth* 124, 13504–13531.
- Fujii, N., Kumazawa, M., 2010. Chapter 5 : Detection of Transient Phenomena Due to Active Scatterers, in: *Active Geophysical Monitoring*. Pergamon. volume 40 of *Handbook of Geophysical Exploration: Seismic Exploration*, pp. 93–103. [https://doi.org/10.1016/S0950-1401\(10\)04010-3](https://doi.org/10.1016/S0950-1401(10)04010-3).
- Garabato, A.C.N., Polzin, K.L., King, B.A., Heywood, K.J., Visbeck, M., 2004. Widespread intense turbulent mixing in the southern ocean. *Science* 303, 210–213.
- Garrett, C., Kunze, E., 2007. Internal tide generation in the deep ocean. *Annu. Rev. Fluid Mech.* 39, 57–87.
- Gilbert, G., 1884. A theory of the earthquakes of the great basin, with a practical application. *American Journal of Science (1880-1910)* 27, 49. <https://doi.org/10.2475/ajs.s3-27.157.49>.
- Gomberg, J., 2007, C., Group, B.W., 2010. Slow-slip phenomena in Cascadia from 2007 and beyond: A review. *Bulletin* 122, 963–978.
- Gomberg, J., Hautala, S., Johnson, P., Chiswell, S., 2019. Separating sea and slow slip signals on the seafloor. *Journal of Geophysical Research: Solid Earth* 124, 13486–13503.
- Grantz, A., Plafker, G., Kachadoorian, R., 1964. Alaska’s Good Friday earthquake, March 27, 1964: a preliminary geologic evaluation. volume 491. US Department of the Interior, Geological Survey.
- Grgić, M., Bašić, T., 2021. Radar satellite altimetry in geodesy-theory, applications and recent developments, in: *Geodetic Sciences-Theory, Applications and Recent Developments*. IntechOpen.
- Grotzinger, J., Jordan, T.H., Press, F., 2010. *Understanding earth*. Macmillan.
- Hallam, A., 1975. Alfred Wegener and the hypothesis of continental drift. *Scientific American* 232, 88–97.

- Hanks, T.C., Kanamori, H., 1979. A moment magnitude scale. *Journal of Geophysical Research: Solid Earth* 84, 2348–2350. <https://doi.org/10.1029/JB084iB05p02348>.
- Hannah, J., 2011. The difficulties in using tide gauges to monitor long-term sea level change. *Survey Quarterly* 300, 19.
- Havskov, J., Ottemoller, L., 2010. *Routine data processing in earthquake seismology: with sample data, exercises and software*. Springer Science & Business Media.
- Heaps, N., 1983. Storm surges, 1967–1982. *Geophysical Journal International* 74, 331–376. <https://doi.org/10.1111/j.1365-246X.1983.tb01883.x>.
- Heidarzadeh, M., Gusman, A.R., Ishibe, T., Sabeti, R., Šepić, J., 2022. Estimating the eruption-induced water displacement source of the 15 January 2022 Tonga volcanic tsunami from tsunami spectra and numerical modelling. *Ocean Engineering* 261, 112165.
- Hess, H., 1962. History of ocean basins <https://doi.org/10.1130/Petrologic.1962.599>.
- Hirose, H., Hirahara, K., Kimata, F., Fujii, N., Miyazaki, S., 1999. A slow thrust slip event following the two 1996 hyuganada earthquakes beneath the Bungo Channel, southwest Japan. *Geophysical Research Letters* 26, 3237–3240. <https://doi.org/10.1029/1999GL010999>.
- Hirose, H., Obara, K., 2005. Repeating short-and long-term slow slip events with deep tremor activity around the bungo channel region, southwest japan. *Earth, planets and space* 57, 961–972.
- Holmes, A., 1931. Radioactivity and earth movements. *Transactions of the Geological Society of Glasgow* 18, 559–606.
- Hu, G., Li, L., Ren, Z., Zhang, K., 2023. The characteristics of the 2022 Tonga volcanic tsunami in the Pacific Ocean. *Natural hazards and earth system sciences* 23, 675–691.
- Hyndman, R.D., Yamano, M., Oleskevich, D.A., 1997. The seismogenic zone of subduction thrust faults. *Island Arc* 6, 244–260. <https://doi.org/10.1111/j.1440-1738.1997.tb00175.x>.
- Iglesias, A., Singh, S.K., Castro-Artola, O., Pérez-Campos, X., Corona-Fernandez, R.D., Santoyo, M.A., Espíndola, V.H., Arroyo, D., Franco, S.I., 2022. A source study of the M w 7.0 Acapulco, Mexico, earthquake of 8 September 2021. *Seismological Society of America* 93, 3205–3218.
- Inazu, D., Hino, R., 2011. Temperature correction and usefulness of ocean bottom pressure data from cabled seafloor observatories around Japan for analyses of tsunamis, ocean tides, and low-frequency geophysical phenomena. *Earth, planets and space* 63, 1133–1149.
- Inoue, T., Ito, Y., Wallace, L.M., Yoshikawa, Y., Inazu, D., Garcia, E.S.M., Muramoto, T., Webb, S.C., Ohta, K., Suzuki, S., et al., 2021. Water depth dependence of long-range correlation in nontidal variations in seafloor pressure. *Geophysical Research Letters* 48, e2020GL092173.
- Intergovernmental Oceanographic Commission (IOC), 2006. *Manual on sea level measurement and interpretation. Volume IV: An update to 2006*.
- Isacks, B., Oliver, J., Sykes, L.R., 1968. Seismology and the new global tectonics. *Journal of geophysical research* 73, 5855–5899. <https://doi.org/10.1029/JB073i018p05855>.
- Ito, Y., Hino, R., Kido, M., Fujimoto, H., Osada, Y., Inazu, D., Ohta, Y., Inuma, T., Ohzono, M., Miura, S., 2013. Episodic slow slip events in the Japan subduction zone before the 2011 Tohoku-oki earthquake. *Tectonophysics* 600, 14–26. <https://doi.org/10.1016/j.tecto.2012.08.022>.
- Itoh, Y., Nishimura, T., Ariyoshi, K., Matsumoto, H., 2019. Interplate slip following the 2003 Tokachi-oki earthquake from ocean bottom pressure gauge and land GNSS data. *Journal of Geophysical Research: Solid Earth* 124, 4205–4230.
- Jaupart, C., Mareschal, J.C., 2010. *Heat generation and transport in the Earth*. Cambridge university press.

- Jones, L.M., Molnar, P., 1979. Some characteristics of foreshocks and their possible relationship to earthquake prediction and premonitory slip on faults. *Journal of Geophysical Research: Solid Earth* 84, 3596–3608. <https://doi.org/10.1029/JB084iB07p03596>.
- Kato, A., Obara, K., Igarashi, T., Tsuruoka, H., Nakagawa, S., Hirata, N., 2012. Propagation of slow slip leading up to the 2011 Mw 9.0 Tohoku-Oki earthquake. *Science* 335, 705–708. <https://doi.org/10.1126/science.1215141>.
- Kim, Y., Clayton, R., Jackson, J., 2010. Geometry and seismic properties of the subducting Cocos plate in central Mexico. *Journal of Geophysical Research: Solid Earth* 115.
- Kious, W.J., Tilling, R.I., 1996. *This dynamic Earth: the story of plate tectonics*. DIANE Publishing. <https://doi.org/10.3133/7000097>.
- Kostoglodov, V., Husker, A., Shapiro, N.M., Payero, J.S., Campillo, M., Cotte, N., Clayton, R., 2010. The 2006 slow slip event and nonvolcanic tremor in the Mexican subduction zone. *Geophysical Research Letters* 37.
- Kostoglodov, V., Pacheco, J., 1999. *Cien años de sismicidad en México*. Instituto de Geofísica .
- Kulháněk, O., 2012. *Anatomy of Seismograms: For the IASPEI/Unesco Working Group on Manual of Seismogram Interpretation*. Elsevier.
- Kuznetsov, V., Sinelnikov, V., Alpert, S., 2015. Yakov Alpert: Sputnik-1 and the first satellite ionospheric experiment. *Advances in Space Research* 55, 2833–2839. <https://doi.org/10.1016/j.asr.2015.02.033>.
- LaBonte, A.L., Brown, K.M., Fialko, Y., 2009. Hydrologic detection and finite element modeling of a slow slip event in the Costa Rica prism toe. *Journal of Geophysical Research: Solid Earth* 114. <https://doi.org/10.1029/2008JB005806>.
- Laboratorio de Geodesia Espacial (LaGeos), Universidad Nacional Autónoma México, Instituto de Geofísica, México, 2023. <http://lageos.geofisica.unam.mx>.
- Lay, T., Wallace, T.C., 1995. *Modern global seismology*. Elsevier.
- Linde, A.T., Gladwin, M.T., Johnston, M.J., Gwyther, R.L., Bilham, R.G., 1996. A slow earthquake sequence on the San Andreas fault. *Nature* 383, 65–68. <https://doi.org/10.1038/383065a0>.
- Lisitzin, E., 1974. *Sea-level changes*. volume 8. Elsevier Oceanography Series.
- Lonsdale, P., 2005. Creation of the Cocos and Nazca plates by fission of the Farallon plate. *Tectonophysics* 404, 237–264.
- Lundquist, C.A., 1970. *Application of space techniques to solid-earth and ocean physics*. Technical Report.
- MacKinnon, J., 2013. Mountain waves in the deep ocean. *Nature* 501, 321–322.
- Matsumoto, H., Araki, E., 2021. Drift characteristics of DONET pressure sensors determined from in-situ and experimental measurements. *Frontiers in Earth Science* 8, 600966.
- Matthäus, W., 1970. Zur historischen Entwicklung der Methoden und Geräte zur Beobachtung und Registrierung des Wasserstandes. *Schriftenr. Geschichte Naturwiss., Technik u. Medizin* 7, 46–59.
- Matthäus, W., 1972. On the history of recording tide gauges. *Proceedings of the Royal Society of Edinburgh. Section B. Biology* 73, 26–34. <https://doi.org/10.1017/S0080455X00002083>.
- Mescherikov, J., 1968. Recent crustal movements in seismic regions: geodetic and geomorphic data. *Tectonophysics* 6, 29–39. [https://doi.org/10.1016/0040-1951\(68\)90024-3](https://doi.org/10.1016/0040-1951(68)90024-3).
- Munk, W., 1981. Internal waves and small-scale processes. *Evolution of Physical Oceanography: Scientific Surveys in Honor of Henry Stommel*, BA Warren and C. Wunsch, Eds.

- Muramoto, T., Ito, Y., Inazu, D., Wallace, L.M., Hino, R., Suzuki, S., Webb, S.C., Henrys, S., 2019. Seafloor crustal deformation on ocean bottom pressure records with nontidal variability corrections: Application to Hikurangi margin, New Zealand. *Geophysical Research Letters* 46, 303–310.
- Nakamura, Y., Kodaira, S., Fujie, G., Yamashita, M., Obana, K., Miura, S., 2023. Incoming plate structure at the Japan Trench subduction zone revealed in densely spaced reflection seismic profiles. *Progress in Earth and Planetary Science* 10, 45.
- National Oceanic and Atmospheric Administration (NOAA), United States, 2023. <http://nctr.pmel.noaa.gov>.
- Neubauer, F., 2014. The structure of the Eastern Alps: from Eduard Suess to present-day knowledge. *Austrian Journal of Earth Sciences* 107, 83–93.
- Newkirk, R.W., Ertel, I.D., 1977. Skylab: A chronology. volume 4011. NASA, National Aeronautics and Space Administration.
- Niiler, P., Filloux, J., Liu, W., Samelson, R.M., Paduan, J., Paulson, C., 1993. Wind-forced variability of the deep eastern North Pacific: Observations of seafloor pressure and abyssal currents. *Journal of Geophysical Research: Oceans* 98, 22589–22602.
- Nikurashin, M., Ferrari, R., 2013. Overturning circulation driven by breaking internal waves in the deep ocean. *Geophysical Research Letters* 40, 3133–3137.
- Nishenko, S., Singh, S., 1987. Conditional probabilities for the recurrence of large and great interplate earthquakes along the Mexican subduction zone. *Bulletin of the Seismological Society of America* 77, 2095–2114. <https://doi.org/10.1785/BSSA0770062095>.
- Null, J., 2024. El Niño and La Niña Years and Intensities. <https://ggweather.com/enso/oni.htm>. Accessed: 2022-07-20.
- Oliver, J., Isacks, B., 1967. Deep earthquake zones, anomalous structures in the upper mantle, and the lithosphere. *Journal of Geophysical Research* 72, 4259–4275. <https://doi.org/10.1029/JZ072i016p04259>.
- Oregon State University (OSU), 2021. Volcano world. <http://www.oregonstate.edu>.
- Organización Meteorológica Mundial (OMM), 2014. El Niño/ Oscilación del Sur. OMM-N° 1145.ISBN:978-92-63-31145-0.
- Ortiz, M., Singh, S.K., Kostoglodov, V., Pacheco, J., 2000. Source areas of the Acapulco-San Marcos, Mexico earthquakes of 1962 (M 7.1; 7.0) and 1957 (M 7.7), as constrained by tsunami and uplift records. *Geofísica Internacional* 39, 337–348.
- Pardo, M., Suárez, G., 1995. Shape of the subducted Rivera and Cocos plates in southern Mexico: Seismic and tectonic implications. *Journal of Geophysical Research: Solid Earth* 100, 12357–12373.
- Paul, B., Rashid, H., 2017. Climatic hazards in coastal Bangladesh: non-structural and structural solutions. Butterworth-Heinemann. ISBN: 9780128052761.
- Pawlowicz, R., Beardsley, B., Lentz, S., 2002. Classical tidal harmonic analysis including error estimates in MATLAB using T_TIDE. *Computers & Geosciences* 28, 929–937. [https://doi.org/10.1016/S0098-3004\(02\)00013-4](https://doi.org/10.1016/S0098-3004(02)00013-4).
- Pelinovsky, E., Choi, B., Stromkov, A., Didenkulova, I., Kim, H.S., 2005. Analysis of tide-gauge records of the 1883 Krakatau tsunami, in: *Tsunamis: case studies and recent developments*. Springer, pp. 57–77.
- Permanent Service for Mean Sea Level (PSMSL), National Oceanography Centre, United Kingdom, 2023. <http://www.psmsl.org>.
- Petterson, H., 1925. Method of Measuring Deep Sea Tides. *Nature* 115, 639–639. <https://doi.org/10.1038/115639a0>.

- Plata-Martínez, R., Ide, S., Shinohara, M., Garcia, E., Mizuno, N., Dominguez, L., Taira, T., Yamashita, Y., Toh, A., Yamada, T., et al., 2021. Shallow slow earthquakes to decipher future catastrophic earthquakes in the Guerrero seismic gap. *Nature communications* 12, 1–8. <https://doi.org/10.1038/s41467-021-24210-9>.
- Van der Pluijm, B.A., Marshak, S., 2004. *Earth structure*. New York .
- Polster, A., Fabian, M., Villinger, H., 2009. Effective resolution and drift of Paroscientific pressure sensors derived from long-term seafloor measurements. *Geochemistry, Geophysics, Geosystems* 10.
- Pugh, D., Woodworth, P., 2014. *Sea-level science: understanding tides, surges, tsunamis and mean sea-level changes*. Cambridge University Press.
- Pugh, D.T., 1996. *Tides, surges and mean sea-level* .
- Rabinovich, A.B., 1997. Spectral analysis of tsunami waves: Separation of source and topography effects. *Journal of Geophysical Research: Oceans* 102, 12663–12676.
- Rabinovich, A.B., Thomson, R.E., Fine, I.V., 2013. The 2010 Chilean tsunami off the west coast of Canada and the northwest coast of the United States. *Pure and Applied Geophysics* 170, 1529–1565.
- Radiguet, M., Cotton, F., Vergnolle, M., Campillo, M., Walpersdorf, A., Cotte, N., Kostoglodov, V., 2012. Slow slip events and strain accumulation in the Guerrero gap, Mexico. *Journal of Geophysical Research: Solid Earth* 117. <https://doi.org/10.1029/2011JB008801>.
- Ranero, C.R., Phipps Morgan, J., McIntosh, K., Reichert, C., 2003. Bending-related faulting and mantle serpentinization at the Middle America trench. *Nature* 425, 367–373.
- Reid, H.F., 1911. The elastic-rebound theory of earthquakes. University of California Publications, *Bulletin of the Department of Geology* 6, 413–444. <https://doi.org/10.1785/BSSA0020010098>.
- Richter, C.F., 1935. An instrumental earthquake magnitude scale. *Bulletin of the seismological society of America* 25, 1–32. <https://doi.org/10.1785/BSSA0250010001>.
- Rogers, G., Dragert, H., 2003. Episodic tremor and slip on the Cascadia subduction zone: The chatter of silent slip. *Science* 300, 1942–1943.
- Ross, J.C., 1854. On the effect of the pressure of the atmosphere on the mean level of the ocean. *Philosophical Transactions of the Royal Society of London* , 285–296 <https://doi.org/10.1098/rstl.1854.0013>.
- Rousset, B., 2019. Months-long subduction slow slip events avoid the stress shadows of seismic asperities. *Journal of Geophysical Research: Solid Earth* 124, 7227–7230.
- Ryan, W.B., Carbotte, S.M., Coplan, J.O., O’Hara, S., Melkonian, A., Arko, R., Weissel, R.A., Ferrini, V., Goodwillie, A., Nitsche, F., et al., 2009. Global multi-resolution topography synthesis. *Geochemistry, Geophysics, Geosystems* 10.
- Sagiya, T., 2004. Interplate coupling in the Kanto district, central Japan, and the Boso Peninsula silent earthquake in May 1996, in: *Computational Earthquake Science Part II*. Springer, pp. 2327–2342. <https://doi.org/10.1007/s00024-004-2566-6>.
- Saksono, T., Fulazzaky, M.A., Sari, Z., 2018. Geodetic analysis of disputed accurate qibla direction. *Journal of Applied Geodesy* 12, 129–138. <http://doi.org/10.1515/jag-2017-0036>.
- Savenije, H.H., 2005. *Salinity and tides in alluvial estuaries*. Gulf Professional Publishing.
- Scholz, C.H., 2019. *The mechanics of earthquakes and faulting*. Cambridge university press.
- Schwartz, S.Y., Rokosky, J.M., 2007. Slow slip events and seismic tremor at circum-Pacific subduction zones. *Reviews of Geophysics* 45. <https://doi.org/10.1029/2006RG000208>.

- Servicio Mareográfico Nacional (SMN), Universidad Nacional Autónoma de México, Instituto de Geofísica, México, 2024. <http://www.mareografico.unam.mx>.
- Servicio Sismológico Nacional (SSN), Universidad Nacional Autónoma de México, Instituto de Geofísica, México, 2023. <http://www.ssn.unam.mx>.
- Shimazaki, K., Nakata, T., 1980. Time-predictable recurrence model for large earthquakes. *Geophysical Research Letters* 7, 279–282. <https://doi.org/10.1029/GL007i004p00279>.
- Shum, C., Ries, J., Tapley, B., 1995. The accuracy and applications of satellite altimetry. *Geophysical Journal International* 121, 321–336. <https://doi.org/10.1111/j.1365-246X.1995.tb05714.x>.
- Singh, S., Astiz, L., Havskov, J., 1981. Seismic gaps and recurrence periods of large earthquakes along the Mexican subduction zone: A reexamination. *Bulletin of the Seismological Society of America* 71, 827–843. <https://doi.org/10.1785/BSSA0710030827>.
- Suárez, G., Monfret, T., Wittlinger, G., David, C., 1990. Geometry of subduction and depth of the seismogenic zone in the Guerrero gap, Mexico. *Nature* 345, 336–338. <https://doi.org/10.1038/345336a0>.
- Sumich, J.L., Morrissey, J.F., 2004. *Introduction to the biology of marine life*. Jones & Bartlett Learning.
- Suárez, G., 2024. Personal communication. Instituto de Geofísica, Universidad Nacional Autónoma de México.
- Thomson, R.E., Emery, W.J., 2014. *Data analysis methods in physical oceanography*. Newnes.
- Totten, S.M., 1981. Frank B. Taylor, plate tectonics, and continental drift. *Journal of Geological Education* 29, 212–220.
- Tsuji, S., Araki, E., Yokobiki, T., Nishida, S., Machida, Y., Zumberge, M., Takahashi, K., 2023. Precise tilt measurement by seafloor borehole tiltmeters at the Nankai Trough subduction zone. *Earth, Planets and Space* 75, 188.
- United States Geological Survey (USGS), 1999. Which volcanic eruptions were the deadliest? <http://www.usgs.gov>.
- Utsu, T., 1966. Regional Differences in Absorption of Seismic Waves in the Upper Mantle as Inferred from Abnormal Distributions of Seismic Intensities. *Journal of the Faculty of Science, Hokkaido University. Series 7, Geophysics* 2, 359–374.
- Vaniček, P., 1978. To the problem of noise reduction in sea-level records used in vertical crustal movement detection. *Physics of the Earth and Planetary Interiors* 17, 265–280. [https://doi.org/10.1016/0031-9201\(78\)90041-9](https://doi.org/10.1016/0031-9201(78)90041-9).
- Von Storch, H., Woth, K., 2008. Storm surges: perspectives and options. *Sustainability Science* 3, 33–43. <https://doi.org/10.1007/s11625-008-0044-2>.
- Walker, G.T., 1924. Correlations in seasonal variations of weather. I. A further study of world weather. *Mem. Indian Meteorol. Dep.* 24, 275–332.
- Wallace, L.M., Webb, S.C., Ito, Y., Mochizuki, K., Hino, R., Henrys, S., Schwartz, S.Y., Sheehan, A.F., 2016. Slow slip near the trench at the Hikurangi subduction zone, New Zealand. *Science* 352, 701–704. <https://doi.org/10.1126/science.aaf2349>.
- Wang, B., 2002. Kelvin waves. *Encyclopedia of atmospheric sciences* 1062.
- Wang, C., Deser, C., Yu, J.Y., DiNezio, P., Clement, A., 2017. El Niño and Southern Oscillation (ENSO): a review. *Coral reefs of the eastern tropical Pacific*, 85–106 https://doi.org/10.1007/978-94-017-7499-4_4.
- Watts, D.R., Kontoyiannis, H., 1990. Deep-ocean bottom pressure measurement: Drift removal and performance .

- Watts, D.R., Wei, M., Tracey, K.L., Donohue, K.A., He, B., 2021. Seafloor geodetic pressure measurements to detect shallow slow slip events: Methods to remove contributions from ocean water. *Journal of Geophysical Research: Solid Earth* 126, e2020JB020065.
- Webb, S.C., Zhang, X., Crawford, W., 1991. Infragravity waves in the deep ocean. *Journal of Geophysical Research: Oceans* 96, 2723–2736.
- Wegener, A., 1915. *Die Entstehung der Kontinente und Ozeane* [El origen de los continentes y océanos]. Braunschweig: Friedrich Vieweg & Sohn Akt. Ges.
- Welch, P., 1967. The use of fast Fourier transform for the estimation of power spectra: a method based on time averaging over short, modified periodograms. *IEEE Transactions on audio and electroacoustics* 15, 70–73.
- Wilson, J.T., 1963. A possible origin of the Hawaiian Islands. *Canadian Journal of Physics* 41, 863–870. <https://doi.org/10.1139/cjes-2014-0036>.
- Woodworth, P., Wöppelmann, G., Marcos, M., Gravelle, M., Bingley, R., 2017. Why we must tie satellite positioning to tide gauge data. *Eos* 98, 13–15.
- Woodworth, P., et al., 2016. *Manual on Sea-level Measurements and Interpretation, Volume V: Radar Gauges*. Paris, Intergovernmental Oceanographic Commission of UNESCO. JCOMM Technical Report No. 89. <https://doi.org/10.25607/OBP-1444>.
- Working Group on California Earthquake Probabilities (WGCEP), 1995. Seismic hazards in southern California: probable earthquakes, 1994 to 2024. *Bulletin of the Seismological Society of America* 85, 379–439. <https://doi.org/10.1785/BSSA0850020379>.
- Wyss, M., Habermann, R.E., 1988. Precursory seismic quiescence. *Pure and Applied Geophysics* 126, 319–332. <https://doi.org/10.1007/BF00879001>.
- Yamaguti, S., 1965. On the Changes in the Height of Mean Sea-Level before and after the Great Niigata Earthquake on June, 16, 1964. *Journal of the Geodetic Society of Japan* 10, 187–191. <http://doi.org/10.11366/sokuchi1954.10.187>.
- Zavala-Hidalgo, J., Trujillo-Rojas, K., Gómez-Ramos, O., Zarza-Alvarado, M., Hernández-Maguey, F., Gutiérrez-Quijada, V., 2020. Tsunamis in the Mexican coasts during the period 2009-2018 and their behavior. *Coastal Engineering Journal* 62, 429–444.
- Zaytsev, O., Rabinovich, A.B., Thomson, R.E., 2017. The 2011 Tohoku tsunami on the coast of Mexico: A case study. *Pure and Applied Geophysics* 174, 2961–2986.
- Zobin, V.M., Jiménez, Z., 2008. Some regularity in the process of re-awakening of andesite and dacite volcanoes: specific features of the 1982 El Chichón volcano, México reactivation. *Journal of volcanology and geothermal research* 175, 482–487.

GLOSSARY

- Aftershocks:** A sequence of earthquakes that occur after a mainshock; thus, their magnitudes are usually smaller. They originate from the relaxation of blocks during an earthquake.
- Astronomic tide:** The periodic perturbation (fall and rise) of the water level caused by the gravitational forces of the Moon and Sun on Earth.
- Average recurrence time (or return time):** The concept of recurrence time is used to calculate the seismic hazard to estimate the average time between large earthquakes that break the same fault, generally $M_W > 7.0$.
- Continental crust:** Comprises 0.40 % of the Earth's mass and 41 % of its surface. It is composed of granitic material, and its density is approximately 2.8 gm/cm^3 .
- Coseismic displacement:** Coseismic displacement refers to the sudden movement of the Earth's crust caused by the release of stress during an earthquake. This displacement reflects the offset along the fault and can be measured on the surface.
- Fault gouge:** results from fine-grained grinding of the sliding between two fault planes.
- Foreshocks:** A sequence of smaller earthquakes that occur in the same region following a main earthquake, resulting from the readjustment of the crust due to the stress changes caused by the main shock.
- Geoid:** Surface on which the gravitational field of the Earth is uniform.
- Geologic faults:** are crustal fractures that exhibit convergent (inverse fault), divergent (normal fault), and transcurrent (transform fault) displacements.
- Glacial striations:** long, linear scratches on the surface of rocks created by the movement of glaciers as they drag debris across the rock.
- High (low) pressure system:** This is the zone of circulating air in which the atmospheric pressure is high (low) compared to its surroundings.
- Hot spots:** are formed by magmatic material at temperatures higher than their surroundings. They come from the core-mantle boundary in the form of mantle plumes. Magma is concentrated under the plate (oceanic or continental) and later erupts as volcanoes. The hot spots were the idea of geologist Wilson to explain the origins of the Hawaiian Islands because they are far from subduction zones that could lead to volcanic activity.
- Hypocenter:** is defined as the location of the earthquake source below the terrestrial surface; its projection on the surface is the **epicenter**. The hypocenter of an earthquake is presented as a point source for calculation because in reality, when a seismic event occurs, a fault portion (area) is broken.
- Magnetic reversal:** is the change of magnetic polarity. Thus, the magnetic North Pole will become the magnetic South Pole, and this will become the magnetic North Pole.
- Mean dynamic topography:** is defined as the height of the averaged ocean surface relative to the geoid. The gradient of the mean dynamic topography is used in the calculation of global oceanic currents.
- Mean sea surface:** is obtained using altimetric data for a period sufficient to filter annual, semiannual, and seasonal variations. The value is relative to the reference ellipsoid.
- Mid oceanic ridges:** Chain of seamounts where oceanic spreading occurs via fissure volcanism.
- Ocean internal waves:** are oscillations within a stratified fluid that occur at density interfaces. They transfer energy and influence oceanic mixing processes.
- Ocean-bottom pressure:** is the pressure exerted by a seawater column at a point on the seafloor.

Oceanic crust: is composed of iron and magnesium minerals; hence, it has a density greater than about 3 gm/cm^3 . Oceanic crust is created at mid-oceanic ridges and is recycled in subduction zones.

Orogeny: is the formation of mountain ranges by folding, faulting, and thrusting of the Earth's crust.

Pacific Ring of Fire: A geologic region delimited by the edges of the Pacific plate characterized by high seismic and volcanic activity. On the east side, the Nazca plate subducts under the South American plate, and the CoCos plate subducts under the North American plate; in the west, the Pacific plate subducts under the Australian plate, and in the north the North American plate.

Pangea: was a supercontinent that began to fragment 200 million years ago due to continental drift mechanism.

Reference ellipsoid: is defined as that surface formed by an ellipsoid of revolution, with which the shape of the Earth can be approximated and whose center coincides with the Earth's center of mass.

Satellite altimetry: A technique that uses radar pulses emitted by artificial satellites to measure the height of a reflective surface (oceanic or terrestrial) concerning a reference ellipsoid.

Seafloor spreading theory: This hypothesis explains that hot magma from the mantle rises (by convection) at mid-ocean ridges, creating new oceanic crust. This new crust will be denser as it cools and, in turn, will move away from the ridge and sink into a trench, thereby completing the convection cycle.

Seismic asperity: is a localized area along a fault where the frictional resistance is higher, allowing it to accumulate elastic strain. These zones often play a critical role in earthquake initiation and magnitude.

Seismic cycle: is a geologic model in which earthquakes are expected to occur approximately every determined time but are not periodic. It helps predict the seismic risks of a region. It considers interseismic (ac-

cumulation of stress), preseismic, coseismic (sudden release of energy in the form of seismic waves), and postseismic phases.

Seismic gap: A segment of a fault where there is an absence of significant earthquakes for a period that exceeds the average recurrence interval of large earthquakes in surrounding areas.

Seismic magnitude: is the size of an earthquake. The magnitude of surface waves is calculated by measuring the amplitude of seismic waves; the magnitude of energy uses the energy irradiated by an earthquake; the coda wave magnitude uses the duration of the coda wave in a record; and moment magnitude that makes use of the seismic moment.

Seismic moment: This quantifies the size of an earthquake by considering the rupture area, fault slip, and shear modulus of the rocks affected by the earthquake.

Seismic quality factor: This factor quantifies the decay of subsurface seismic waves. Therefore, it measures the physical state (consolidated or unconsolidated) of the medium through which the seismic waves travel.

Seismic waves: Mechanical waves that come from an earthquake. There are two types: (1) *P* and *S* waves, which are called body waves because they travel through the interior of the Earth, and (2) surface waves of Rayleigh and Love.

Seismogenic zone: This zone has the largest proportion of subduction earthquakes. The oceanic crust is fragile, and as it sinks, it becomes more plastic. Hence, earthquakes occur mainly at shallow depths, and those with deep hypocenters are very rare.

Seismograph: This instrument records seismic waves traveling through a rocky medium. The product is called a seismogram. It was invented in 1855 by physicist Luigi Palmieri.

Seismotectonics: This term refers to the causes of seismic events closely related to geological activity (e.g., geologic faults).

Static friction: is the friction force that opposes

- the start of the displacement of an object; the **dynamic friction** is the friction force when the object is already in motion.
- Storm surge:** is an intense rise in sea level on the coast due to storm winds.
- Storm tide:** occurs when a storm surge coincides with a high tide, causing a drastic increase in sea level and flooding.
- Sub-lunar point:** this point is on the Earth's surface under the Moon.
- Subduction zone:** a region where a denser tectonic plate sinks by gravity under another, which is less dense.
- Theory of continental drift:** It proposes that the continents were once joined in a single landmass, known as Pangaea, and later drifted apart to reach their current positions. This theory was extensively developed by Alfred Wegener in 1915.
- Theory of elastic rebound:** This model describes the tectonic causes of earthquakes: the movement of the crust causes two blocks to accumulate elastic tension; when this limit is exceeded, the sudden movement produces seismic waves. The crust is assumed to be elastic. Harry Reid proposed this model after studying the 1906 San Francisco earthquake.
- Theory of plate tectonics:** a geological model in which the lithosphere is divided into fragments known as tectonic plates. The boundaries of these plates are convergent, divergent, and transform. These plates move relative to each other because of convection forces in the mantle. This theory combines continental drift theory with ocean spreading theory.
- Tide gauge benchmark:** is a metal plate inserted near a tide gauge station where sea level measurements are referenced to zero level.
- Trade winds:** Winds blowing from east to west along the equatorial region. They come from the northeast, in the Northern Hemisphere, and from the southeast, in the Southern Hemisphere.
- Tsunami:** is a phenomenon that consists of a wave series due to water displacement caused by a submarine earthquake, volcanic eruption, or landslide. In the open sea, the period of waves is usually several kilometers; when waves approach the coast, their period is reduced, forming waves that can exceed 30 meters.
- Volcanic explosivity index:** is a semi-quantitative logarithmic scale used to measure the intensity of a volcanic eruption. The calculation involves several factors, such as the duration of the volcanic explosion.
- Walker cell:** The atmospheric circulation in the intertropical convergence zone moves the cold air (East Pacific) to the warm zone (West Pacific); from there, it rises to descend again in the high-pressure region, cooling down.
- Atmospheric pressure:** The force per unit area exerted by a column of air in the atmosphere.
- Low-frequency earthquakes:** Earthquakes with frequencies > 1 Hz and magnitudes $M_W \ll 3$.
- Nonvolcanic tremors:** Seismic phenomena similar to volcanic tremors, characterized by low-frequency, nonimpulsive signals often associated with tectonic processes rather than volcanic activity.
- Slow slip event:** Earthquakes generated by the aseismic slip of faults without radiating seismic waves. The duration of these events is usually days, weeks, and months. Fluid migration is believed to cause slow slip events in subduction zones.
- Very low-frequency earthquakes:** Similar to low-frequency earthquakes, but their durations are 10–200 s, and their spectrum is between 0.01–0.10 Hz.

ABBREVIATIONS

ACA Acapulco	MDT Mean dynamic topography
CEOF Complex empirical orthogonal function	MSL Mean sea level
CPD Cycles per day	MAT Middle America Trench
CPH Cycles per hour	NNR No-net-rotation
CW Cosine window	NVT Nonvolcanic tremor
DART Deep-ocean Assessment and Reporting of Tsunamis	OBP Ocean-bottom pressure
DORIS Doppler Orbitography and Radiopositioning Integrated by Satellite	OBT Ocean-bottom temperature
EQ Earthquake	PR Pulse radar
EP East Pacific	PSD Power Spectral Density
ENSO El Niño-Southern Oscillation	LR Rayleigh waves
ETS Episodic tremor and slip	SEMAR Secretaría de Marina
GEBCO General Bathymetric Chart of the Oceans	SC Seismic cycle
GPS Global Positioning System	SMN Servicio Mareográfico Nacional
GSG Guerrero seismic gap	SO Southern Oscillation
HPR High-Pressure Region	SOI Southern Oscillation Index
InSAR Interferometric Synthetic Aperture Radar	SRM Spectral ratio method
IB Inverted barometer	SSE Slow slip event
LFE Low-frequency earthquake	SST Sea surface temperature
LOS Line Of Sight	TS Tsunami
LPR Low-Pressure Region	VLFE Very low-frequency earthquake
LQ Love waves	FMCWR Frequency-modulated continuous-wave radar
LOWESS Locally Weighted Scatterplot Smoothing	WP West Pacific
MZN Manzanillo	

NOMENCLATURE

ΔR_{atm} Atmospheric load correction	C_p Propagation corrections
ΔR_{dry} Dry tropospheric correction	$C_{xy}(\tau)$ time-lagged cross-correlation
ΔR_{ion} Ionospheric correction	D Average fault displacement
ΔR_{tides} Tide effect correction	d Distance
ΔR_{wet} Wet tropospheric correction	D_{cc} Vertical displacement of the continental crust
Δ Epicentral distance	D_{sf} Vertical displacement of the seafloor
η Sea level change	E_s Radiated energy by an earthquake
λ First Lamé constant	F Gravitational force
μ Second Lamé constant (shear modulus)	G Gravitational constant
ω Angular frequency	g Gravity acceleration
\vec{v}_{sub} Subduction velocity	H_{mss} Mean sea surface height
ρ Density	H_{sat} Satelllite height
ρ_{sw} Seawater density	I Instrumental drift
σ Standard deviation	IB Inverted barometer effect
\tilde{M}^t Conjugate transpose matrix (or Hermitian transpose matrix)	K Eigenvalues of a covariance matrix
\tilde{M} Conjugate matrix	M Matrix
A Maximum amplitude of a seismic wave	M_B Body wave magnitude
a Earth's radio	M_c Coda wave magnitude
A_f Area of the rupture along the geologic fault	M_e Energy magnitude
A_M Antipodal point	m_E Earth mass
AT Astronomical sea level	m_M Moon mass
B_M Sub-lunar point	M_s Surface wave magnitude
C Eigenvectors of a covariance matrix	M_W Moment magnitude
c Speed of light	M_0 Seismic moment
C_g Geophysical corrections	M_{cov} Covariance matrix
C_{pc} Pearson correlation coefficient	M_L Local magnitude
	N Geoid height

N_h	Number of harmonic terms	S_{bg}	Background spectrum
N_x	Number of measurements	S_{obs}	Observed tsunami spectrum
NT	Nontidal components	S_{ratio}	Spectral ratio
P	Primary or longitudinal seismic wave	S_{tsu}	Tsunami spectrum
P_0	Mean atmospheric pressure	SL	sea level
P_{mob}	Mean ocean-bottom pressure	SL_m	mean sea level
P_{obs}	Observed atmospheric pressure at sea level	T	Period
P_{ob}	Ocean-bottom pressure	T_d	Height of the mean dynamic topography
Q	Quality factor or anelastic attenuation of seismic waves	T_t	Filtered value
		v_p	P -wave velocity
R	Altimetric range	v_s	S -wave velocity
S	Secondary or transverse seismic wave	W	Tricube weight function
S_ϵ	Noise spectrum	z	Height of a water column